Structural mechanics and collective self-organisation in filamentous cyanobacteria

Mixon Kanyama Faluweki

A thesis submitted in partial fulfillment of the requirements of Nottingham Trent University for the degree of Doctor of Philosophy

May 8, 2023

Abstract

Filamentous cyanobacteria, one of the earliest types of organisms to have evolved on Earth, are photoautotrophs made of single cells joined together in long filaments. They are ubiquitous, living in water, soil, rocks and extreme environments like hot springs. Their oxygen production is believed to have led to the evolution of oxygen-dependent organisms like us. They live in colonies forming biomats, and are associated with stromatolites, which are important for understanding the evolution of early life. Commercially, filamentous cyanobacteria are used for biofuel production, food supplements, cosmetics and medicines. In order to maximise the usage of these microorganisms, we must understand how individual filaments interact and form collective structures. This thesis, therefore, focuses on quantifying the mechanical properties and collective organisation of filamentous cyanobacteria. First, the structural and mechanical properties of the filaments, such as the bending stiffness, are quantified. The mechanical properties are linked to their shapes, to predict the magnitude of internally generated active forces. These results can be used to model cyanobacteria motion and self-organisation. Next, this thesis looks at the behaviour of filaments in isolation and when interacting with other filaments or walls. These results provide parameters such as filament speed, angular drift and curvature that are then used by collaborators for modelling and predicting the collective behaviour of the cyanobacteria. The last part of this thesis provides experimental evidence of how self-organisation occurs for filamentous cyanobacteria in an open space and in confinement. A density-dependent phase transition was found, between disordered and nematically ordered patterns of filamentous cyanobacteria. Finally, in confinement studies, it was observed that certain chamber geometries, e.g. circular, promote unequal filament distribution. The results here are applicable in areas such as the study of stromatolites and the evolution of early life, and in the production of algae-based biofuels.

Acknowledgments

This work has been completed with support from a number of people both within and outside Nottingham Trent University and I would like to thank them all.

Special thanks to my director of studies, Dr. Lucas Goehring for his immeasurable guidance throughout this project. His dedication to duty, being always available for meetings has shaped me into a better researcher. Any of my future academic success stories would not be complete without mentioning the foundation he has helped me to build.

I would also like to thank my supervisor Professor Haida Liang and independent assessor Dr. David Fairhurst for their guidance and support throughout this project.

My research work was largely collaborative and this was possible with a team of dedicated researchers across multiple institutions. I would like to thank Jan Cammann, and Dr. Marco G. Mazza from Loughborough University, UK, for their valuable discussions and their numerical work which has tremendously helped me in this project. I also thank Dr. Stefan Karpitschka from the Max Planck Institute for Dynamics and Self-organisation for the valuable discussions on this project.

The project was funded by the Max Planck Institute for Dynamics and Self-organisation (MPIDS) and Nottingham Trent University of whom I am so thankful for the opportunity to carry out this research.

My lab colleagues, in particular Thomas Darwent, Megha Emerse, Jay Marsden and Patrick Atkinson who have supported me endlessly and became friends if not a family. I will forever be thankful to you friends.

I am also grateful to all the technicians, research fellows and staff at Nottingham Trent University for their unlimited support. Special thanks should go to Dr. Chi Cheung (Sammy) for the support with OCT, Dr. Graham J. Hickman and Kathryn Kroon for helping with TEM and light microscopy and Ryan Toms for helping with different technical works.

To all staff and students that played football with me, I thank you all for keeping entertained.

Finally, my biggest thanks goes to my wife Esther and daughter Mwatipatsa. I am so thankful for the support my wife has given me and for the happiness that my daughter brought to my life during most of the challenging times. They gave me plenty of reasons to keep going.

List of Publications

Published Paper

M. K. Faluweki and L. Goehring, Structural mechanics of filamentous cyanobacteria, Journal of The Royal Society Interface **19**, 20220268 (2022).

Paper In Preparation

M. K. Faluweki*, J. Cammann*, M. G. Mazza and L. Goehring. Active spaghetti: collective organization in cyanobacteria. arXiv:2301.11667, 2023. [*Equal contribution]

Contents

Abstract i

Acknowledgments ii

List of Publications iii

Contents iv

List of Figures viii

1 Introduction 1

1.1 Motility in filamentous cyanobacteria 4

1.2 Collective behaviour in filamentous cyanobacteria 4

1.3 Importance of filamentous cyanobacteria 5

1.4 Thesis organisation 7

1.5 Research aims and objectives 8

2 Methodology 10

2.1 Microfabrication 10

2.1.1 Photolithography 10

2.1.2 Soft lithography 13

2.1.3 Wafer film thickness measurement using OCT 15

2.2 Confocal microscopy 18

2.2.1 Confocal image acquisition 19

2.2.2 Confocal image post-acquisition processing 21

2.3 Culture and sample preparation 21

2.3.1 Culture maintainance 22

2.3.2 Culture transfer and sample preparation for experiments 22

2.3.3 Disposal of culture 23

3 Structural mechanics of filamentous cyanobacteria 24

3.1 Introduction 24

3.1.1 Filament bending and flow in a microfluidic channel 26

3.1.2 Atomic force microscopy for stiffness measurement 28

3.2 Methods . . . 30
3.2.1 Culture and sample preparation . . . 30
3.2.2 Bending stiffness measurement using a microfluidic flow device . . . 31
3.2.3 Nanoindentation . . . 37
3.2.4 Cell wall imaging . . . 39
3.2.5 Filament shape imaging . . . 40
3.3 Results . . . 41
3.3.1 Bending stiffness . . . 42
3.3.2 Nanoindentation and cell wall properties . . . 48
3.3.3 Filament curvature and shape . . . 52
3.4 Discussion . . . 54
3.5 Conclusions . . . 57

4 Dynamic properties of single cyanobacteria filaments 59
4.1 Introduction . . . 59
4.2 Methodology . . . 61
4.3 Results . . . 64
4.3.1 Isolated filaments move in circular clockwise motion . . . 64
4.3.2 Gliding speed is roughly constant . . . 65
4.3.3 Angular drift is roughly constant . . . 69
4.3.4 Filament rotation and tip motion . . . 71
4.3.5 Curvature fluctuations have a correlation time . . . 73
4.3.6 Filaments reverse their motion randomly but maintain clockwise motion . 75
4.4 Discussion . . . 77
4.5 Conclusion . . . 78

5 Cyanobacteria filament interaction with walls and other filaments 80
5.1 Introduction . . . 80
5.2 Methodology . . . 82
5.2.1 Cyanobacteria filaments pair-wise interaction . . . 82
5.2.2 Cyanobacteria filament and wall interactions . . . 83
5.2.3 Variation of filament curvature with filament density . . . 83
5.2.4 Motion of filaments in bundles . . . 84
5.3 Results . . . 86
5.3.1 Cyanobacteria filaments pair-wise interaction . . . 86
5.3.2 Cyanobacteria filament and wall interactions . . . 88

5.3.3 Effect of interactions on filament curvature . . . 89
5.3.4 Filaments in a bundle move equally in both directions . . . 91
5.4 Conclusion . . . 92

6 Cyanobacteria self-organisation in an open space 94
6.1 Introduction . . . 94
6.1.1 Model of self-organisation of filamentous cyanobacteria . . . 95
6.1.2 Prediction of the phase transition point . . . 95
6.2 Methodology . . . 97
6.2.1 Sample preparation . . . 97
6.2.2 Sample imaging . . . 98
6.2.3 Measuring filament density . . . 99
6.3 Results . . . 102
6.3.1 Emergence of nematic order . . . 102
6.3.2 Structure size in filamentous cyanobacteria patterns . . . 105
6.3.3 Ordering behaviour in naturally multiplying colonies . . . 107
6.3.4 Topological defects in *O. lutea* colonies . . . 107
6.4 Conclusion . . . 111

7 Cyanobacteria self-organisation in confinement 113
7.1 Introduction . . . 113
7.2 Methodology . . . 114
7.3 Results . . . 117
7.3.1 Filaments accumulate at the walls in circular confinement . . . 117
7.3.2 Filament structure in other confinement geometries . . . 119
7.4 Conclusion . . . 120

8 Summary and Outlook 122
8.1 Summary . . . 122
8.1.1 Structural and mechanical properties of filamentous cyanobacteria . . . 122
8.1.2 Isolated cyanobacteria filaments motion . . . 123
8.1.3 Collective interaction between filaments. . . . 124
8.1.4 Collective organisation in filamentous cyanobacteria . . . 125
8.1.5 Cyanobacteria in confinement. . . . 125
8.2 Future outlook . . . 126

Bibliography **128**

List of Figures

1.1 Examples of stromatolites at Hamelin Pool. 1
1.2 Diversity of cyanobacteria. 2
1.3 Comparing the internal structure of cyanobacteria with other bacteria. 3
1.4 Electron micrograph of a fragmented single cell of *Oscillatoria sp.* filament. . . . 4
1.5 Reticulate patterns formed due collective behaviour of filamentous cyanobacteria. 5
1.6 A biofilm of *Klebsormidium flaccidum* growing on a terracotta statue, Cathedral of Seville. 6

2.1 Photolithography steps and fabricated mould. 13
2.2 Soft lithography process. 14
2.3 Schematic diagrams of time-domain and Fourier-domain optical coherence tomography. 17
2.4 Illustration of pillar height measurement using OCT. 18
2.5 A schematic diagram of a confocal microscope. 19
2.6 Illustration of confocal wide-area scanning. 20
2.7 Example filamentous cyanobacteria raw images and initial processing workflow. . 21
2.8 An incubator used to keep samples in this project 23

3.1 An example of filamentous cyanobacteria collective structure 25
3.2 Modelling cyanobacteria bending and structure. 27
3.3 Schematic representation of tapping mode AFM. 28
3.4 Example AFM force-distance curve. 29
3.5 A snapshot of CAD design for a flow channel used in this project. 32
3.6 Convergence of the flow field numerical approximation. 33
3.7 Flow field along the mid-plane of a rectangular microfluidic channel. 35
3.8 Microfluidic flow cell. 36
3.9 Flow test sequence. 37
3.10 Stiffness analysis using Bruker's Nanoscope analysis software. 38
3.11 Internal structure of cyanobacteria. 39
3.12 Filamentous cyanobacteria under confocal fluorescence imaging. 40
3.13 Filament widths and structure in *O. lutea* 41
3.14 Measurements of the bending stiffness of filamentous cyanobacteria. 45

3.15 Example microfluidic pillars for three-point bending test. 48
3.16 Comparison of partial-slip and no-slip flow-induced bending stiffness calculations. 48
3.17 Cross-sectional images of filamentous cyanobacteria. 49
3.18 Cyanobacteria elasticity as measured by nanoindentation 51
3.19 Curvature analysis in filamentous cyanobacteria. 52
3.20 Curvature distributions in three species of filamentous cyanobacteria. 53
3.21 Measured persistence length in inactive cyanobacteria filaments 56

4.1 Electron micrograph of a fragmented single cell of *Oscillatoria sp.* filament. . . . 60
4.2 Example images of single filaments of cyanobacteria (*O. lutea*). 61
4.3 Example image stitching process. 63
4.4 Image processing for single filaments. 64
4.5 Cyanobacteria filament midpoint track. 65
4.6 Cyanobacteria filament speed. 66
4.7 Filament speed vs. filament length. 66
4.8 Effect of sliding window size on the computed speed. 67
4.9 Filamentous cyanobacteria rotate as they glide. 68
4.10 Comparing cyanobacteria filament speed measurement approaches. 69
4.11 Analysis of filament speed periodic behaviour in *O. lutea*. 70
4.12 Angular drift in *O. lutea*. 71
4.13 Cyanobacteria filament rotation analysis. 72
4.14 Filamentous cyanobacteria dynamic curvature. 74
4.15 Reversal time distribution in *O. lutea*. 76

5.1 Example collective structure in *O. lutea* 80
5.2 Quantification of filament interaction behaviour. 82
5.3 Quantification of filament-wall interactions. 84
5.4 Quantification of filament curvature with filament density. 85
5.5 Measurement of the direction of motion of filaments in bundles. 86
5.6 Cyanobacteria filament to filament alignment. 87
5.7 Filament-wall alignment results. 89
5.8 Curvature distribution in colonies of different densities. 90
5.9 Effect of interactions on filament curvature. 91
5.10 Direction of motion of filament in bundles. 92

6.1 Schematic depiction of the filament-filament interaction in simulations. 96

6.2 An illustration of random filament interactions. 97
6.3 The experimental setup for structure formation. 98
6.4 Example full well image (left) of filamentous cyanobacteria collective structure. . 99
6.5 Demonstration of adaptive image threshold. 101
6.6 Verification of filament density measurement. 102
6.7 Generation of an angle map from a filament structure image. 103
6.8 Calculation of S_{2D} from a skeletonised image. 105
6.9 Ordering transition in filamentous cyanobacteria. 106
6.10 Size of structures in dense systems. 108
6.11 Comparing the ordering transition between long and short-term cyanobacteria colonies. 109
6.12 Classification of topological defect charge. 109
6.13 Examples of defects in 2D nematic liquid crystal. 110
6.14 Defect dynamics in filamentous cyanobacteria structure. 111

7.1 A snapshot of confinement design in QCAD software. 115
7.2 Filamentous cyanobacteria in confinement chambers. 116
7.3 Wall hugging effect of *O. lutea* in confinement. 118
7.4 Depletion and ordering of filaments at the centre of a circular confinement. . . . 119
7.5 Comparing filament structure formation in four different confinement geometries. 120

Chapter 1

Introduction

Cyanobacteria, also known as blue-green algae, are one of the most successful forms of life on Earth, with origins dating back over two billion years [1–3]. They are autotrophs that make food from sunlight, water, and carbon dioxide through photosynthesis [4]. It is believed that the ability of cyanobacteria to photosynthesise and release oxygen caused significant changes to the Earth's atmosphere during the Precambrian i.e. "the great oxidation event" [5], allowing for the eventual evolution of other life forms that rely on that oxygen, including us [3].

Cyanobacteria are also ubiquitous, finding habitats in most water bodies and in extreme environments such as the polar regions, deserts, brine lakes, and hot springs [6–8]. In water bodies, cyanobacteria contribute to the formation of stromatolites, which are layered formations that are formed by adhesive compounds produced by cyanobacteria and other microorganisms over a long period of time [9]. The oldest known stromatolites are from the Huntsman Limestone (Bulawayan Group) in Zimbabwe [10], which are about 3 billion years old. The first known modern stromatolites were discovered in Hamelin Pool, Australia in the 1950's [11, 12] and examples are shown in Figure 1.1. Since their discovery, modern stromatolites have had a significant impact on the study of the early evolution of life, allowing for comparing them with fossil records [13].

Figure 1.1: Examples of stromatolites at Hamelin Pool. These lumps are formed gradually by the piling microbial mats. The mats are formed when adhesive compounds from microorganisms such as cyanobacteria cement sand and other materials. Permission to reproduce this figure has been granted by Bush Heritage Australia [14]

Cyanobacteria are a diverse group with some species found as unicellular, like *Chroococcus*, while others form long chains of joined cells that can be either branched or unbranched. Some examples of cyanobacteria are shown in Figure 1.2. The diversity is not only in the arrangement of cells but within the cells as well as in their morphology and metabolic function. For example, the genus of *Gloeobacter* is different from all other cyanobacteria groups in that it lacks thylakoids which are the characteristic light-harvesting features of all other cyanobacteria [15]. Photosynthesis in *Gloeobacter* takes place in the plasma membrane rather than in thylakoid as in all other cyanobacteria groups [16, 17]. Some groups like *Chroococcidiopsis* survive harsh conditions like high salinity [18] and extreme UV radiation [19]. The filamentous ones are also differentiated in their structure with some coiled, like *Spirulina subsalsa*, while others like *Oscillatoria lutea* appear more straight, as shown in Figure 1.2. Certain filamentous cyanobacteria like *Nostoc* (Figure 1.2(d)) also have specialised cells called heterocysts that help fix nitrogen from the air [20].

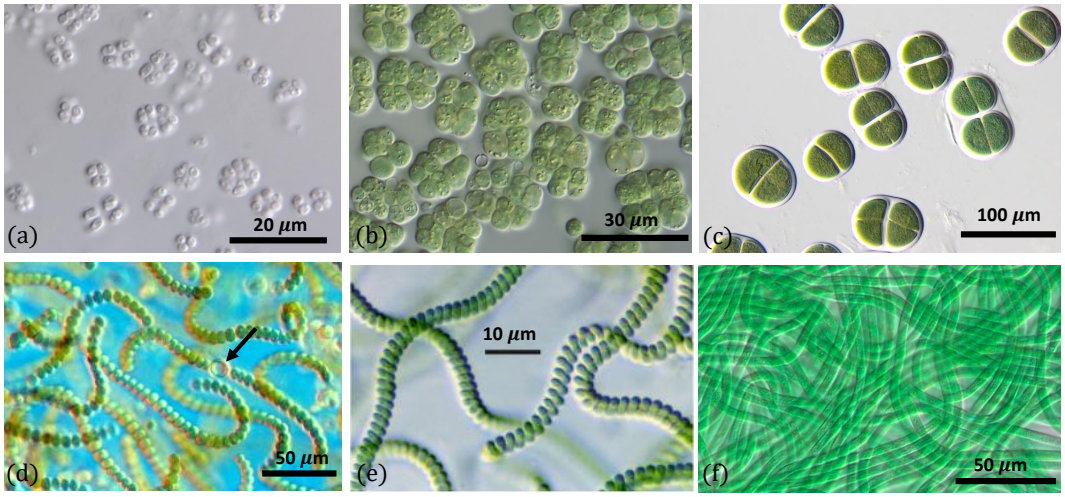

Figure 1.2: Diversity of cyanobacteria. From unicellular forms like *Gloeobacter violaceus* (a), *Chroococcidiopsis cubana* (b), and *Chroococcus turgidus* (c), to filamentous species like *Nostoc microscopicum* (d), *Spirulina subsalsa* from order *Spirulinales* (e) and *Oscillatoria lutea* (f). Certain species like *Nostoc microscopicum* (d) have specialised cells called heterocysts (shown by the arrow) that help fix nitrogen from the air. Images (a)-(d), and (f) were taken from SAG culture collection catalogue (SAG 7.82, SAG 39.79, SAG 36.85, SAG 55.79, SAG 1459-3) [21]. Image (e) was adapted from Sili *et al.* 2013, [22]. Permission to reproduce these images has been granted by the respective authors.

In terms of their internal structure, cyanobacteria are classified as Gram-negative bacteria which are a group of bacteria that do not retain the crystal violet stain used to differentiate

bacteria (Gram staining) [23]. This differentiation divides bacteria into two major groups: Gram-positive and Gram-negative. Generally, Gram-negative bacteria have a thin cell wall, with the exemption being cyanobacteria whose peptidoglycan layer thickness is similar to that of Gram-positive bacteria. Further details of the cell wall are illustrated in Figure 1.3. Later in this thesis, I will refer to this internal structure with the aim of estimating the internal forces generated by the activity of filamentous cyanobacteria.

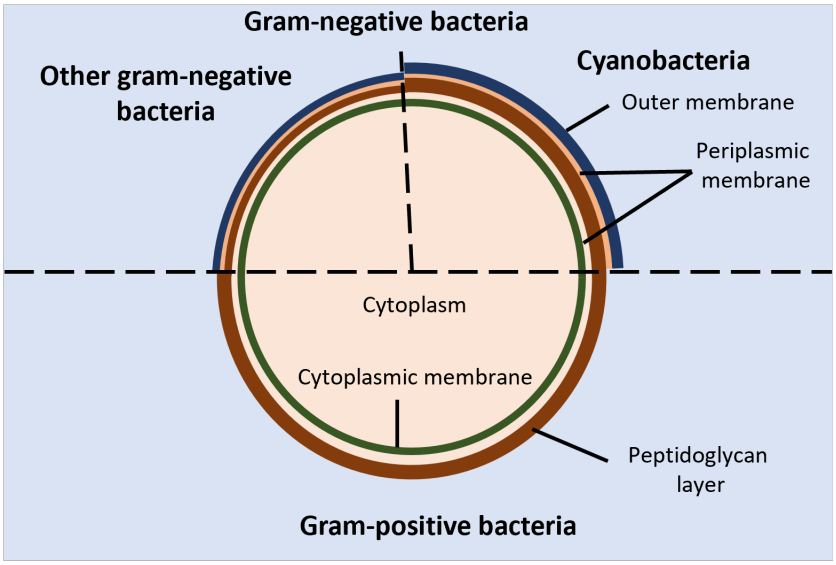

Figure 1.3: Comparing the internal structure of cyanobacteria with other bacteria. Generally, Gram-negative bacteria have a thin peptidoglycan layer, except cyanobacteria whose peptidoglycan layer thickness is similar to that of Gram-positive bacteria. Figure adapted with modifications from [24]. Permission to reproduce this figure has been granted by the publisher.

Being a diverse group, cyanobacteria are classified into different orders. The traditional classification of cyanobacteria was based on morphology but the modern classification is based on genetic analysis. As of 2014, there were nine orders of cyanobacteria [25]. However, in an updated classification from the online database of cyanobacteria [26] at the time of writing, the number of groups had grown to ten. The orders of cyanobacteria that are most relevant to this thesis are the filamentous ones, *Nostocales* and *Oscillatoriales*, that bundle together into larger structures including biofilms, biomats and stromatolites [27,28]; this project focuses on the order *Oscillatoriales*.

1.1 Motility in filamentous cyanobacteria

All known cyanobacteria lack flagella [29], however many filamentous species move on surfaces by gliding, a form of locomotion where no physical appendages are seen to aid movement [30]. The actual mechanism behind gliding is not fully understood, although over a century has elapsed since its discovery [31,32]. One theory suggests that gliding motion in cyanobacteria is mediated by the continuous secretion of polysaccharides through pores on individual cells [33–35]. Another theory suggests that gliding motion involves the use of type IV pili, polymeric assemblies of the protein pilin [36], as the driving engines of motion [37–39]. However, it is not clear how the action of these pili would lead to motion, with some suggesting they retract [40], while others suggest they push [39], to generate forces. Other scholars have suggested surface waves generated by the contraction of a fibril layer (shown in Figure 1.4) as the mechanism behind gliding motion in *Oscillatoria* [41, 42]. As shall be discussed in Chapter 3, the magnitude of such compression forces can be estimated from measured mechanical properties and filament shapes. Recent work also suggests that shape fluctuations and capillary forces could be involved in gliding motion [43]. However, there is still a lack of quantitative study of the motion of filaments, a gap that this thesis aims to rectify.

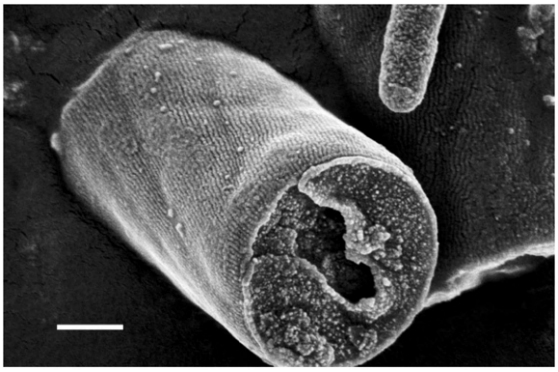

Figure 1.4: Electron micrograph of a fragmented single cell of *Oscillatoria sp.* filament showing fibril layer seen as parallel corrugations on the cell surface, running at an angle to the long filament axis. Figure adapted from [44]. Scale bar: 500 nm. Permission to reproduce this figure has been granted by the authors.

1.2 Collective behaviour in filamentous cyanobacteria

Through collective interaction, filamentous cyanobacteria self-organise into colonies or biofilms, symbiotic communities found in a wide variety of ecological niches. Their larger-scale collective

structures are characterised by diverse shapes including bundles, vortices, and reticulate patterns [45]. Similar patterns have been observed in fossil records [2, 46] and in this project, as shown in Figure 1.5. It is known that the mechanics of the filaments contribute to self-organisation, for example in determining how one filament will bend when in contact with other filaments or obstacles [47]. However, there has been a lack of any corresponding systematic measurement of the micro-mechanical properties of filamentous cyanobacteria, to the point where such properties are typically just assumed when needed in models (*e.g.* see [47]). Also, although the reticulate patterns formed by filamentous cyanobacteria have been used to match the patterns found in fossil records with modern patterns, their experimental study has been less quantitative [45]. In chapters 3,4, and 5, I seek to fill that gap by providing carefully measured values of the mechanical properties and behaviour of individual filaments of cyanobacteria, in order to help quantify their collective behaviour and understand the structures formed.

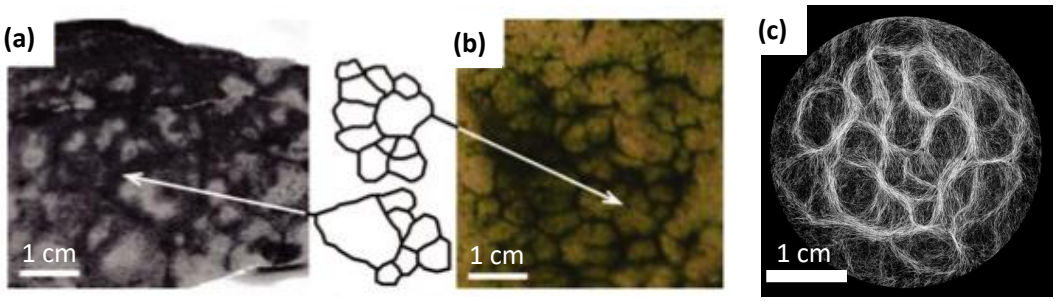

Figure 1.5: Reticulate patterns and vortices formed due to collective behaviour of filamentous cyanobacteria are similar to those found in fossil records. The patterns shown here are (a) as observed in a fossil record [46], (b) as observed in *Pseudanabaena* experiments by Shepard *et al.* [45], and (c) as observed in a culture of *Oscillatoria lutea* in this project. Permission to reproduce figures (a-b) has been granted by the authors.

1.3 Importance of filamentous cyanobacteria

Filamentous cyanobacteria are important in many ways to their environment. For example, those living in water bodies provide food and oxygen to aquatic life like fish. Certain species of filamentous cyanobacteria, such as *Anabaena* and *Nostoc*, have differentiated cells called heterocysts that help fix nitrogen from the air, and can thereby support plant growth [20, 48–50]. However, the growth of cyanobacteria in different habitats is not entirely beneficial, as cyanobacteria are known to negatively affect their environment in cases of algal blooms [51] or biofouling [52]. For example, the overgrowth of toxic algal blooms in water bodies brings different negative effects to

aquatic life including shading other aquatic plants, and possible death of fish and invertebrates due to entanglement or poisoning [51]. Furthermore, terrestrial species can invade architectural heritage and buildings where they can cause degradation of the structure [53, 54]. Indeed, cyanobacteria are one of the microorganisms contributing to the biofouling of rock art sculptures, some of which are of archaeological importance like the statue at the Cathedral of Seville shown in Figure 1.6.

Figure 1.6: A biofilm of filamentous cyanobacteria *Klebsormidium flaccidum* growing on a terracotta statue, Cathedral of Seville. Some archaeological sculptures like these are damaged by biofilm invasion. Figure adapted from [55].

Commercially, filamentous cyanobacteria have numerous applications. For example, certain species of filamentous cyanobacteria like *Spirulina* are used as food supplements due to their high nutrient content [56]. Some filamentous cyanobacteria are also considered to have medicinal powers with the potential to cure viral diseases [57]. They are also good candidates for use in bioreactors to produce a wide range of chemicals, including biofuels like biodiesel [58] and ethanol [59]. However, despite their importance to the history of life on Earth, and their commercial and environmental potentials, there remain basic questions of how filamentous cyanobacteria move, respond to their environment, and self-organise into collective patterns and structures. In chapters 5, 6, and 7 I address some of these concerns by first measuring and quantifying the key properties that underlie the behaviour of filamentous cyanobacteria and then combining these observations to study the collective structure formation of filamentous cyanobacteria in different scenarios.

In addition to this brief introductory chapter, more detailed and specific literature reviews will be given at the beginning of subsequent chapters. Here, I will instead now briefly highlight the questions addressed in the following chapters and explain what each of those chapters contributes to the whole thesis.

1.4 Thesis organisation

This thesis has eight chapters, including this introductory chapter and a final summary chapter. The work presented in the remaining chapters is introduced as follows:

Chapter 2: General materials and methods

This chapter introduces the key methods and techniques used throughout the project. These methods are referenced throughout the thesis. The three main methods or techniques covered in depth include the fabrication of microfluidic devices, confocal microscopy for imaging, and culture and sample preparation. Other techniques used, such as optical coherence tomography (OCT) and image processing, are also briefly introduced.

Chapter 3: Mechanical properties

The measurement of the key mechanical properties of filamentous cyanobacteria is covered in this chapter, which focuses on the three related species of *Kamptonema animale*, *Lyngbya lagerheimii* and *Oscillatoria lutea*. The goal is to quantify the key mechanical properties of these species and connect these to other observable filament properties, in order to estimate the range of active forces generated internally by the filaments. Specifically, I study their bending stiffness using a microfluidic flow device and link this to Young's modulus, internal cell structure, and filament shapes to estimate the internally generated forces.

Chapter 4: Dynamic properties of isolated filaments

The measurement of the key parameters governing filament motion continues here, but now the focus narrows to one species i.e. *O. lutea*, for a deeper analysis. Here the goal is to obtain the key dynamic properties of isolated filaments, in order to understand how filaments behave without interference from external factors such as other filaments or boundaries. Examples of properties studied here are the speed, angular drift and filament curvature, and how these properties change with time. These measurements are made by tracking isolated filaments gliding on a substrate.

Chapter 5: Collective filament behaviour

Continuing with the measurement of key parameters, this chapter reports on the behaviour of filaments when they interact with other filaments and with walls. This chapter builds on the isolated behaviour reported in the previous chapter and is intended to allow for the understanding of the filament's collective behaviour by breaking it down into a few key fundamental interactions.

The work in this chapter starts with quantifying what happens when two filaments meet: they either pass directly by each other or turn to align. The probability of alignment is very low, about 0.04, although this probability varies with the angle of intersection. This chapter also shows that filaments lose their preferred curvature when they interact. Another key result is that filaments align with flat walls for some considerable distance before detaching themselves.

Chapter 6: Self-organisation in an open space

In this chapter, the topic of study now turns to collective responses and the study of filamentous cyanobacteria self-organisation in an open space. Here, experimental observations are made on filamentous cyanobacteria growing in well plates and analysis is made on the observed filament structure, to determine for example the critical density at which the filaments make a transition from disorder to order. The measured critical density is linked to a predicted value, based on the parameters measured in chapters 4 and 5. The results are also compared with those from a numerical model developed by my collaborators and shown to match well. Finally, the chapter quantifies different parameters of the structures formed, such as the vortex diameters.

Chapter 7: Collective structure in confinement

This final results chapter presents the study of filamentous cyanobacteria self-organisation in confined geometries. The goal is to understand how confinement affects the distribution of filaments in chambers and also to compare the effect of different confinement shapes or geometries on filament distribution. Using microfluidic techniques, four different confinement geometries are designed and fabricated. Cyanobacteria filaments are grown inside these microfluidic devices and observations are made on the distribution of filaments within the chambers and how that changes with the size and the shape of the confinement. This chapter presents a strand of investigation that remains in progress and is intended to be the basis of follow-up collaborative research.

Chapter 8: Summary and conclusions

This final chapter summarises the work carried out in the whole thesis. Suggested future research questions originating from this thesis are also discussed.

1.5 Research aims and objectives

Here, I present the main aims and objectives of this thesis:

- Quantify the key mechanical properties of filamentous cyanobacteria using a microfluidic device and connect the measurements to the internally generated forces responsible for filament shape.
- Quantify the key dynamical properties of isolated filaments gliding on a substrate, such as filament speed and angular drift, to understand how filaments behave without any external interference.
- Build on the previous objectives and quantify the key collective behaviours of filaments gliding on a substrate.
- Study collective organisation of filamentous cyanobacteria in an open space to quantify their key structural properties.
- Study the collective organisation of filamentous cyanobacteria in confinement and quantify the effect of various parameters of the confinement geometry on filament distribution.

Chapter 2

Methodology

In this thesis, there were a number of methods or techniques that were used repeatedly, such that they deserve special attention. These methods were the microfabrication of microfluidic chips, wafer pillar height measurement using optical coherence tomography (OCT), imaging using confocal microscopy, and culture and sample preparation. Here, I describe what all these methods involved. Other methods that are relevant to specific chapters will be discussed in those chapters.

2.1 Microfabrication

Most of the experiments in this thesis involved the use of microfluidic chips as either flow channels or confinement chambers for growing filamentous cyanobacteria. To make a microfluidic device, different microfabrication techniques are used, as described in *e.g.* [60]. In this thesis, photo and soft lithography techniques were used to make microfluidic chips and the general fabrication process is outlined here. Experiment-specific modifications to the procedure outlined here will be given in the respective methodology sections of chapters 3, 5, 6, and 7.

2.1.1 Photolithography

Photolithography is a process where light is used to imprint a pattern onto a surface [60]. This involves the use of a photomask, which is designed to have the patterns to be transferred to the surface of interest. A photomask is typically made from a transparent material over which an opaque material is printed to block light in certain areas. The printed patterns were made using computer-aided design (CAD) software, called QCAD [61]. Designs for specific patterns will be given later in the chapters where these designs were used. After designing the patterns in QCAD, the designs were sent to JD Photo Data, a company that fabricated the actual masks. Typically, the designs were printed onto a 5-inch quartz glass plate and printed with Chrome at a resolution of 64,000 dpi (400 nm pixel size) which allowed all features greater than about 5 μm to be printed accurately.

The end product of the photolithography process is a master mould that is used to make

PDMS chips. To manufacture the actual master mould, I used a silicon wafer (10 cm in diameter and 0.5 mm thick) and SU8 photoresist (Microchem) [62]. SU8 is an epoxy-based negative photoresist that becomes cross-linked upon being exposed to UV light, and the unexposed areas can then be washed away by a photoresist developer, a chemical that dissolves the uncrosslinked areas of the photoresist. Positive photoresists behave in the opposite manner: areas that are exposed to UV light become soft and are dissolved by a developer, leaving exposed wafer [60]. Therefore, using SU8 as a photoresist, the areas that were meant to be channels or other open features on the PDMS chip were made to be transparent on the photomask. This allowed UV light to go through the mask and cross-link those areas of the photoresist, forming plateaus on the master mould after development. There are different varieties of SU8 photoresists which differ by their viscosities, ranging from 45 cSt to 12,000 cSt [62]. The viscosity of a photoresist determines how easily the photoresist will flow when being spin-coated onto a wafer, and that affects the thickness of the coating at the end. Therefore, different photoresists can achieve different film coating thicknesses under the same coating conditions. Knowing the thickness of the coating to be achieved helps choose the correct photoresist and the correct spin-coater settings. In this thesis, I used two varieties, SU8-3025 and SU8-3050, which allowed me to achieve coating thicknesses between 20 and 115 μm in a single layer [62].

The process of making the master mould started with cleaning the wafer by blowing high-pressure nitrogen gas onto the surface. The wafer was then dehydrated by placing it on a hotplate set at 200°C for 5 minutes. The dehydrated wafer was then placed into a spin-coater (WS-650MZ-23NPPB, Laurell) that was kept in a fume cupboard to avoid inhalation of harmful solvents. The wafer was held firmly by a low-pressure suction underneath it, which ensured that it did not fly away during spinning. Ideally, the suction is at the centre of the wafer, to allow forces to balance during spinning. Once the wafer was firmly held on the spin coater, a small amount of the photoresist (typically 4 ml for the 10 cm diameter wafer used here) was placed at the centre of the wafer and the spin coater programme was run. The settings on the spin coater programme were different for the different desired thicknesses and for each photoresist used. Here, I will give an example of achieving a uniform film thickness of 60–70 μm using SU8-3025 photoresist. First, the wafer is spin-coated by ramping up to 500 rpm at an acceleration of 100 rpm/s, and the speed is held for 10 seconds. Then the speed is increased to 1000 rpm at an acceleration of 300 rpm/s, and this speed is held for 30 seconds. Finally, the speed is reduced to 0 rpm by decelerating at 300 rpm/s. Other film thicknesses could be achieved by altering the settings as described in the SU8-3000 series datasheet [62].

The coated wafer was then carefully removed from the spin coater and placed onto a hotplate set at a temperature of 95°C for 30 minutes, in a process known as a soft bake. In a soft bake,

any solvent in the photoresist is removed and the layer solidifies. The SU8-3000 datasheet [62] provides different soft baking times for different thicknesses of films. In general, the thicker the layer, the longer the time to evaporate all the solvent in the photoresist. It is recommended to use an open hotplate rather than a convection oven for the soft bake, to avoid the formation of skin over the photoresist surface, which could block the remaining solvent from evaporating, thereby compromising the coating quality [62].

After the coated wafer was fully soft-baked, it was ready for UV exposure through the photomask. I used a mask aligner (SUSS MicroTec MJB4) for UV exposure in this thesis. First, the mask was securely held on the exposure stage under a low-pressure suction. With the mask printed on one side of the quartz plate, as described earlier, it was placed on the exposure stage with the printed surface facing down. This is important because, when the wafer is inserted underneath the mask, such that the two touch one another under gentle pressure, the effects of diffraction of light are minimised during exposure. The wafer was then put onto its holder and inserted into the alignment position, underneath the mask, ensuring that the patterns of interest on the mask were directly above the wafer. The wafer was then exposed to UV light for cross-linking. For most of the wafers used here, with SU8 thicknesses of 40 – 114 μm, total exposure energy between 150 – 250 mJ cm^{-2} was required [62] and this was typically achieved by exposing the wafer for 8 seconds with a light power output of 25 mW cm^{-2}. All the areas of the photoresist exposed to UV light became cross-linked and the unexposed areas remained soft. After exposure, the wafer was baked again, first at 65°C for 1 minute to reduce stress, and then at 95°C for 5 minutes to further harden the layer in a process called the post-exposure bake [62]. Usually, if the process has gone well, the imprinted patterns can be seen on the surface of the layer at this stage.

After the post-exposure bake, the unexposed areas of photoresist were removed by submerging the wafer in a developer (solvent bath) which in this thesis was microposit EC solvent (Rohm and Haas). The solvent dissolves all unexposed parts of the photoresist and the process can be enhanced by either gently shaking the container holding the wafer and the solvent, or by using a sonicator. Here, a sonicator was used to enhance the development process. The length of the time the solvent bath stayed in the sonicator was dependent on the thickness of the layer, and for a thickness of 60–70 μm it was 12 minutes. The final stages of the fabrication process involve washing the dissolved parts of the photoresist away by first rinsing with isopropyl alcohol (IPA) followed by rinsing with de-ionised water. The wafer can then be dried by using a nitrogen jet. The photolithographic process is summarised in Figure 2.1 alongside a photograph of a fabricated master mould that was used in chapter 7.

The method described here allows multiple features to be produced on a single design with

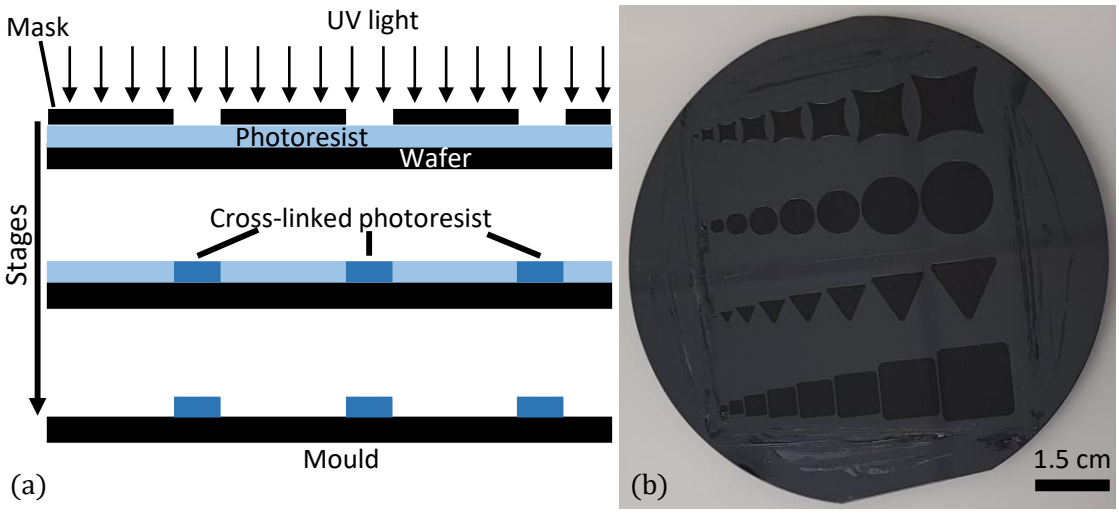

Figure 2.1: Photolithography steps and fabricated mould. (a) Schematic of the photolithographic procedure summarising the mould fabrication process from UV exposure to the development stage, and showing the exposure, baked, and washed wafers, respectively, from top to bottom. (b) An example of a mould fabricated on a 10 cm diameter wafer following the steps in section 2.1.1. The darker shapes are confinement designs made for experiments in chapter 7.

great accuracy, as shown in Figure 2.1(b). It also allows a fabricated master mould to be reused multiple times to make chips which are identical, such that complicated microfluidic devices like a model porous media with thousands of micropillars [63] can be reproduced exactly from a single mould. This ensures that repeated experiments are always conducted under the same physical conditions, limiting the possibility of variations between chips used for the same experiment. Once the master mould was made, the next step was to fabricate the microfluidic chip, as detailed in section 2.1.2.

2.1.2 Soft lithography

In order to fabricate a microfluidic chip, a soft lithography process was followed. First, the master mould was put inside a mixing tray. A soft lithography process was then begun by preparing a liquid elastomer in another clean mixing tray. The liquid elastomer used here was poly-dimethilsiloxane (PDMS), which was prepared by mixing base and curing agent (Sylgard 184, Dow Corning) at a ratio of 10:1. The mixing ratio of the base and the curing agent affects the stiffness of the chip such that the ratio of 10:1 produces PMDS with Young's modulus of $\sim$ 1.5 MPa [64].

After the base and curing agent were mixed thoroughly, the desired amount of the mixture

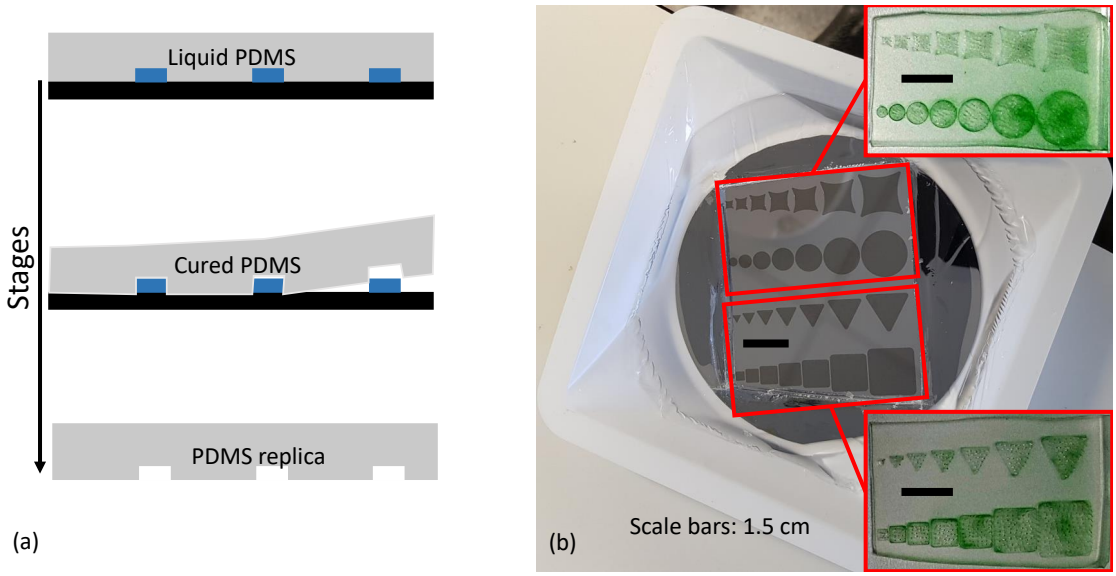

Figure 2.2: Soft lithography process. (a) Schematic of the soft lithography process, starting from pouring liquid PDMS onto the mould, then curing the PDMS, followed by peeling off the PDMS replica, as shown from top to bottom, respectively. (b) An example of a master mould and fabricated microfluidic devices (inserts) filled with cyanobacteria and made from PDMS chips cut out of the master mould are shown. The PDMS chips shown were used for experiments in chapter 7.

(typically $\sim$ 40 ml here) was poured over the master mould, which was stored in another mixing tray. The tray with the master mould and the elastomer was then put into a vacuum chamber for 15 to 30 minutes to degas it so that any bubbles and dissolved air trapped inside the mixture while stirring were removed. Degassing ensures that the chip, when fabricated, has no defects or unintended pores that are caused by bubbles, and that it is optically transparent. The liquid elastomer was then cured by placing it in a convection oven set at a temperature of 75°C for 1 hour. After 1 hour of baking, the PDMS solidified but remained elastic. Using a scalpel, the PDMS was carefully cut around the design region, and the chip was carefully peeled back to end up with a chip and reusable master mould, as shown in Figure 2.2.

The PDMS chip thus fabricated was then further developed into a complete microfluidic device. From this stage, the steps followed to create a microfluidic device differed, according to the needs of the experiment. In some experiments, as in chapter 3, holes were punched into the channel inlets or outlets, using a small hole punching device (shown in chapter 7), while in chapter 7, multiple holes were punched across the well or chamber regions to aid the diffusion of nutrients (see Figure 2.2(b)). Therefore, how the chip was finalised into a completed microfluidic

device depended on the experiment plan and detailed information on these processes will be given in subsequent chapters. Here, I will give the general steps that were followed to complete the fabrication of a PDMS chip into a finished microfluidic device.

The features in the cutout chip remained open along one face, and to complete the microfluidic channels, they needed to be properly sealed. This is where a substrate was used. A PDMS chip can stick to glass or another PDMS block when the surfaces are properly treated, as will be discussed next. Here, I used glass slides coated with PDMS for experiments in chapter 3 and transparent well plates coated with PDMS for experiments in chapter 7. In each case, the surface was coated with a thin layer of liquid PDMS to ensure a constant environment for the cyanobacteria samples, on all surfaces. For glass slides, the coating was done using a spin-coater, where a 5 ml drop of a 10:1 mixture of sylgard 184 base to curing agent was poured on the glass slide and spin-coated at a speed of 2,000 rpm for 30 seconds. For well plates, a small amount of the PDMS mixture was poured onto the surface and the well plate was tilted to ensure that the PDMS flowed and spread across the whole surface. Later the well plate was left to stand for 20 minutes on a level surface to ensure that the film thickness was even across the whole area. The well plate was covered during this time to minimise the accumulation of dust.

Once the glass slides or well plates were evenly coated with PDMS, they were also baked in a convection oven at 75°C for 1 hour in order to cure the PDMS. The fully baked PDMS-coated substrate and the cutout chip were both put in an oxygen plasma cleaner for $\sim$ 8 minutes to activate the surfaces for bonding. PDMS is made up of repeating units of -O-Si$(CH_3)_2$- [65]. Exposing PDMS surface to oxygen plasma introduces silanol (SiOH) groups [65, 66]. When the treated surfaces are pressed against one another, the silanol groups on the surface react to form an irreversible Si-O-Si covalent bond that can withstand pressures between 207–345 kPa [65]. While sticking the two surfaces together, care was taken to ensure that no air pockets were left and that no part of the wells or channels touched the base, as this would collapse the channels. Any external attachments, such as inlet and outlet tubes, were connected at this stage. The result was a complete microfluidic device that could be used for the intended experiment. The master mould was reused to create several identical chips by repeating this process. To know the exact height of the microchannels, I measured the thickness of the photoresist layer on the wafer using optical coherence tomography (OCT), as described in the next section.

2.1.3 Wafer film thickness measurement using OCT

The spin-coating procedure only gives an approximate thickness of the photoresist film. To know the exact thickness of the film or the height of the microfluidic channels, the thickness of the film

needs to be measured. Different techniques can be used to measure the thickness of thin films [67] but here I use optical coherence tomography (OCT) due to its very high axial resolution [68]. OCT is a very high-resolution non-destructive and non-invasive imaging technique that is used to view subsurface structures of semitransparent samples [68, 69]. It is based on the Michelson interferometer, which uses a low-coherence light source to make precise measurements by splitting the light into two paths and then recombining it to form an interference pattern [69]. Notably, the Michelson interferometer is known for its use in an experiment that disproved the existence of an aether in the 19^{th} century [70]. An aether was believed to be a medium that light travels through and most physicists at that time believed that light needed a medium to travel.

OCT has some analogies to ultrasound imaging. However, instead of sound, OCT uses a broadband light source [71]. Compared with ultrasound imaging, OCT achieves a depth resolution of up to a few micrometers [72], which is two orders of magnitude higher than ultrasound. However, the penetration depths are much lower (a few millimeters) compared with other conventional imaging techniques [72]. Nevertheless, the high-depth resolution and non-contact imaging offered by OCT has seen a wide range of applications in fields like medicine [71–73] and art conservation [74–76].

Categorically, OCTs are grouped into two types: Time-domain (TD-OCT) and Fourier-domain (FD-OCT) OCTs [72]. Schematic diagrams of these two kinds of OCTs are shown in Figure 2.3. In both kinds of OCTs, light from a broadband source is split into two parts by a beam splitter (dichroic mirror) [71]. One part of the split light travels towards the sample while the other travels to a reference mirror. The reflected light from both arms travels back to the beam-splitter where they recombine and travel towards the detector. The low-coherence nature of the light ensures that the two beams of light interfere constructively when they have travelled equal distances [71]. In TD-OCT, sample depth information is obtained by moving the reference mirror [72]. On the other hand, in FD-OCT, the reference mirror is fixed and a spectral detector is employed, as shown in Figure 2.3(b). Depth information is obtained by analysing the spectrum of the reflected signals using Fourier analysis, hence the name of Fourier-domain OCT [72]. By fixing the reference mirror, FD-OCT is faster and it is the most common type of OCT [72] and the one used in this thesis.

Samples in OCT imaging are scanned point by point, in a line, to generate a cross-sectional 2D image. Repeating the procedure line by line, multiple cross-sectional images are obtained which can then be combined into a 3D image. Here, I only used 2D OCT images. I used an ultra-high-resolution FD-OCT (centre wavelength of 810 nm and a depth resolution of 1.8 μm in air) [77], developed by the Imaging & Sensing for Archaeology, Art History & Conservation (ISAAC) group at Nottingham Trent University, to measure photoresist film thickness. OCT

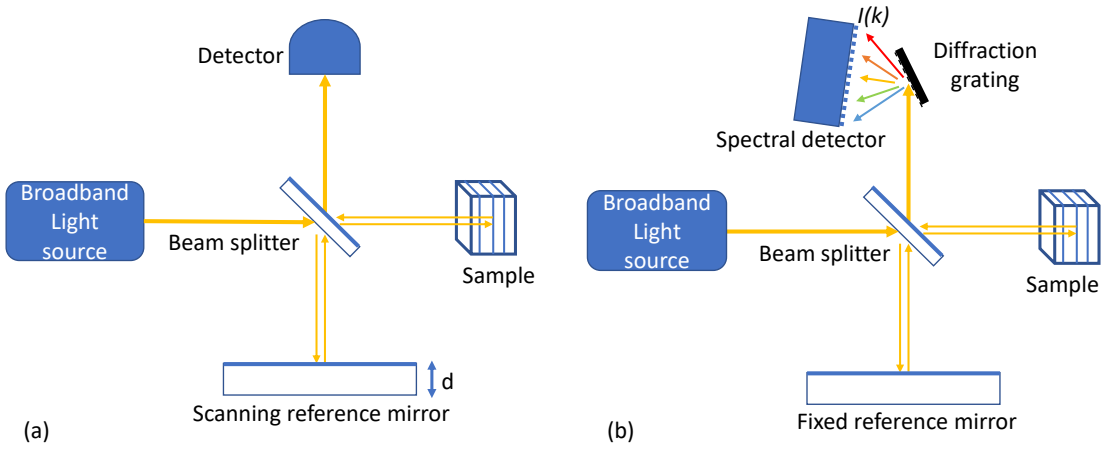

Figure 2.3: Schematic diagrams of time-domain and Fourier-domain optical coherence tomography. (a) Time-domain OCT involves a scanning reference mirror. (b) Fourier-domain OCT uses a fixed reference mirror but has a spectral detector. In this thesis, I exclusively used FD-OCT.

was used because the transparent nature of the photoresist allowed light to go through it and reflect at the interface between the film and the reflective silicon wafer.

On the OCT image, the optical thickness of the sample, or of any layer, is the product of its physical thickness and the group refractive index. The group refractive index of a medium defines the ratio of the velocity of a narrow-band optical pulse in a vacuum to its velocity in the medium [78]. The name group refractive index takes into consideration the multiple wavelengths involved in the travelling optical pulse. Therefore, to measure the actual thickness of the film from an OCT image, the optical thickness of the photoresist layer on the OCT image must be divided by the group refractive index of SU-3000 photoresist at the centre wavelength of the light source (810 nm) which is 1.586 [62, 79].

Alternatively, without the knowledge of the group refractive index, a reference surface may be used. This method involves scanning a sample sitting on a flat reference surface. The scanning is carried out in such a way that the OCT image shows both the sample and the reference surface, as shown in Figure 2.4(b). Therefore, in the case of the master mould, the method would work if there is a film-free area. The actual thickness of the film in this method is measured by first extending a line along the reference surface to underneath the sample, and then measuring the distance between the sample's top surface and the extended line, as shown Figure 2.4(b).

To complete a single line of the scan, the scanner in the OCT system rotates from side to side [80]. The rotation of the scanner causes a flat surface to appear like a curved line on the OCT image. The degree of curvature is more significant with an increased field of view [80]. Therefore,

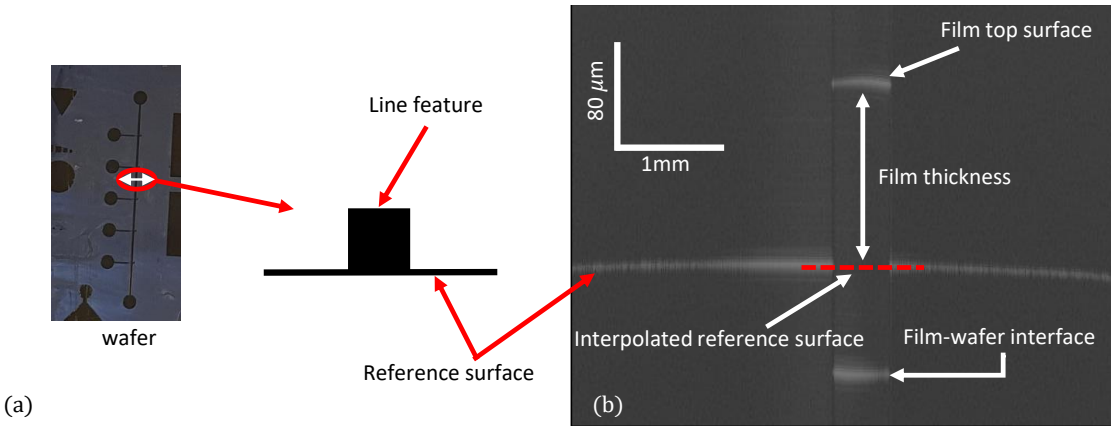

Figure 2.4: Illustration of photoresist film thickness measurement using OCT. (a) A physical scenario is shown involving a wafer with a microfluidic channel design (left) with a double arrow showing the position and the direction of OCT scanning and an illustration of the expected topography at the position of scanning (right). The resulting OCT image would appear as in panel (b). This shows the top surface of the scanned part of the film, the displaced wafer-film interface due to the reduced group velocity of light in the film, a flat reference surface (wafer) which is interpolated beneath the sample, and the marked true thickness of the film.

for very precise measurements of the thickness of the sample using the reference surface method, the OCT image needs to be corrected for apparent surface curvature. This was done by scanning a flat surface that covers the whole width of the image, and the image obtained was then analysed by fitting first and second-order polynomials to the surface profile. The difference between the linear and quadratic fits was used to correct (flatten) all subsequent images taken using that OCT system while the image settings were kept unchanged. Both the methods described here for measuring the film thickness using OCT were used to verify measurements.

2.2 Confocal microscopy

Most of the imaging in this work was carried out using confocal microscopy. As such, this section outlines the general confocal microscopy methods used to acquire images of filamentous cyanobacteria. The methods described here apply to every part of this thesis where confocal microscopy was used. Confocal microscopy is a special type of imaging where images of a sample can be obtained at a specified focal plane [81]. In fluorescence imaging, a sample is excited with light of a particular frequency and the sample emits light at a lower frequency, which is captured by the microscope light detector. The confocal microscope is able to block light emitted from all

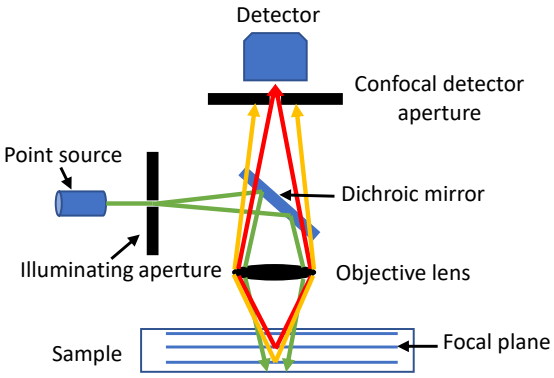

Figure 2.5: A schematic diagram of a confocal microscope.

planes other than the focal plane, subject to its resolution limits [81]. This is achieved through the use of a focal gate or confocal detector aperture, which is a narrow slit (pinhole) sitting next to the detector, as shown in Figure 2.5. In some confocal microscopes, the size of the slit can be adjusted by the confocal user. Increasing the size of the slit allows light originating from multiple planes to reach the detector and that reduces the depth resolution of the confocal microscope. For 2D images, like those mostly captured in this project, the slit width was set to the maximum value (equivalent to a depth of field of 81 μm), to ensure that filaments at different depths were captured in a single scan depth. By scanning plane by plane, confocal microscopes are used to generate 2D images that can be combined to form a 3D image of the sample. A schematic diagram of a confocal microscope is shown in Figure 2.5.

2.2.1 Confocal image acquisition

Confocal images are possible with fluorescent samples. However, not all biological samples are fluorescent [82], although non-fluorescent ones could be made artificially fluorescent by staining them with fluorescent dyes. Samples that are naturally fluorescent are known as auto-fluorescent and these include cyanobacteria. Auto-fluorescence in cyanobacteria is possible due to the presence of chlorophyll-a [83]. When irradiated with green light, the chlorophyll in cyanobacteria absorbs the light and the molecules become excited, which leads to the emission of red light as the molecules decay back to their ground state. The emitted red light, especially from the focal plane under study, is detected by the microscope photo-detector, as illustrated in Figure 2.5. Staining biological samples with a dye for fluorescence imaging could lead to cellular toxicity [84]. Therefore, having a biological sample that is auto-fluorescent, like in filamentous cyanobacteria, is ideal for live-cell fluorescence imaging. In this project, a confocal laser scanning microscope (Leica TCS SP5) was used. Taking advantage of the auto-fluorescence of the cyanobacteria, I

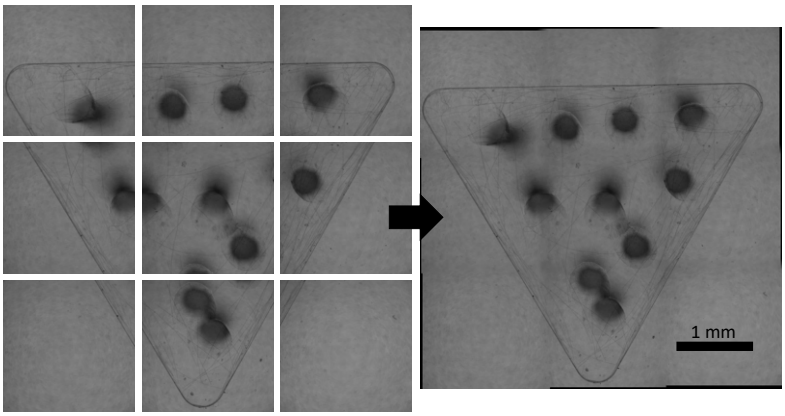

Figure 2.6: Illustration of confocal wide-area scanning. Brightfield channel images are used here for illustration. An area to be scanned was divided into tiles, as shown on the left. The image tiles were scanned one by one with the sample stage moving as automatically controlled by the confocal software (LAS AF). Individual images were later merged to form a single large image, as shown on the right. The image here shows a triangular confinement chamber used for growing cyanobacteria, as discussed in chapter 7.

used 514 nm laser light for excitation and observed the resulting emission through a bandpass filter from 620 to 780 nm. Brightfield images of the sample under study were always collected alongside confocal images. Usually, brightfield images were used for observing the environment around the filaments under study, specifically to view non-fluorescent features such as channel or chamber boundaries, as will be discussed in later chapters.

The confocal microscope also allowed for wide-area imaging, known as tile-scanning, where a marked region of interest of a sample or imaging chamber was partitioned into multiple tiled images, each scanned one at a time and later joined together to form one large image, as illustrated in Figure 2.6. Merging of image tiles into one large image was done automatically in the confocal software (LAS AF). In certain cases, however, image tiles might not be merged correctly. One of the causes for this problem is a lack of static features in the imaging space that the software uses to correlate neighbouring tiles. To resolve this problem, I ensured that each wide-area scan included some static features, such as channel or chamber boundaries. The contrast of the static features was also important for the correct merging of image tiles. I ensured that the brightfield channel image had a strong contrast, for example by changing channel gain. Once confocal images were captured, certain pre-processing steps were carried out before the resulting image could be further analysed. In the next section, I will discuss these image-processing steps.

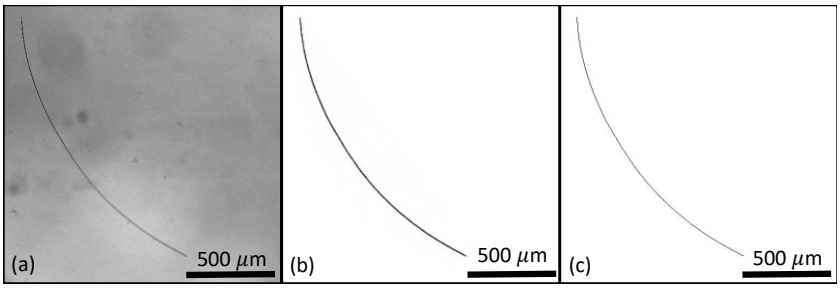

Figure 2.7: Filamentous cyanobacteria (*Oscillatoria lutea*) images and image processing. (a) A bright field image, (b) An inverted confocal image of the same filament, and (c) a binary skeleton of the confocal image.

2.2.2 Confocal image post-acquisition processing

Depending on the depth of the sample being imaged, certain samples could be scanned using a single focal plane. Other samples required scanning at multiple depths, each depth giving a 2D image (z-scan). To get a single 2D image from such z-scans, images were stacked together and compressed vertically to form a 2D image with each pixel intensity being the maximum of the combined z-scans. This was done either using the confocal microscope software, or other imaging processing software like Matlab or ImageJ [85]. Finally, images were processed in Matlab with customised codes, each developed for different purposes in this project. In many cases, for example, grayscale images were turned into binary by applying a threshold after removing noise from the image. Usually, the original confocal images had low noise, as shown in Figure 2.7(b).

As stated in the introduction of this section, bright-field images, like the one shown in Figure 2.7(a), were also used in the analysis, especially to see the environment a particular filament was in *e.g.* whether it was near a boundary. Finally, depending on the needs of the experiment, binary images could be processed further to generate skeletons (*i.e.* representing each filament by a single pixel width line, through the mid-line of the filament's image) as illustrated in Figure 2.7(c). Various computations could be made on either the binary or skeletonised image, as will be demonstrated in subsequent chapters.

2.3 Culture and sample preparation

The strains of filamentous cyanobacteria used in this project were supplied by the Culture Collection of Algae at Göttingen University, also known as the SAG (Sammlung von Algenkulturen der Universität Göttingen). Three strains of filamentous cyanobacteria were used: *Kamptonema animale* (SAG 1459-6), *Lyngbya lagerheimii* (SAG 24.99), and *Oscillatoria lutea* (SAG 1459-3),

with the numbers uniquely identifying the strains in the culture collection [21, 86]. These strains will be referred to as *K. animale*, *L. lagerheimii*, and *O. lutea*, respectively, throughout this thesis. These strains are well-studied, easy to cultivate, non-toxic and associated with microbial mat formation and stromatolites (*e.g.* [29, 30, 45, 87, 88]).

The three strains studied belong to the same order, *Oscillatoriales* [21], and have similar sizes and behaviour as observed in this project. I, therefore, studied the mechanical properties of all three strains in chapter 3 as one way of checking the internal consistency of the methods used. However, due to time limitations, I could not repeat the subsequent sets of experiments for all three strains. Therefore, beyond chapter 3 I chose to focus my study on *O. lutea* because the filaments in this strain grew most easily under the incubation conditions. In general, the three strains behaved in a similar manner. Therefore, the results obtained from *O. lutea* could be extended, with caution, to the other two species.

2.3.1 Culture maintainance

The strains were maintained in a medium of BG11 broth (Sigma-Aldrich) diluted to a ratio of 1:100 with 18.2 MΩcm of ultrapure water, from a PURELAB Chorus 1 Complete water purifier (ELGA LabWater). Following Lorentz *et al.* [89], they were incubated at 20 ± 1°C and with warm-white LEDs (colour temperature of 2800 K) providing a photon flux of 10 ± 2 μmol m^{-2} s^{-1} on a 16h day + 8h night cycle. Figure 2.8 shows an incubator with samples, as used in the project. The incubator was a customised wine fridge (Cookology CWC600BK) with LEDs fitted in to provide the required lighting intensity.

Within the incubator, stock samples were kept in transparent glass bottles of different sizes, between 100 and 500 ml. The nutrients inside the media deplete as the population of cyanobacteria grows. Therefore, samples were transferred to a fresh medium about every 4 weeks. The period could be longer or shorter depending on the initial cyanobacteria concentration at the time of transfer. Usually, for long-term incubation, the initial density was kept low, to increase the period between sample transfers. Under different conditions, long-term cultivation of cyanobacteria can be maintained by reducing their activity *e.g.* by reducing the temperature [89]. This approach to culture maintenance was not used in this project, as an actively growing stock of material was desired, from which samples could be periodically taken for experiments.

2.3.2 Culture transfer and sample preparation for experiments

Transferring samples to new bottles or media needed care, to avoid contaminating the culture. First, a clean surface was prepared and new sterile glass bottles were filled with fresh media,

Figure 2.8: An incubator used to keep samples in this project. The walls inside were covered with reflective aluminium foil to enhance the even distribution of light.

usually to three-quarter capacity. Cyanobacteria samples were then added, usually in a volume ratio of 1:10 with the medium. However, in certain cases where large amounts of samples were needed for immediate experiments, the whole cyanobacteria culture was maintained by just replacing the media in each bottle. Once samples were transferred to a new medium, the new bottle was covered, while ensuring that air could move in and out of the bottle (usually, by leaving the cover cup loosely screwed). This was important because cyanobacteria need air in addition to light, water and nutrients, to make their own food.

While preparing samples for experimental observations, experiment-specific procedures were followed. Such detailed sampling procedures will be provided in the methodology sections of each following experimental chapter.

2.3.3 Disposal of culture

In case of excess culture, these were destroyed by adding a household bleach (Domestos), at a volume ratio of 1:5 to the culture suspension, which killed the cyanobacteria through its active ingredient, sodium hypochlorite [90]. Usually, the samples were left to stand for at least 24 hours after the bleach was added before being disposed of, through the sink. While killing the cyanobacteria, the bleach dissolves the green pigment. Therefore, one indication that the culture is effectively killed is when the green colour disappears. Glass bottles were then disposed of as per institutional disposal policies.

Chapter 3

Structural mechanics of filamentous cyanobacteria

3.1 Introduction

In chapter 1, I introduced filamentous cyanobacteria, and their known physical and behavioural aspects were briefly discussed. In this chapter, I will measure and quantify the key mechanical properties that underlie the behaviour of three typical cyanobacteria species. As a result, the review introducing this chapter will build on that in chapter 1, but with a focus on the mechanics of the filaments. For example, it was noted that there are different models of gliding motility in filamentous cyanobacteria [33–35, 37–39, 41, 42], but the challenge underlying all these models is the need to understand the range of forces that cyanobacteria can generate as they move and change shape. Therefore, in this chapter, I aim to measure the bending stiffness and evaluate the internal distribution of stress and bending energy associated with shape fluctuations in filamentous cyanobacteria. The results of this chapter have been published [91].

No matter what the origin of their motile forces is, mechanically, filamentous cyanobacteria can be considered to act as self-propelled semi-flexible rods. This means that they belong to the class of active polymer or active nematic systems, terms that describe collections of self-driven moving objects with a highly elongated shape (see *e.g.* [92–94]). For such systems, the bending stiffness–also sometimes called flexural rigidity–characterises the flexibility of the filaments and influences their behaviour. As a recent example, the motion of active polymers in porous media has been shown to depend dramatically on their stiffness, ranging from filaments that smoothly move through the pore spaces to those that easily get trapped [95]. This would be of relevance to the design of scaffolds for microbial fuel cells [96, 97], to determine pore sizes that can effectively trap filaments but still allow for the flow of dissolved gasses, for example.

In section 1.2 it was also noted that through collective interaction, filamentous cyanobacteria self-organise into colonies or biofilms, symbiotic communities found in a wide variety of ecological niches [45]. The dense colonies of these structures are characterised by vortices and bundles

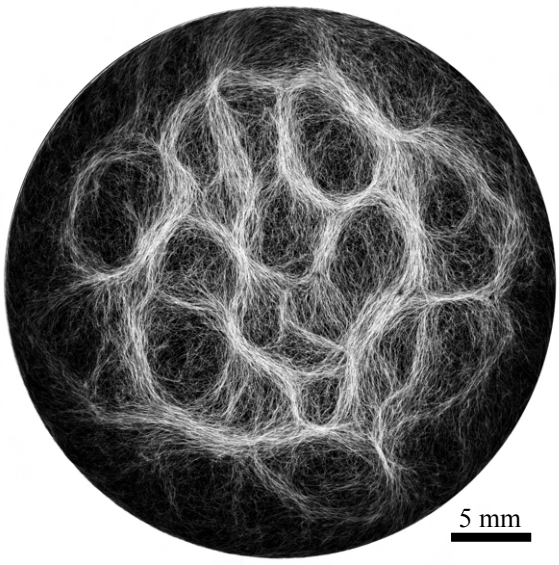

Figure 3.1: An example of filamentous cyanobacteria collective structure in *Oscillatoria lutea*, showing a reticulate pattern. Reproduced from [91].

forming reticulate patterns as shown in Figure 3.1. The mechanical response of the filaments was identified as one of the factors that contribute to self-organisation, for example in determining how one filament will bend when in contact with other filaments or with obstacles [47]. Further, biofilms and biomats in general show some remarkably conserved macro-mechanical properties, typically behaving as viscoelastic materials with a relaxation time of about 20 minutes [98]. However, there has been a lack of any corresponding systematic measurement of the micro-mechanical properties of filamentous cyanobacteria, to the point where such properties are typically just assumed when needed in models (*e.g.* see [47]). This chapter seeks to fill that gap by providing carefully measured values of the mechanical properties of individual filaments of cyanobacteria.

In general, the focus here is on the equilibrium structural mechanics, or statics, of filamentous cyanobacteria, while their dynamics will be discussed in the following chapters. In particular, I look at the bending stiffness of the cyanobacteria, treating them as slender bodies, or flexible rods. For this, custom microfluidic flow cells were developed, in which I studied how the bacteria are reversibly deflected by the drag forces of fluid flowing past them. I then connect their bending stiffness to the mechanical response of their cell walls. For this, I quantify Young's modulus of the filaments, through nanoindentation techniques, and show that the stiffness of the cell walls provides most of the filament's resistance to bending. Finally, I look at the shapes of cyanobacteria filaments in different scenarios and connect these shapes to their internal distribu-

tions of forces. All the three species introduced in section 2.3 (*Kamptonema animale*, *Lyngbya lagerheimii* and *Oscillatoria lutea*) will be studied here and their results will be compared, for the purpose of checking the consistency of the methods.

In the remainder of the introduction to this chapter, I will present a detailed overview of two areas that were critical to the measurement of the mechanical properties of the cyanobacteria filaments. The first topic involves the approximation of a filament as a slender body and presents the mathematical framework needed to model the resulting force balance problem. The second topic is atomic force microscopy, and I will outline how this tool can be used to map the mechanical properties of a surface, like the cell wall of a bacterium.

3.1.1 Filament bending and flow in a microfluidic channel

Theory of a bending slender rod

Here, the theoretical framework used to evaluate the mechanical properties of filamentous cyanobacteria will be outlined. A strand of bacteria is treated as a slender elastic rod [99], whose shape is defined along an arc or contour length coordinate s by its position $\boldsymbol{x}$. Other geometric variables include the normal vector, $\hat{\boldsymbol{n}}$, the orientation $\theta(s)$ of the tangent vector $\hat{\boldsymbol{t}} = \mathrm{d}\boldsymbol{x}/\mathrm{d}s$, and the curvature $\kappa(s) = \mathrm{d}\theta/\mathrm{d}s = (\mathrm{d}^2\boldsymbol{x}/\mathrm{d}s^2) \cdot \hat{\boldsymbol{n}}$, as sketched in Figure 3.2. The radius of curvature of the filament, $R(s) = 1/\kappa$.

External forces and internal moments can both act to bend an elastic filament. Specifically, if w is an external force per unit length, applied normal to the filament, this will generate a bending moment M, such that

$$\frac{\mathrm{d}^2 M}{\mathrm{d}s^2} = -w. \tag{3.1}$$

This moment, along with any internally generated moments, will bend or flex the filament, whose mechanical resistance is given by its bending stiffness or flexural rigidity, β. In mechanical equilibrium, and assuming a linear elastic response, this balance can be given as

$$M = -\beta(\kappa - \kappa_0) = -\beta\tilde{\kappa}, \tag{3.2}$$

where κ_0 is any intrinsic curvature (*i.e.* it describes the shape of the filament in the absence of external forces), and where $\tilde{\kappa}$ is the change in curvature away from this reference configuration. Equivalently, the deformation energy, per unit length, is

$$\mathcal{U} = \frac{1}{2}\beta\tilde{\kappa}^2. \tag{3.3}$$

This bending means that one side of the filament, on the inside of the bend, will be under compression, whereas the opposite side will be in tension or extension.

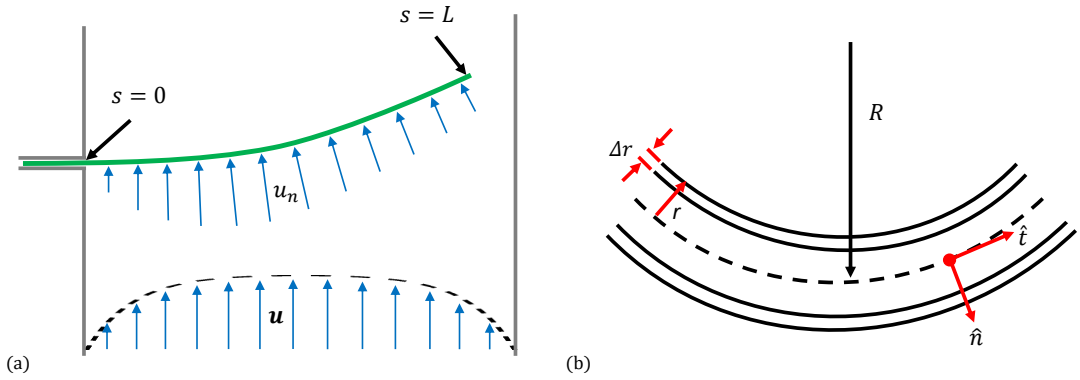

Figure 3.2: Modelling cyanobacteria bending and structure. (a) The filament of bacteria is treated as a slender rod of length L, which bends under a drag force arising from the normal component of the channel flow, u_n. (b) The close-up of the filament is approximated as a hollow cylinder of radius r and wall thickness Δr. The radius of curvature ($R = 1/\kappa$), tangent ($\hat{\boldsymbol{t}}$) and normal ($\hat{\boldsymbol{n}}$) vectors are defined with reference to the neutral axis of the cylinder, which follows path s. Reproduced from [91].

In my experiments, external drag forces are generated by the flow of water past a filament of cyanobacteria, confined in a channel. The Poiseuille solution for the flow field $\boldsymbol{u}$ expected in my channels, with rectangular cross-section, will be developed and validated in 3.2.2. The filament is treated as a flexible cylinder of radius r surrounded by water of density ρ and dynamic viscosity μ, which is flowing towards the filament with a normal velocity component $u_\mathrm{n}(s)$. In the viscous limit, the flow of water around the filament will produce a drag force per unit length of

$$w = \xi u_\mathrm{n}, \tag{3.4}$$

where ξ is the coefficient of resistance or friction coefficient (alternatively, $\xi = \rho r u_\mathrm{n} C_\mathrm{D}$ for drag coefficient C_D). At low, but finite, Reynolds number, $\mathrm{Re} = 2\rho r u_\mathrm{n}/\mu \ll 1$, the drag of an infinite cylinder is well-approximated [100–102] by

$$\xi \cong \frac{4\pi\mu}{\log(7.4/\mathrm{Re})}. \tag{3.5}$$

In my system, using a filament radius of 2.2 μm and a maximum flow speed of 2.6 mm s^{-1}, I maintain $\mathrm{Re} \leq 0.01$. Equation 3.5 is also appropriate for filaments of finite lengths L where $L/r \gtrsim \mathrm{Re}^{-1}$, as holds in my case (otherwise a simpler form could be adapted, as in [103, 104], based on the slenderness ratio L/r).

Finally, one of my aims is to compare the bending stiffness of a strand of cyanobacteria to the contributions expected from its cell wall. For this, if I treat the cell wall as a thin, hollow

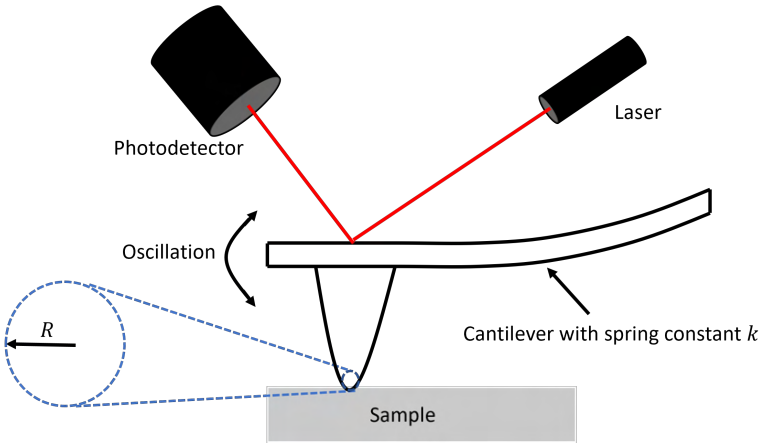

Figure 3.3: Schematic representation of tapping mode AFM. The probe oscillates up and down as it probes the sample surface. The cantilever has a spring constant k and the tip has an effective radius R.

cylinder of radius r, thickness Δr, and Young's modulus E, it will have a bending stiffness

$$\beta = \pi E r^3 \Delta r \tag{3.6}$$

assuming that $\Delta r \ll r$ [105, 106].

3.1.2 Atomic force microscopy for stiffness measurement

Atomic force microscopy (AFM) is a very high resolution (up to fractions of a nanometer) imaging technique under the family of scanning probe microscopes [107, 108]. There are a number of different modes or techniques of AFM imaging developed specifically to measure different sample properties and surface topography [109]. This project used an AFM operating in the tapping mode, where the AFM probe continuously oscillated up and down so that the AFM tip taps on the sample surface with a variable force [110] as shown in Figure 3.3.

In this project, the technique used for measuring the mechanical properties of the samples was the force-distance method [111]. In this method, the force that the AFM tip exerts on the sample during the up and down motion is measured by the AFM system from the spring constant of the cantilever k and its bending [112]. On the other hand, the bending of the cantilever is measured through a photodetector that captures the intensity of the light reflected from the reflective surface on the back of the cantilever [112]. The captured light intensity is then converted into a deflection value using a calibrated deflection sensitivity value [113] (to be discussed later in section 3.2.3). In general, the optical system is also used to measure the deflection of the cantilever for estimating the force exerted on the sample, and also the vertical

displacement of the AFM tip from a reference point within the AFM system [112]. The estimated force and displacement measurements constitute the force-distance curves. Figure 3.4 gives an example of force-distance curves.

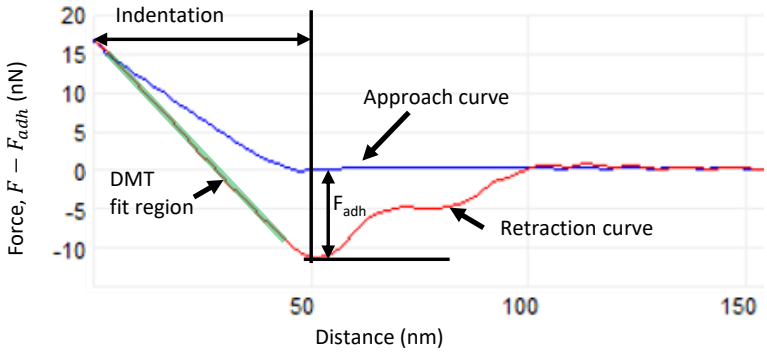

Figure 3.4: Example AFM force-distance curve. The DMT model, Equation 3.7, is fitted to the force-distance curve as the probe is withdrawn from the sample (retraction curve) around the region marked in green.

As illustrated in Figure 3.4, AFM force-distance curves are made up of two curves: one for showing the forces during the approach or downward motion of the probe and the other for the retraction of the probe [112]. A full cycle starts the AFM probe approaching the sample from the air with the force exerted on the sample $F = 0$ up to when the tip touches the sample and the cantilever starts to bend while the force F is increased up to the maximum force (peak-force) [111]. A plot of the force applied on the sample against the displacement of the AFM tip gives the approach curve. Once F reaches the peak force, the AFM probe is withdrawn and the F goes down to zero [111].

However, adhesion forces F_{adh} between the AFM tip and the sample [114] still hold the AFM cantilever to the sample, forcing it to bend downwards during retraction, until the retraction force at the AFM tip and sample interface exceeds the adhesion forces [111]. Once the adhesion forces have been overcome, the AFM probe moves up and the cycle is repeated. A plot of the resultant force $F - F_{adh}$ during retraction is called the retraction curve (red curve in Figure 3.4). In general, the force plotted in the force-distance curves like in Figure 3.4 is the resultant force $F - F_{adh}$, where $F_{adh} = 0$ during the approach. The force-distance curves are captured at every spot the AFM probe presses on the sample and are used to retrieve mechanical properties of the sample like the stiffness and adhesive forces [112]. The procedure is also capable of recording surface topography by mapping all the heights across the sample surface [113].

Retrieving the elastic modulus from the force-distance curves requires the use of models that

take into consideration of the tip geometry and surface forces. A number of models have been developed that are applicable to different systems [115–117]. The simplest model is based on Hertz theory [115] which assumes that the AFM can be treated as a sphere in contact with a hard surface. Hertz theory does not take into consideration any adhesion or surface forces, which makes it less applicable to this study, as there are significant adhesion forces ($\sim$ 10 nN) between cells and the AFM tip as shown in Figure 3.4. Johnson-Kendall-Roberts (JKR) theory [116] accounts for adhesion, but only in the limit of low stiffness and large tip radii. The theory that is most appropriate here is the Derjaguin-Muller-Toporov (DMT) model [117]. The DMT model is similar to the Hertz model but also incorporates adhesion forces. Mathematically, it is given as

$$F - F_{adh} = \frac{4}{3} E^* \sqrt{R(d - d_0)^3} \tag{3.7}$$

where $F - F_{adh}$ is the relationship between the applied force F and the adhesive force between the AFM tip and the sample F_{adh}, $d - d_0$ is the indentation depth, R is the tip radius, and E^* is the reduced modulus. The model is fit to the region marked green in Figure 3.4), where F and F_{adh} are well related. This model represents the deformation that occurs both in the sample and the AFM tip. As such, mathematically, the reduced modulus is defined as

$$E^* = \left(\frac{1 - \nu_s^2}{E_s} + \frac{1 - \nu_t^2}{E_t} \right)^{-1} \tag{3.8}$$

where E_s and E_t are the sample and tip Young's moduli, respectively, while ν_s and ν_t represent sample and tip Poisson. The Young's modulus of the tip is assumed to be infinite [113] (tip made from silicon) hence the second term in the brackets of Equation 3.8 can be ignored and the equation simplifies to $E^* = E_s/(1 - \nu_s^2)$. As an indentation substrate, I treat the filament as an elastic half-space, which is an accurate approximation for spherical indentation into a cylinder when the effective radius of the indenter is significantly (in practice, at least five-fold [118]) larger than the radius of the cylinder [118–120]; my probe tip radius is approximately 20 nm, and the radius of the cyanobacteria filaments is about 2200 nm. This technique can be used to measure the elastic modulus of samples ranging from 700 kPa to 70 GPa [113]. To actually measure the mechanical properties of a sample on an AFM, the instrument needs to be calibrated, as described in section 3.2.3.

3.2 Methods

3.2.1 Culture and sample preparation

Three species of filamentous cyanobacteria were used: *Kamptonema animale* (SAG 1459-6), *Lyngbya lagerheimii* (SAG 24.99), and *Oscillatoria lutea* (SAG 1459-3). Culture labels refer to

strains held at the culture collection of algae in Göttingen (SAG) [21]. They were maintained in a medium of BG11 broth (Sigma-Aldrich) diluted to a ratio of 1:100 with deionised water. Following Lorentz *et al.* [89] they were incubated at $20 \pm 1°C$, with warm-white LEDs (colour temperature of 2800 K) providing light with a photon flux of 10 ± 2 μmol m^{-2} s^{-1} on a 16 h day + 8 h night cycle. For sampling, the material was transferred into a 100 ml glass bottle half-filled with medium and shaken mildly so that the filaments were separated, but not otherwise damaged. Samples were then drawn out, typically in a 0.5 ml syringe, for experimental use.

3.2.2 Bending stiffness measurement using a microfluidic flow device

Microfluidic chip preparation

The microfluidic devices (Figure 3.5) used here to measure the bending stiffness of cyanobacteria are inspired by similar devices used for the characterisation of the elastic properties of pollen tubes [121] and *E. coli* [105, 122]. The design shown in Figure 3.5 was made in CAD software, QCAD [61] and printed on a chrome-quartz photomask. From the mask, a master mould was made in a UV-cured photoresist (Microresist SU-8 3025 and 3050) following the procedure given in section 2.1.1. Individual chips were made by pouring poly(dimethylsiloxane) (PDMS, Dow Sylgard 184) over the template and degassing the result under vacuum before curing at 75°C for 1 hour, a process described in detail in section 2.1.2. The chip was then cut out and holes were punched at the inlet and outlet points, through which tubing was connected. Finally, the chip was primed in an oxygen plasma, together with a PDMS-coated glass slide, and these two components were bonded together to form a complete device, as shown in Figure 3.5(c).

The chips were designed around a simple rectangular flow channel, much wider (300 μm) than it is tall (two designs with channel heights 72 ± 2 and 134 ± 3 μm), with well-separated inlets and outlets allowing for an even flow to develop (channel length of 30 mm). The inlet was connected to a syringe pump, while tubing from the outlet led to a beaker to collect waste. Part-way along the channel is an injection point where a filament of cyanobacteria can be threaded into the channel, from a syringe containing a dilute suspension of the cyanobacteria. The fluid flow inside the microfluidic channel created can be measured, for example using techniques such as particle image velocimetry (PIV) [123]. However, this is not practical in repeated experiments like these where each time a new flow profile has to be measured. Instead, I used an estimated flow profile through the channels from a known volumetric flow rate, as described and validated in the following sections.

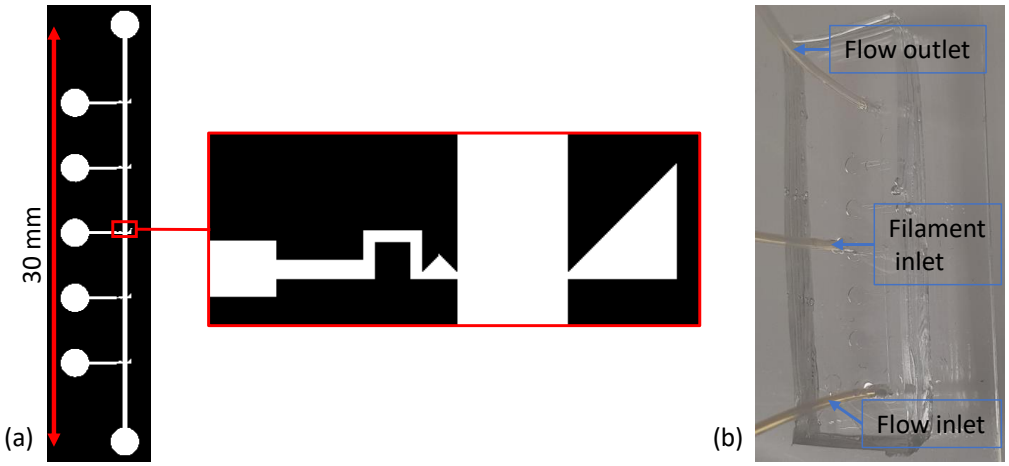

Figure 3.5: A snapshot of CAD design for a flow channel used in this project. (a) The full-flow cell design has multiple filament entry points and channels shown in white. Only the middle injection point was used in this project and to the right is an expanded view of the flow channel design, showing a U-bend for anchoring cyanobacteria filaments. The wedge on the right of the expanded view was created for possible three-point testing but this method was not pursued. (b) A snapshot of a completed microfluidic flow device with tubes connected to the flow inlet and outlet holes, as well as the filament inlet hole.

Flow profile inside the channel

To calculate the flow profile around the filaments I make use of Boussinesq's series solution for Poiseuille flow in a rectangular channel [124, 125]. The flow along a channel of width W and height H, with a coordinate system centred at its midpoint, such that $-W/2 \leq x \leq W/2$ and $-H/2 \leq z \leq H/2$, can be given by

$$u_y = \frac{4W^2U_0}{\pi^3 k} \sum_{n=1,3,5,\ldots}^{\infty} \left(\frac{(-1)^{(n-1)/2}}{n^3} \left[1 - \frac{\cosh(n\pi z/W)}{\cosh(n\pi H/2W)} \right] \cos(n\pi x/W) \right) \tag{3.9}$$

Here, U_0 is the average flow speed in the channel, set by the rate of the external syringe pumps, and k is an effective permeability given by

$$k = \frac{W^2}{12} \left(1 - \frac{192W}{\pi^5 H} \sum_{n=1,3,5,\ldots}^{\infty} \frac{\tanh(n\pi H/2W)}{n^5} \right). \tag{3.10}$$

This solution is appropriate for laminar flows. For the fastest flows in my devices $U_0 \simeq 3$ mm s^{-1}. Using the hydraulic diameter $D_\mathrm{h} = 2WH/(W+H)$ to calculate the Reynolds number $\mathrm{Re_c} = \rho U_0 D_\mathrm{h}/\mu$ of the channel flow gives a maximum $\mathrm{Re_c} \approx 0.5$, well within the laminar limit.

To determine an appropriate number of terms and grid spacing to use for approximating Equation 3.9, I first picked a representative volumetric flow rate Q flowing through a rectangular

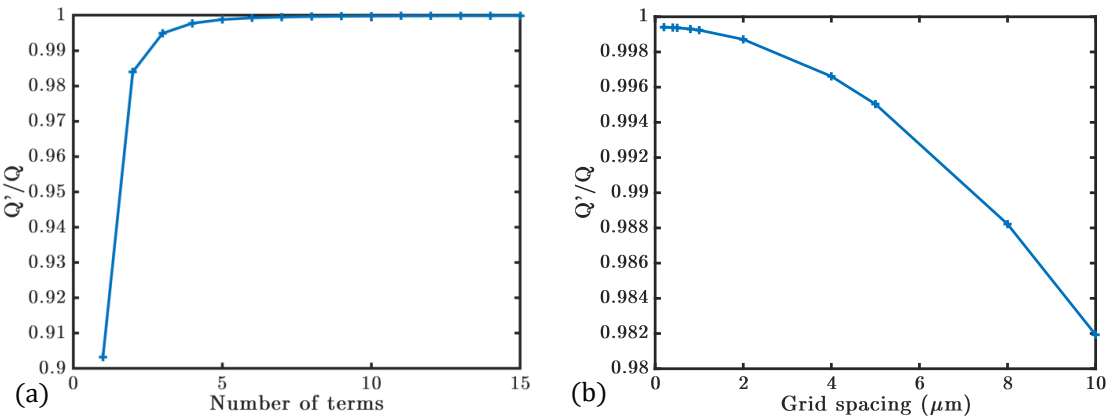

Figure 3.6: Convergence of the flow field series. (a) The series in Equation 3.9 converges quickly, such that 10 terms can be used to approximate Equation 3.9 to an accuracy of over 99.9 % for a spacing of ≤ 1 μm. (b) By truncating the series after 10 terms and varying the grid spacing it is seen that a grid spacing ≤ 1 μm gives a total flow rate that is within 0.1% of the theoretical value. A grid spacing of 0.1 μm and a sum of the first 10 terms of Equation 3.9 were used to analyse the experiments.

channel cross-section at an average speed U_0. I then computed the total flow rate Q' across the entire cross-section using a different number of terms in Equation 3.9 but with a fixed grid spacing of 1 μm. The calculated volumetric flow rate, summed over the whole channel, is then compared with the representative volumetric flow rate by computing the ratio Q'/Q. Results are plotted in Figure 3.6(a), where it can be seen that the series converges quickly and that summing the first 10 terms in Equation 3.9 gives an error of $\leq 0.1\%$. Similarly, I then fixed the number of terms to 10 and varied the grid spacing and again computed Q'/Q. Results shown in Figure 3.6(b) indicate that a grid spacing of ≤ 1 μm and a sum of up to 10 terms of Equation 3.9 gives a flow field that is over 99.9% accurate. Therefore, a choice of grid spacing of 0.1 μm and the series sum of 10 terms in Equation 3.9 was used to approximate flow profile u_y throughout this chapter.

Validation of the flow profiles

The pump used in this project was pre-calibrated for volumetric flow rate using a 0.5 ml syringe. The volumetric flow per step was found $9.39 \pm 0.30 \times 10^{-4} \mu$L/step (mean $\pm$ SE). To be sure of the actual flow rate through the microfluidic channel, I conducted a validation test. The validation process involved flowing a suspension of fluorescent particles (1.9 μm in diameter) through the

microfluidic channel at a fixed flow rate of 93.9 ± 3.0 μL/h (the step motor was set to the speed of 100000 steps/h). The motion of the microparticles along the central horizontal plane was captured by a confocal microscope (Leica TCS SP5). For these green microparticles, 405 nm laser light was used for excitation while a detection bandwidth of between 450 and 650 nm was used. A resonant scanner operating at 8 kHz was employed for quick data acquisition, suitable for particle tracking, as required in this part of the project. A frame interval of 37 milliseconds, including exposure time, was achieved.

Images were captured via two channels, the bright field mode and the fluorescent mode. Bright-field images were used for distance calibration while particle tracking was done using images from the fluorescent channel. An example of images captured is shown in Figure 3.7(a). Particle tracking was carried out using PIVlab software [126]. This Matlab-based software minimises the distance moved by particles in a field between two successive frames and calculates the distance moved by particles in terms of pixel distance. By applying calibrations both in space and time, the flow field in a region of interest can be retrieved. The flow field along the mid-horizontal plane of the microfluidic channel, with a cross-section of 300 μm $\times$ 134 μm, is shown in Figure 3.7(b). By taking a line profile across the width of the channel and averaging across 100 frames, the plot shown in Figure 3.7(c) was generated. There was a low-density distribution of particles along the edges of the channel as can be seen in Figure 3.7(a). The PIVlab software extrapolated flow velocities near the channel boundaries and this resulted in a flat region of the velocity profile near the channel boundaries as shown in Figure 3.7(c). I, therefore, excluded the extrapolated regions of the measured profile and fitted the first term of Equation 3.9 with U_0, $W + W_s$ and $H + H_s$ as fit parameters. Here, W_s and H_s are unknown slip lengths in the width and height of the channel respectively, while W and H are known values of channel width and height, respectively. The resulting fit was extrapolated to cover the whole width of the channel as shown in Figure 3.7(c) and was compared with the theoretical profile for the same average flow rate, calculated using Equation 3.9.

As a check, I compared the known volumetric flow rate from the pump of 93.9$\pm$3.0 μL/h (mean $\pm$ SE) with a measured volumetric flow rate found by extrapolating the measured flow profile shown in Figure 3.7(b). The measured volumetric flow rate was found to be $2.60 \pm 0.02 \times 10^{-11}$ $\mathrm{m^3\ s^{-1}} \equiv 93.5 \pm 0.7$ μL/h (mean $\pm$ SE), which is consistent with the known volumetric flow rate and the measured mean volumetric flow rate is within 0.5 % of the known value.

The measured volumetric flow rate only validates the total flow. However, from Figure 3.7(c), it can be seen that the measured flow profile has the same shape as the expected flow field in the central region of the channel but does not obey the no-slip boundary condition, rather it displays a partial-slip nature. This is not something new in microfluidics, as the no-slip

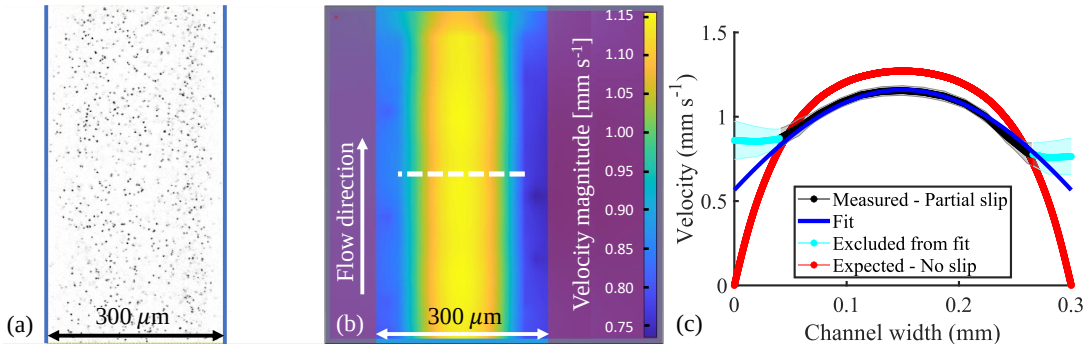

Figure 3.7: Validation of the flow field in a rectangular microfluidic channel. (a) Example image showing microparticles flowing inside a flow channel. Few particles were moving close to the channel boundaries. (b) Flow field along the mid-plane of a 300 μm $\times$ 134 μm rectangular microfluidic channel, for a flow rate of 93.9 ± 3.0 μL/h (mean $\pm$ SE), as measured using PIVlab. (c) Line profile along the dashed line in (b) (black), averaged over 100 frames, plotted alongside the expected flow with a no-slip boundary assumption (red). The grey shaded area in the measured flow profile represents the standard deviation from 100 frames and was plotted using Matlab code, ShadedErrorBar [127]. The fit using Equation 3.9 was applied to the measured flow profile (black plot), excluding the regions near the boundary.

boundary condition is well approximated at the macroscale, but not at the microscale [128, 129]. In microfluidics, certain factors were found to contribute towards partial-slip flow. For example, hydrophobic microfluidic walls have been found to induce a partial-slip flow, while hydrophilic walls did not [130]. PDMS surfaces are slightly hydrophobic in nature, therefore it is plausible that they should induce a slip like the one seen in Figure 3.7(c). Other factors such as surface roughness, dissolved gas and bubbles, or shear rate are also known to affect slip (see Ref [128]). As shown here, it is easier to estimate the flow field from Equation 3.9 than to measure the flows for every volumetric flow rate and for every plane inside the channel. I, therefore, used Equation 3.9 to estimate flow fields inside the microfluidic channel for all the measurements in this project. The justification for this choice will be given in section 3.3.1 where I will compare measurements made using the no-slip flow profile from Equation 3.9 and a measured partial-slip flow profile using PIV.

Bending measurements

Cyanobacteria filaments were threaded into the channel, from a syringe containing a dilute suspension of the cyanobacteria; the syringe was operated by hand until only one filament was

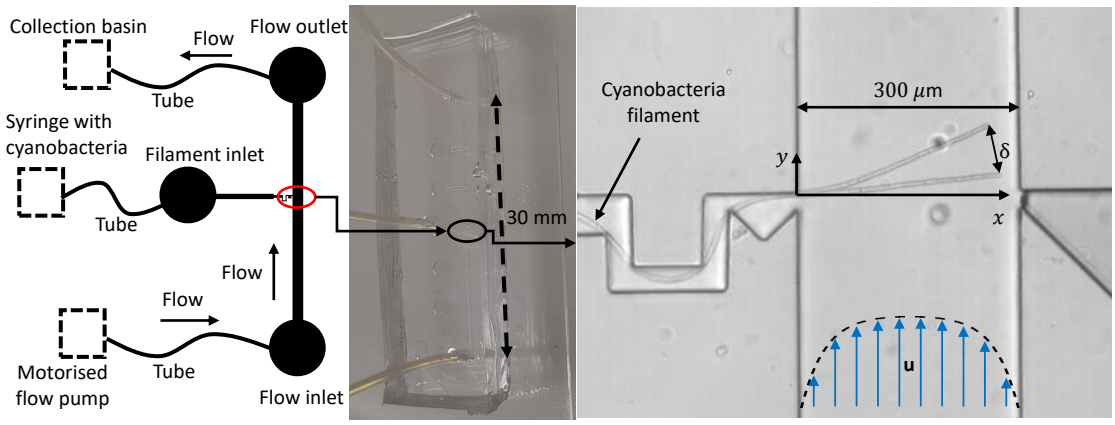

Figure 3.8: Microfluidic flow cell. The sketch to the left gives a schematic of the flow cell, showing how the components were connected. In the middle is an image of a fully fabricated microfluidic device. The close-up view to the right highlights the interactions between a cyanobacteria filament and the flow in the channel. The filament is introduced through a narrow inlet, which has tight corners to pin it in place and anchor it at the point along the wall where it enters into the main channel. The view here of the chip in use is a superposition of two white-light microscopy images of the rest and deflected configurations of a single filament, as it is pushed by a laminar flow $\boldsymbol{u}$ travelling along the y-axis of the channel. Reproduced from [91].

allowed to protrude into the flow channel. In order to enter the channel, the cyanobacteria filament had to bend around a narrow U-bend, designed to anchor it at the channel wall. A sketch of the design, along with a snapshot of a chip in use, is given in Figure 3.8.

The setup used meant that for any experiment a single isolated strand of cyanobacteria was under observation in the flow cell, well-anchored to one wall and crossing close to perpendicular across most of the channel. This filament was then pushed on and deflected by a flow of water in the channel, using average flow speeds between 0.48 and 2.59 mm s^{-1}. A flow test consisted of a series of alternating flowing and stopped conditions, such as those given in Figure 3.9.

In order to minimise any systematic effects of plastic deformation (as observed in *e.g.* [105] for *E. coli*), the sequence of flow speeds used during any experiment was randomised, and between each condition, the flow was turned off to allow the filament to relax back to an equilibrium or rest position as shown in Figure 3.9. For analysis, images of the filament in equilibrium and deflected configurations were collected using a confocal laser scanning microscope (Leica TCS SP5), as described in section 2.2.1. By scanning the focal plane, this method also allowed me to measure the height at which the filament entered the channel. The images were thresholded

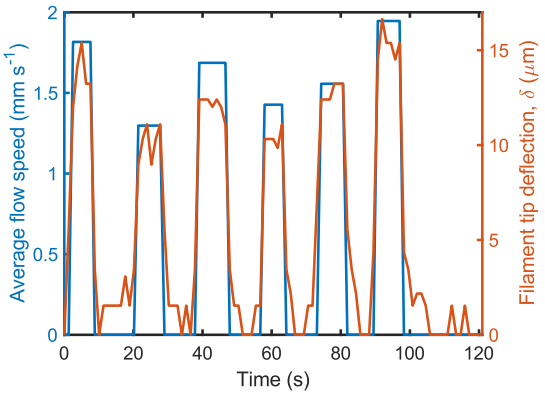

Figure 3.9: Flow test sequence. Each flow test consisted of a sequence of different flow speeds, separated by stopped-flow conditions, while I tracked the deflection of a single filament of cyanobacteria in the channel. As shown here, the total deflection was proportional to the applied flow. Reproduced from [91].

and skeletonised in Matlab, as described in section 2.2.2, in order to have the filament shapes expressed as a set of pixel coordinates along a path s of length L, under different flow conditions.

3.2.3 Nanoindentation

The nanoindentation experiments were carried out using a Bruker AFM (Bruker Dimension Icon, Bruker Inc.). Specifically, I used the quantitative nanomechanical mapping (QNM) mode (*e.g.* see [113,131,132] and section 3.1.2 for further details). The first decision to be made was choosing the most appropriate AFM cantilever for the sample under study. The filamentous cyanobacteria's cell wall is made up of membranes and a more rigid peptidoglycan layer, whose Young's modulus was anticipated to lie in the range 5–50 MPa [133–138]. Therefore, the cantilever should be able to measure elasticity of materials in this range. The best candidate amongst the available AFM cantilevers was Bruker's RTESPA-150, with a nominal spring constant of 5 N/m, and suitable for $5 \leq E_s \leq 500$ MPa [113]. The cantilever was mounted on its holder and aligned as instructed in the user manual [113].

Calibration started with the cantilever deflection sensitivity, as discussed in section 3.1.2. The cantilever deflection sensitivity is a property of the light detection system of the AFM, which is used to measure the bending of the AFM cantilever. It is dependent on the positioning of the AFM cantilever, such that if the cantilever or the optics are moved then the calibration should be repeated [114]. The cantilever tip was pressed against a very hard test surface, here sapphire, and the deflection sensitivity was entered into the system. The spring constant of the

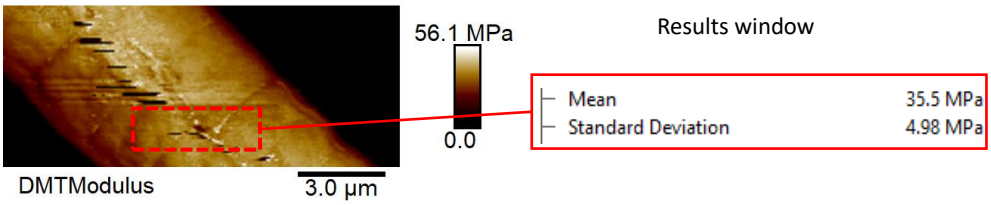

Figure 3.10: Stiffness analysis using Bruker's Nanoscope analysis software. Left: A map of the DMT modulus retrieved automatically by fitting Equation 3.7 to each force-distance curve, at every pixel shown in the selection. Right: part of the results window showing the mean and standard deviation of the DMT modulus, from the selected area. The standard deviation is used as the uncertainty of the measured modulus values that will be given in section 3.3.2. Reproduced from [91].

cantilever, k, was calibrated using the thermal tune option of the AFM. The typical value for k for RTESPA-150 is 5 N/m but can lie in the range 1.5–10 N/m [113]. I then employed a relative method of measuring Young's modulus of samples which compares the stiffness of the sample under study to a reference sample e.g. PDMS [113]. An alternative method of measuring Young's modulus is the absolute method, which requires accurate measurement of the cantilever tip radius (usually done by scanning a rough sample) and the spring constant (done by thermal tuning, especially for soft cantilevers) [113]. The advantage of the absolute method is that it does not require a reference sample, which might be affected by factors such as ageing [113]. The relative method, on the other hand, avoids accumulated errors from uncertainties in the tip radius and spring constant measurements [113].

Using the reference method, a PDMS reference sample was probed to a selected indentation depth between 25-50 nm (typically 50 nm), and the effective tip radius and/or cantilever spring constant were adjusted to match its known Young's modulus of 3.5 MPa. The adjustment of either the tip radius R or the cantilever spring constant k works here because measurement of the Young's modulus is influenced by the ratio $k/\sqrt{R}$. Therefore, the ratio of the two parameters that yield a measurement matching the known modulus of the reference sample is important. The choice of my indentation depth was based on the expected cell wall thicknesses of a few tens of nm, which meant that probing to 25–50 nm should be sensitive to the elasticity of deeper layers of the cell wall, like the peptidoglycan layer. As will be seen in section 3.3.2, the measured Young's modulus across the given indentation depth range is consistent, suggesting that I was probing the same type of material in all the indentation depths.

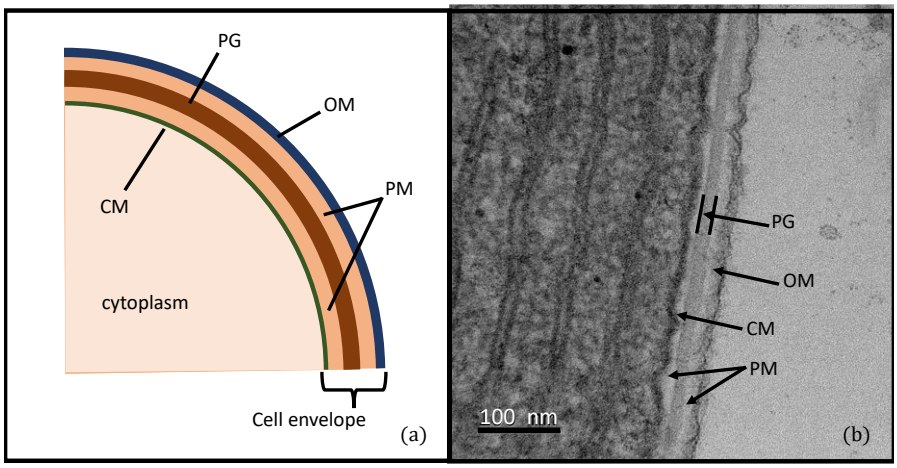

Figure 3.11: Internal structure for cyanobacteria. (a) A schematic representation of the different layers of the cell envelope. (b) A TEM micrograph of *K. animale* Abbreviations: PG, peptidoglycan layer; CM, cytoplasmic membrane; OM, outer membrane; and PM, periplasmic membrane. Figure (b) reproduced from [91].

Once the probe was calibrated for a given PDMS indentation depth, cyanobacteria filaments were then deposited on a wet glass slide and probed to match the same indentation depth as PDMS, while the cantilever scanned across an area. To ensure that the filaments remained well-hydrated during scanning (and to prevent an artificial increase in E with time, due to drying out [133]), scanning times were kept to less than 5 minutes, and the scanner was covered to minimise airflow. Elastic modulus measurements were extracted by fitting the Derjaguin-Muller-Toporov (DMT) model [117] (see Equation 3.7) to the resulting force-distance curves using the retraction profile, as discussed in 3.1.2. The fitting was done automatically in Bruker's QNM software (Nanoscope Analysis. The result was a map of the DMT modulus of the sample, which was analysed by first selecting an area in the middle of the filament, as shown in Figure 3.10. The statistics for the chosen area are shown on the right hand of Figure 3.10. The mean and the standard deviation of the modulus values were recorded for each filament and the results are to be discussed in section 3.3.2.

3.2.4 Cell wall imaging

To complement my mechanical measurements of cyanobacteria filaments, I observed the internal structure of the filaments using images captured by Transmission Electron Microscopy (TEM). Both sample preparation and imaging were carried out by Dr. Graham Hickman of the Imaging Suite at the School of Science and Technology at Nottingham Trent University while I conducted

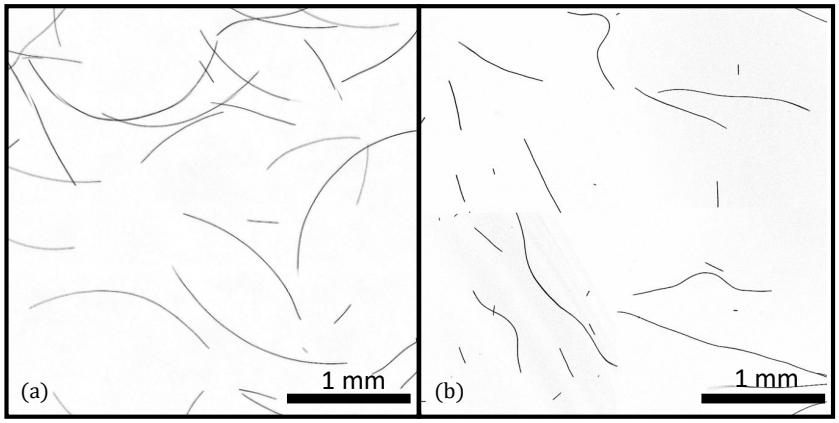

Figure 3.12: Filamentous cyanobacteria under confocal fluorescence imaging. (a) Under ideal conditions active gliding specimens of *O. lutea* appear as long thin curved filaments. (b) When rendered inactive, for example by being briefly cooled, the same filaments adopt a more random shape. Reproduced from [91].

the image analysis and feature measurement. Samples were prepared following methods in Ref. [88], procedure (b). In this instance, the resin was TAAB 813 (TAAB, Aldermaston) and uranyl acetate was substituted for EM Stain 336 (Agar Scientific Ltd., Stansted), which in both cases was used according to the manufacturer's instructions. Once fixed, embedded, sectioned and stained, sections were examined with a JEM2100Plus TEM (JEOL UK, Welwyn Garden City) operating at 120 kV. Electron micrographs were digitised using a Rio16 (Gatan UK, Abingdon) camera operated using Digital Micrograph (3.32.2403.0) and exported to .tiff for analysis. An example of a micrograph collected for one of the species studied is shown in Figure 3.11 and the analysis follows later in section 3.3.2.

3.2.5 Filament shape imaging

Freely gliding cyanobacteria filaments naturally adopt a curved shape, as shown in Figure 3.12(a), whereas inactive filaments have a more irregular, meandering shape, like those shown in Figure 3.12(b). These shapes were quantified by measuring the curvature of over one hundred free-gliding (active) and inactive filaments in each of the three species studied. While the focus here is on the static curvature and how it varies between filaments, in chapter 4 I will present the variation of curvature with time or space, i.e. the dynamic curvature. In the case of active filaments, dilute suspensions ($\sim$ 1 filament/mm^2) were transferred to a well plate (well diameter of 1.5 cm) and then left undisturbed in the incubator for 24 h before measurement.

For inactive filaments, the procedure was similar except that dilute suspension of the filaments

was transferred to a medium with a temperature of 2°C and stored at this temperature for 4 hours. During imaging, ice was added to the suspension to keep the temperature low. After the experiments, the inactivated filaments recovered their motility after warming back up.

Images were taken using a confocal microscope, as described in section 2.2.1, and were processed in Matlab by fitting a circle to the skeleton of the thresholded image of a filament, using Pratt's method [139, 140]. For each filament, the local orientation θ and curvature κ were independently evaluated by fitting tangent vectors to each point along the thresholded image skeleton, using a sampling window of 30 pixels (90 μm). Finally, for each species, the cross-sectional radius of at least 21 filaments was measured by manual measurements of high-magnification optical microscope images (see example in Figure 3.13), using ImageJ [85] and with results shown in Table 3.1.

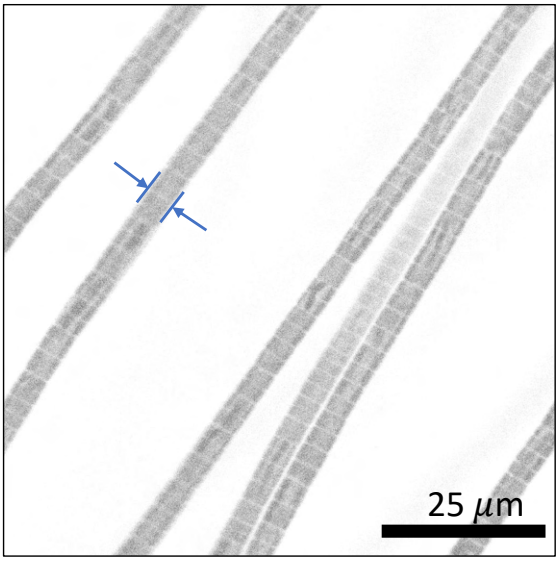

Figure 3.13: Filament widths and structure in *O. lutea*. Under higher magnification, *O. lutea* is seen to be composed of one-cell-wide strands of connected cells. The widths for *O. lutea* were found to be 4.2 ± 0.2 μm and were measured as indicated on the figure. Reproduced from [91].

3.3 Results

The aims of this chapter are to quantify the mechanical properties of typical species of filamentous cyanobacteria and to connect these properties to the shapes they naturally take and the forces that they can generate internally. Here, observations of their bending stiffness β, Young's modulus E, the curvature of active filaments κ and cross-sectional radius r will be reported. A summary of the key results is given in Table 3.1, and tables of all individual measurements are

reported in individual subsections.

Table 3.1: Summary of results, showing the bending stiffness β, the reduced modulus E^* and Young's modulus E of the cell walls, and the average active curvature κ and cross-sectional radius r of the cyanobacteria filaments. In all cases, the uncertainty range gives the standard deviation of the measurements and the number of independent measurements is given by n.

Species	β (N m^2)	E^* (MPa)	E (MPa)	κ (m^{-1})	r (μm)
K. animale	$4.8\pm2.9\times10^{-17}$	53 ± 8	40 ± 6	470 ± 304	2.2 ± 0.1
	n=9	n=13	n=13	n=119	n=29
L. lagerheimii	$6.0\pm5.0\times10^{-17}$	27 ± 6	20 ± 4	452 ± 322	2.2 ± 0.1
	n=9	n=8	n=8	n=98	n=23
O. lutea	$2.6\pm1.6\times10^{-17}$	35 ± 7	26 ± 6	537 ± 228	2.1 ± 0.1
	n=7	n=10	n=10	n=154	n=21

3.3.1 Bending stiffness

The bending responses of the three species of filamentous cyanobacteria were measured using the flow cells described in section 3.2.2 and sketched in Figure 3.8. For each test, the measured displacement profile, $\delta(s) = |\boldsymbol{x}(s) - \boldsymbol{x}_0(s)|$, gives the difference in position between the bent and rest configurations of the filament ($\boldsymbol{x}$ and $\boldsymbol{x}_0$, respectively), from where it enters the flow cell, $s = 0$, to its tip at $s = L$. To retrieve bending stiffness values in any of the experimental runs, the following procedure was followed. First, by combining equations 3.1, 3.4 and 3.5 we have

$$\frac{d^2M}{ds^2} = -\frac{4\pi\mu}{\log(7.4/\mathrm{Re})}u_\mathrm{n}(s). \tag{3.11}$$

For a cantilever beam, as assumed here, and assuming small enough deflections from the rest configuration, Equation 3.11 can be expressed in terms of the deflection profile $\delta(s)$ as

$$\beta\frac{d^4\delta}{ds^4} = -\frac{4\pi\mu}{\log(7.4/\mathrm{Re})}u_\mathrm{n}(s). \tag{3.12}$$

This is a fourth-order beam deflection equation, which is integrated four times numerically in Matlab to obtain an estimate for $\beta\delta(s)$, as explained next. On the right hand of Equation 3.12, I start by evaluating the velocity $u_\mathrm{n}(s)$, using Equation 3.9. From the experiments with confocal microscopy, the vertical position z inside the microfluidic channel was determined by scanning the channel vertically. The width of the channel was 300 μm. Therefore, Equation 3.9 could be evaluated by approximating the series for the appropriate number of terms and grid spacing, as discussed in section 3.2.2.

Now, $u_{\mathrm{n}}(s)$ defines the normal component of the flow velocities along the bent filament. From the experiments, the projection of the bent or deflected filament on the channel width was used to determine the number of flow lines to be considered. The bent filament was first skeletonised and cleaned, such that no two pixels were along the same horizontal coordinate. Due to imaging constraints, the pixel size or the spacing between the points on the filament along the width of the channel was larger than the grid spacing on the flow profile. As such, the flow profile u_y was sampled, such that the spacing between the flow lines matched the pixel size to give a sampled flow profile $u_y(s)$. The points on the bent filament skeleton were used to approximate the angles of the filament with respect to the channel, by fitting a tangent line of angle θ_b to a region of a radius of 11 points at each point along the filament. These angles were then used to calculate $u_{\mathrm{n}}(s)$ as

$$u_{\mathrm{n}}(s) = u_y(s)cos(\theta_b), \tag{3.13}$$

at every pixel along the filament.

The Reynolds number, Re was also calculated for each point along the filament, as $\mathrm{Re} = 2\rho r u_{\mathrm{n}}/\mu$ where ρ, is the density of water, r the filament radius and ν the dynamic viscosity of water at standard temperature and pressure. With u_{n} and Re evaluated, the right-hand side of Equation 3.12 can be computed and the result is a vector containing the list of the forces acting along the filament, at every pixel along its skeleton.

The next step is to integrate Equation 3.12 numerically, four times, to get $\beta\delta(s)$. This is done in Matlab using the function *cumtrapz*(X, Y) which computes the approximate cumulative integral of data Y via the trapezoidal method, with X as the vector of the spacing between points in Y. I, therefore, integrated Equation 3.12 four times over the path length s, applying, in turn, the boundary conditions $\delta'''(L) = \delta''(L) = 0$ (corresponding to a free boundary condition, $M'(L) = M(L) = 0$, at the hanging end of the filament) and $\delta'(0) = \delta(0) = 0$ (corresponding to clamped boundary conditions where the filament enters the flow cell). This leads to a predicted shape of the filament deflection, δ_{p}, up to the (yet undetermined) scale factor β. The next step is to find the deflection of the bent filament.

The deflection profile of the bent filament is found using the shape of the bent filament and the shape of the filament at equilibrium before being exposed to the flow. From the experiments, the equilibrium profile of the filament was measured by converting the filament in a stopped-flow condition into a skeleton and dividing it into the same number of points as the bent filament. In other words, the total path s, from 0 to L, was divided up equally into the same number of points, in each case. By doing so, each point $\boldsymbol{x}_{\mathrm{b}}(s)$ on the bent filament had a corresponding point on the equilibrium shape $\boldsymbol{x}_0(s)$ and these points were used to calculate the deflection profile

as $\delta(s) = |\boldsymbol{x}_\mathrm{b}(s) - \boldsymbol{x}_0(s)|$. To find the best estimate of β I then performed a least-squares fit of the predicted to observed deflection profiles, with β as the free parameter.

So far, this method does not account for any solid-body rotation of the filament, as it responds to the flow. Assuming that all deflections are caused by bending, this gives a lower bound on β. As a refined estimate, I simultaneously allowed for a small rotation, of angle α, around the point where the filament enters the channel. Practically, this was done with the same algorithm as described above, but performing the final fit (now of α and β) against a cost function $(\delta_\mathrm{p}(s) - |\boldsymbol{x}(s) - \mathbf{R}\boldsymbol{x}_0(s)|)^2$, rather than $(\delta_\mathrm{p}(s) - \delta(s))^2$, and where $\mathbf{R}(\alpha)$ is the rotation matrix.

$$\mathbf{R} = \begin{bmatrix} \cos\alpha & -\sin\alpha \\ \sin\alpha & \cos\alpha \end{bmatrix}.$$

The result is the best-fit value of β and rotation angle α. The value of the best rotational angle is then substituted into $|\boldsymbol{x}_\mathrm{b}(s) - R\boldsymbol{x}_0(s)|$ to get the corrected deflection profile, *i.e.* that which now excludes any rotational component of the deflections. An example is shown in Figure 3.14(b). Using the best-fit β, the deflection profiles corresponding to different forces (i.e. flow profiles) can also be plotted. Some examples are shown alongside the corrected deflection profiles in Figure 3.14(b). Alternatively, to get a distribution of the bending stiffness values along any filament, I calculated the bending stiffness for each flow by dividing the output of the fourth-order integral by the corrected measured deflection profiles. This gives bending stiffness measurement at each point along the filament for each flow test. Examples of such bending stiffness profiles are shown in Figure 3.14(c). The bending stiffness profiles were then used to compute standard deviations of β for each flow test, which were used for error propagation.

The final value of β was found in each case by calculating a weighted mean of all the flow tests for a particular filament. This was done by applying the formula

$$\bar{\beta} = \frac{\sum_{i=1}^{n} w_i \beta_i}{\sum_{i=1}^{n} w_i} \tag{3.14}$$

where $w_i = 1/\sigma_i^2$ is weighting for each entry, σ_i^2 is the variance of β_i, while n is the total number of flow tests per filament. The uncertainty in these measurements was taken as the standard deviation of all measurements for a particular filament. The final bending stiffness value for each species was the average of all the weighted mean values in each species with a range of values given by the standard deviation of this distribution. For each species, seven to nine independent strands of cyanobacteria were tested and each strand was subjected to up to six different flow conditions. Results are reported in Table 3.3.1 and Figure 3.14(d). There was considerable variation between individuals, up to about one order of magnitude, but the average bending stiffnesses of all three species were very similar to each other.

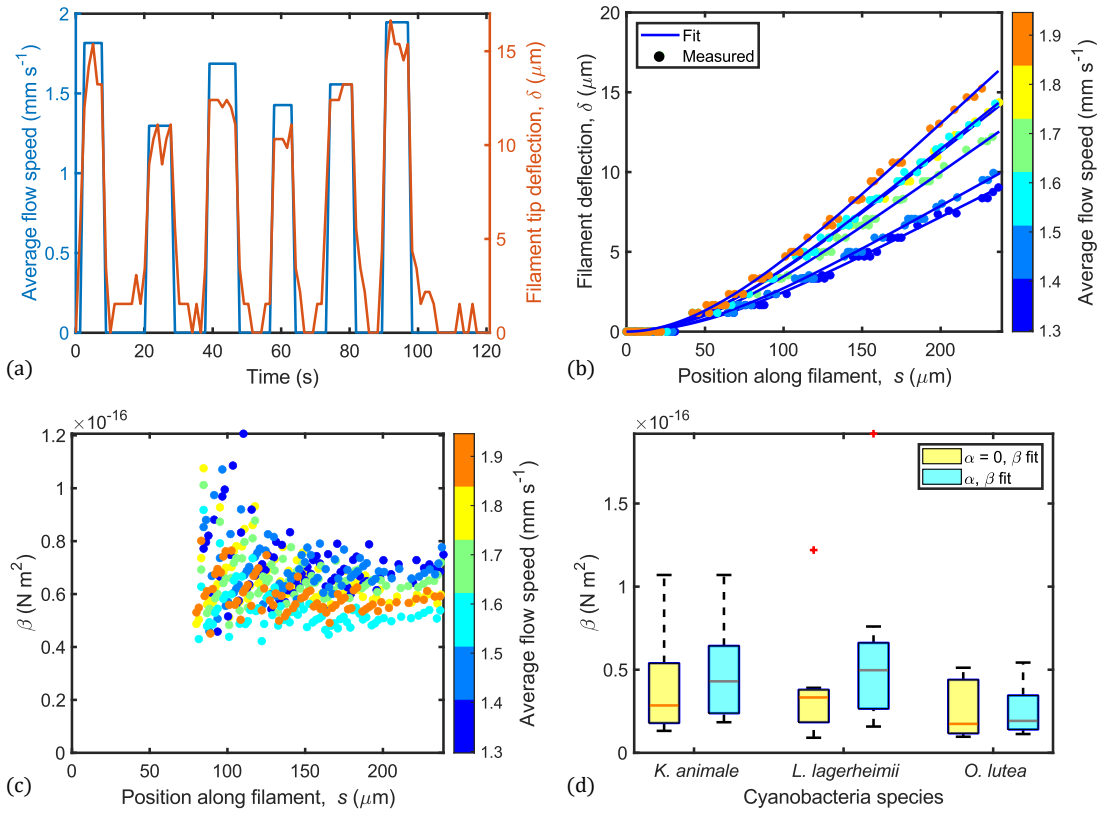

Figure 3.14: Measurements of the bending stiffness of filamentous cyanobacteria. (a) Each flow test consisted of a sequence of different flow speeds, separated by stopped-flow conditions, while I tracked the deflection of a single filament of cyanobacteria in the channel. As shown here, the total deflection was proportional to the applied flow. (b) Each deflection profile was fit to the expected elastic deformation, with the magnitude of the elastic response (effectively, β) and a solid-body rotation, α, as fitting parameters; shown here are the fits for one example filament. (c) After accounting for any rotation through a global correction, a bending stiffness, $\beta(s)$, was then extracted at every point along the filament. (d) I show the distribution of the values of β observed for the three species of filamentous cyanobacteria studied. In each case, results are shown before (yellow, left) and after (blue, right) accounting for rotational effects. On the boxes, whiskers indicate extreme points, a line gives the median and the bottom and top edges of the box indicate the 25$^{\text{th}}$ and 75$^{\text{th}}$ percentile, respectively. Reproduced from [91].

I also include in Figure 3.14(d) the results where rotational effects were neglected (*i.e.* assuming $\alpha = 0$). Since this scenario attributes all motion to bending, these results can be interpreted as a lower bound on the bending stiffness.

The bending results were further analysed to look for evidence of plastic or nonlinear responses. For example, as the cyanobacteria filaments can change their own shape, their response

Table 3.2: Bending stiffness measurements for three filamentous cyanobacteria species. There is considerable variation between measurements within and between species, of up to one order of magnitude.

Species	*K. animale*	*L. lagerheimii*	*O. lutea*
Sample Number	Weighted Mean ± Weighted Error ($\times 10^{-17}$N m^2)	Weighted Mean ± Weighted Error ($\times 10^{-17}$N m^2)	Weighted Mean ± Weighted Error ($\times 10^{-17}$N m^2)
1	2.31 ± 0.72	7.60 ± 1.00	1.92 ± 0.78
2	4.30 ± 1.00	6.28 ± 0.95	3.72 ± 0.75
3	2.41 ± 1.00	4.97 ± 2.25	1.58 ± 0.23
4	6.22 ± 0.65	3.99 ± 1.60	5.43 ± 1.00
5	10.70 ± 2.47	6.16 ± 2.40	1.35 ± 0.36
6	7.05 ± 2.47	19.20 ± 2.74	3.04 ± 0.71
7	5.61 ± 0.95	1.99 ± 1.00	1.13 ± 0.28
8	2.59 ± 2.11	1.58 ± 1.00	
9	1.84 ± 0.70	2.85 ± 0.43	
Mean	4.78	6.07	2.60
SD	2.92	5.33	1.56
SE	0.97	1.78	0.59

to an external flow might relax over time, due to a redistribution of internally generated forces. I tested for this effect in my data by looking for correlations between the measured bending stiffness and the order in which flows were applied. As shown in Figure 3.14(a), each filament was typically subject to six different flow rates applied over a few minutes. Spearman's rank-order correlation test showed no significant correlation between the order in which the flows were applied and the measured β (*K. animale*, $r_s(51) = -0.70, p = 0.23$; *L. lagerheimii*, $r_s(41) = 0.40, p = 0.75$; *O. lutea*, $r_s(36) = 0.26, p = 0.66$). I conclude that, at least over the experimental timescales, there is no evidence of any plastic response to the shear flows.

I also performed statistical tests to check for any systematic effects of the filament length, or flow speed, on the measured bending stiffness. The various cyanobacteria filaments extended lengths L between 190 and 295 μm into the flow cell, but there was no significant correlation between L and β (Pearson correlation coefficient: *K. animale*, $r(51) = 0.07, p = 0.86$; *L. lagerheimii*, $r(41) = 0.17, p = 0.66$; *O. lutea*, $r(36) = 0.65, p = 0.11$). There is, however, a moderate positive correlation between flow speed and β (*K. animale*, $r(51) = 0.47, p < 0.01$; *L. lager-*

heimii, $r(41) = 0.35, p = 0.02$; *O. lutea*, $r(36) = 0.63, p < 0.01$). Although this correlation is not particularly strong, it may indicate a degree of strain stiffening in the filaments, a type of response known from a variety of biopolymers [141], for example.

Furthermore, I note that complementary three-point bending measurements of *O. lutea* and *K. animale* were performed in parallel to this study by a collaborative group under the supervision of Stefan Karpitschka in Göttingen, and are reported in [142]. There was an initial intent for a stronger collaboration here, but the travel restrictions due to covid resulted in these studies proceeding parallel in nature and more independent than planned. While broadly consistent with the results here, they observed higher average bending stiffnesses of $1.4 \pm 0.4 \times 10^{-16}$ N m^2 and $1.1 \pm 0.3 \times 10^{-16}$ N m^2 for *O. lutea* and *K. animale*, respectively. The difference between our results could be due to the assumptions made by our collaborators in their measurement of the bending stiffness. By pushing cyanobacteria filament against two pillars using a calibrated force P from a thin micropipette, they measured the instantaneous deflection d of the filament. The bending stiffness of cyanobacteria filament was retrieved by fitting the equation $B = (\Delta X^3/48)\partial P/\partial d$, where ΔX is the distance between the pillars. In their computation, ΔX was assumed to be constant.

However, as the cyanobacteria filament was being pushed against the two cylindrical pillars as shown in Figure 3.15, the points of contact continuously moved closer, effectively decreasing ΔX. Using the example shown in Figure 3.15, ΔX changed from about 66 μm at no deflection to 53 μm under deflection. Accounting for this change in ΔX reduces the measured bending stiffness values by half, which makes our results more similar.

Finally, recall that in section 3.2.2 I showed that the measured flow inside the microfluidic channel did not fully follow a no-slip boundary condition. However, I decided to use a no-slip boundary condition equation for estimating the flow profiles in my measurements because it was easier to do so than to measure every flow profile. Here, as the last check of the accuracy of my results, I compare the bending stiffness values measured using the no-slip and the observed partial-slip flow profiles along the plane of the filament in the flow channel. Based on the results shown in Figure 3.16, the partial slip-based bending stiffness profile is within 10 % of the no-slip-based bending stiffness profile. Such a difference is largely negligible since the bending stiffness values between filaments vary by one order of magnitude although it may represent a small systematic error of $\leq 10\%$ overestimation, in the results.

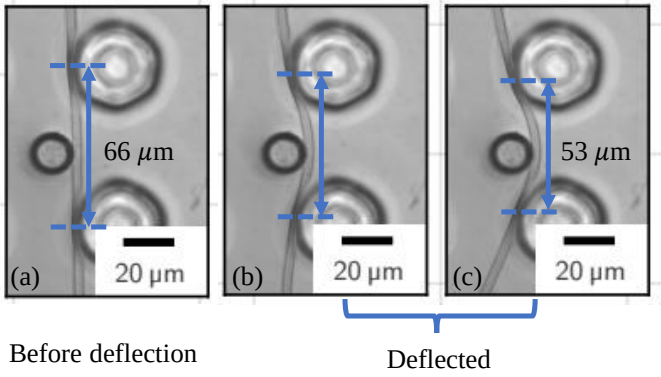

Figure 3.15: Example microfluidic pillars for three-point bending test, as carried out in [142]. (a) Before the force is applied the filament stays straight and the distance between the contact points is roughly equal to the distance between the two pillar centres. (b) When the force is applied the filament bends and the points of contact move closer to each other as is also shown in (c), effectively reducing ΔX used for retrieving the bending stiffness from 66 μm to 53 μm in this case. Adapted from [142].

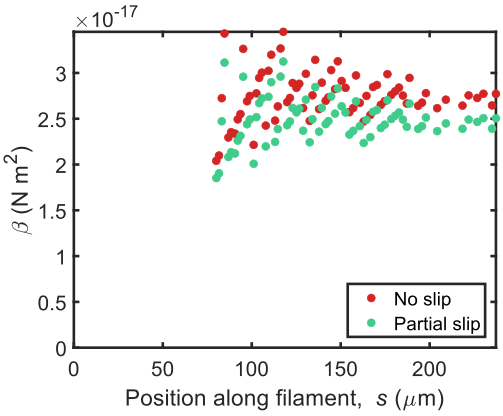

Figure 3.16: Comparison of partial-slip and no-slip flow-induced bending stiffness calculations. Here, the average value for the no-slip profile is 2.75 $\pm$ 0.3 $\times 10^{-17}$ N m^2, while that of the partial-slip profile is 2.49 $\pm$ 0.2 $\times 10^{-17}$ N m^2. These values are within 10 % of one another, much smaller than one order of magnitude variation between measurements shown in Figure 3.14, showing that the no-slip assumption leads to, at most, only a relatively small systematic error.

3.3.2 Nanoindentation and cell wall properties

The bending stiffness of a slender rod, such as a filament of cyanobacteria, is directly related to the elastic properties of its constituents. Assuming that the cytoplasm does not support a significant load, most of the bending moment can be expected to be carried by rigid structures

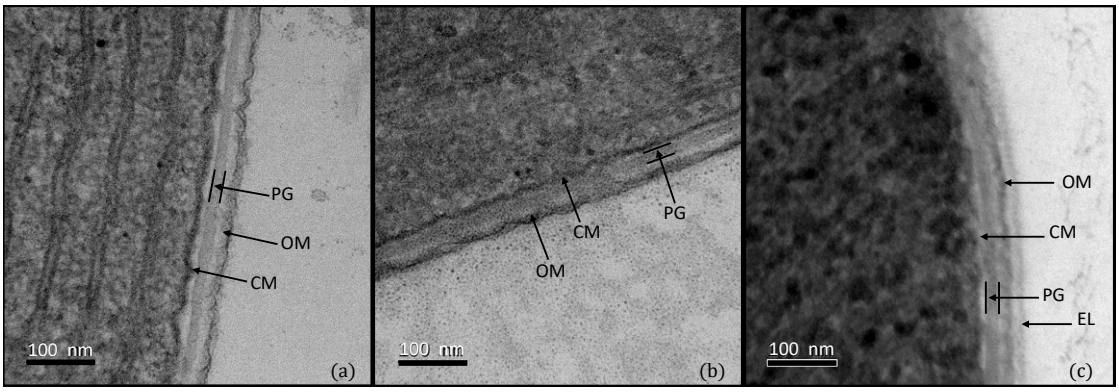

Figure 3.17: Cross-sectional images of filamentous cyanobacteria, taken using transmission electron microscopy. (a) *K. animale*. (b) *L. lagerheimii*. (c) *O. lutea*. Arrows indicate PG, peptidoglycan layer; CM, cytoplasmic membrane; OM, outer membrane; and EL, external layer. Reproduced from [91].

like the cell wall. Here the goal is to test this assumption and evaluate the mechanical properties of the cell walls of my species of filamentous cyanobacteria.

The main structural component of the bacterial cell wall, as reviewed in chapter 1, is peptidoglycan, a stiff cross-linked polymer; this means that the cell wall is known to behave elastically, with measurements of its Young's modulus E typically ranging between about 5-50 MPa [133–138]. Although classed as gram-negative, cyanobacteria have particularly thick cell walls, extending to tens of nanometres or more [143, 144]. Figure 3.17 shows examples of cross-sectional images of the three species of filamentous cyanobacteria under study here.

Maps of the reduced modulus $E^* = E/(1-\nu^2)$ were collected by atomic force microscopy using quantitative nanomechanical mapping techniques, as described in section 3.2.3. For each map, average values and standard deviations were calculated over an area of a cell that avoided any imaging artefacts like scarring and focused on the centre of a filament, to minimise the effects of surface curvature on measurements [132]. The results were converted into measurements of Young's modulus, E, by assuming $\nu = 0.5$, as appropriate for soft biological materials [132, 145]. Measurements from at least 8 different filaments were analysed for each species, at a fixed indentation depth of 50 nm, as shown in Table 3.3.2.

To capture the full distribution of measured values, a box plot of E is given in Figure 3.18(a). All three species have similar Young's moduli, with most observations in the range of 25–50 MPa, although *K. animale* potentially has a slightly higher modulus than the other two species. These results are similar to those found for *E. coli* (35–60 MPa) [133] but noticeably higher than

Table 3.3: Reduced modulus, E^*, measurements for three species of filamentous cyanobacteria, based on AFM force-distance measurements and giving the mean, standard deviation (SD) and the standard error (SE) of all observations.

Species	*K. animale*	*L. lagerheimii*	*O. lutea*
Sample Number	E^* Mean ± SD (MPa)	E^* Mean ± SD (MPa)	E^* Mean ± SD (MPa)
1	38 ± 20	22 ± 16	33 ± 39
2	42 ± 5	31 ± 9	42 ± 24
3	48 ± 4	19 ± 7	35 ± 16
4	47 ± 4	30 ± 10	31 ± 12
5	56 ± 5	24 ± 7	45 ± 24
6	60 ± 19	32 ± 17	27 ± 11
7	54 ± 11	23 ± 8	33 ± 13
8	62 ± 15	34 ± 18	24 ± 8
9	60 ± 14		46 ± 23
10	61 ± 19		32 ± 13
11	60 ± 14		
12	54 ± 18		
13	50 ± 18		
Mean	53	27	35
SD	8	6	7
SE	2	2	2
	E	E	E
Mean	40	20	26
SD	6	4	6
SE	2	2	2

Bacillus subtilis (3 MPa) [146]. To check for any depth-dependence of E, measurements were repeated with indentation depths of 25, 40 and 50 nm. As shown in Figure 3.18(b), there is no clear trend of the measured elastic modulus with indentation depth, supporting the interpretation that the elastic properties of the cell wall were accurately probed.

From the measured Young's moduli, one can also estimate effective cell wall thicknesses, Δr, under the assumption that the majority of the filament stiffness comes from the cell wall. Using Equation 3.6, the estimated wall thicknesses are 35±8 nm, 90±28 nm, and 34±8 nm for

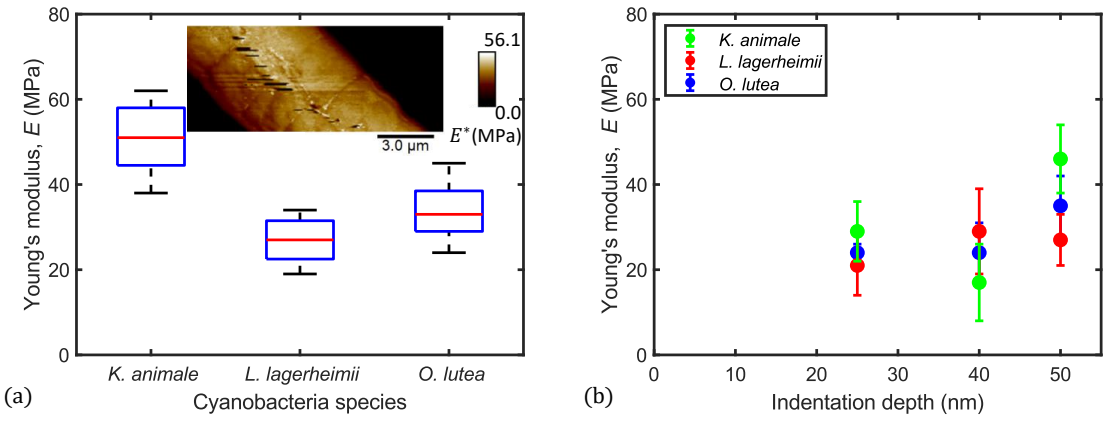

Figure 3.18: Cyanobacteria elasticity was measured by nanoindentation. (a) A summary here shows Young's modulus measurements of the three species of filamentous cyanobacteria, probed to 50 nm depth. On each box, the whiskers indicate extreme points while the red line is the median and the bottom and top edges of the box indicate the 25^{th} and 75^{th} percentiles, respectively. The inset gives an example map of the reduced modulus E^* for *O. lutea*. (b) Repeating the tests for different indentation depths showed no significant effect on the measured E, over the range of depths used. Error bars represent standard deviations of measurements. Reproduced from [91].

K. animale, *L. lagerheimii*, and *O. lutea*, respectively. These estimates can be compared to direct observations of the cell wall structures using TEM, with example micrographs shown in Figure 3.17. At least 5 different filament cross-sectional images were analysed. Thicknesses of different layers of the cell envelope were measured by hand using ImageJ [85]. First, it was noted that the thickness of the full cell envelope is 47 ± 4 nm, 45 ± 3 nm, and 69 ± 6 nm for *K. animale*, *L. lagerheimii* and *O. lutea*, respectively. Similar thicknesses, of 35 ± 5 nm, can be seen for TEM images of *K. animale* in Strunecky *et al.* [88]. These values are comparable to the estimated thicknesses.

However, the cell envelope in cyanobacteria is a layered structure, consisting of a thick peptidoglycan layer separated by inner and outer membranes [144], as shown in Figure 3.17. Of these, the peptidoglycan is expected to be the stiffest layer, and if measured alone has thicknesses of 18 ± 2 nm, 14 ± 2 nm, and 18 ± 3 nm for *K. animale*, *L. lagerheimii* and *O. lutea*, respectively. Thus, while the bending stiffness measurements are largely consistent with the interpretation of the mechanical response of the cyanobacteria as a hollow cylinder, the peptidoglycan layer may need some additional support to fully supply this role. This might come, for example, from the walls between cells, along the length of the filament, which have not been included in this simple

model. Practically, however, these observations show that assuming that the entire cell wall is a uniform load-bearing layer provides a good estimate of the bacteria's mechanical properties.

3.3.3 Filament curvature and shape

Finally, in order to relate the mechanical properties of filamentous cyanobacteria to their shape and ability to generate forces, filaments were observed under optimal conditions (∼20°C) and when chilled to reduce metabolism and mobility (∼2°C). At room temperature, the filaments were active and glided steadily along the bottom of their containers, adopting a curved shape, as shown in Figure 3.12(a). When cooled, the bacteria were inactive and displayed a more irregular, meandering shape, as in Figure 3.12(b).

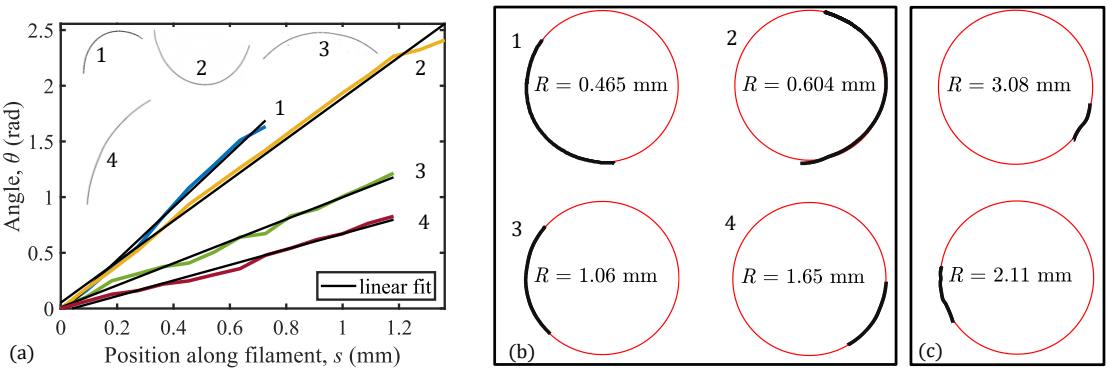

Figure 3.19: Curvature analysis in filamentous cyanobacteria. (a) A plot of the orientation angle *vs.* position along active filaments shows that the filament shape has a constant rate of change of angle, *i.e.* a constant curvature, $\kappa = d\theta/ds$. Shown are four typical cases of *O. lutea*, corresponding to the filaments shown in the upper left. There is a variation of curvature between filaments. (b) Examples of active, gliding filamentous cyanobacteria (black) showing curved configurations along with best-fit circles. (c) Examples of curvature fitting in inactive filaments show that filaments have local shape variations and an overall larger radius of curvature than active filaments. Panels (a,b) reproduced from [91].

In the case of active filaments, their shapes were characterised by looking at how relative orientation θ, taken from tangent vectors, varies along their length s. Each filament was skeletonised and subdivided into subregions of equal lengths of 90 μm (30 pixels). The orientation of the tangent vector to each subregion was then found by fitting a first-order polynomial to the coordinates of all of the pixels in the region and taking the arctangent of the slope. The variation of the angle, along the filament contour, $\theta(s)$, was then measured with reference to the

orientation of the first subregion. Four typical cases of active filaments of *O. lutea* are explored in Figure 3.19(a-b), and the other two species behaved similarly. In Figure 3.19(a) it can be seen that the filaments each have a relatively constant curvature, $\kappa = d\theta/ds$, so that their shapes are well-approximated by circular arcs. One can therefore fit circles directly to the filament shapes, as demonstrated in Figure 3.19(b), to measure their average curvature.

On the other hand, inactive filaments have local shape fluctuations as was shown in Figure 3.12, which affects their overall shape. For comparison with the active filaments, I fitted a circle to the whole shape of each inactive filament as shown in Figure 3.19(c). Curvature distributions were collected from about a hundred individual filaments for each species' active and inactive cases. These measurements are summarised in Figure 3.20. The actively gliding members of all three species have a preferred curvature of around 0.5 mm^{-1}, corresponding to a radius of curvature of about 2 mm. For the inactive filaments, there was no preferred overall curvature, and the measured curvature distributions instead showed a peak, or median value, around zero. It is clear that, for the active case, internal forces within the cyanobacteria filaments break the chiral symmetry, generating the pattern of compression and tension required to maintain a curved shape. Indeed, this bias seems related to their motion, as it was also observed that there is a strong preference for clockwise, over counter-clockwise, motion in all three species (see chapter 4).

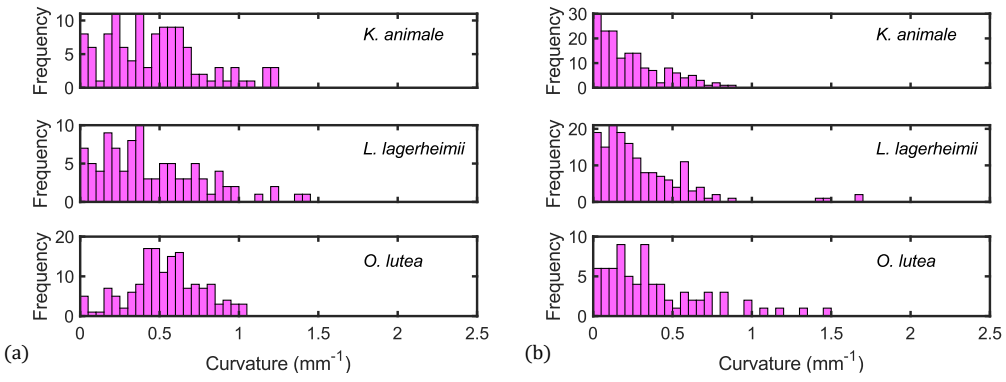

Figure 3.20: Curvature distributions in three species of filamentous cyanobacteria, as measured by fitting the filament shape to a circular arc, as in Figure 3.19, for (a) active gliding filaments at 20°C and (b) inactive filaments at 2°C. Reproduced from [91].

The bending stiffness measurements in this work were made on active filaments under their normal conditions i.e. standard room temperature. While it is understood that inactivity is associated with the loss of smooth filament curvature, there is a knowledge gap on how the same affects the bending stiffness of the filaments.

3.4 Discussion

As outlined in section 1.1, the mechanical origins of the gliding motion of filamentous cyanobacteria have remained obscure, despite several alternative models being proposed [33,34,37,38,41,42]. One factor behind this has been a lack of data about the mechanical response of the bacteria, which can be used to constrain such models. Here, I will briefly discuss how the measurements of the stiffness and other mechanical properties of the cyanobacteria reported here can help understand the forces at play inside a moving chain of cyanobacteria cells. In section 3.3.2 it was seen that the bending stiffness of cyanobacteria can be largely attributed to a rigid cell envelope, and this interpretation will be explored here to consider the magnitude of the internal forces needed to sustain the curved shape of active filaments, along with an estimate of the internal bending energy stored in this curvature. Using a similar energy scale, the disordered shape of inactive bacteria will also be discussed, in the context of a persistence length of a randomly driven flexible rod.

The cyanobacteria studied here move with a slow gliding motion, at speeds of $3.0\pm0.7\mu$m s^{-1}, and slowly rotate as they glide, in a corkscrew-like motion [30, 41, 143, 147]. Their curved shape does not change significantly as they advance, suggesting that the shape is dynamically maintained by something like a compressional wave that accompanies the rotational motion. However, their well-defined curvature largely disappears, on average, when the cells are inactivated by lowering their temperature, further evidencing that their shape results from an internally generated distribution of forces.

In any event, assuming that the filament behaves as a hollow cylinder of radius r and wall thickness Δr, one can estimate the magnitude of the active forces needed to maintain a curvature κ as

$$\sigma_s = \frac{\kappa\beta}{\pi r^2 \Delta r} = \kappa E r. \tag{3.15}$$

This follows from Equation 3.6 and gives the maximum stress that would be felt in a hollow cylindrical beam under uniform bending (see *e.g.* [106, 148]), or alternatively an estimate of the maximum internal stress in the cell wall that would be needed to give rise to the observed curvature. Based on the empirically determined values given in Table 3.1, I can use Equation 3.15 to estimate σ_s in the three species of cyanobacteria studied here. As shown in Table 3.4, these internal stresses are typically of the order of tens of kPa. The energy stored in the bent shape can also be estimated, by Equation 3.3. As shown in Table 3.4, these internal bending energies should reach magnitudes of a few pJ m^{-1}, per unit length along the filament.

Although my focus here has been on the static mechanics of cyanobacteria, these axial stresses can be linked to the various models of gliding motion. As one example, Halfen and Castenholz

Table 3.4: Summary of derived quantities, based on results in Table 3.1. Shown are: the cell wall thickness Δr, estimated from Equation 3.6; the maximum cell wall stress σ_s, from Equation 3.15; and the bending energy per unit length $\mathcal{U}$, from Equation 3.3. In all cases, the uncertainty range gives the standard error of estimates propagated from uncertainties in the quantities in Table 3.1.

Species	Δr (nm)	σ_s (kPa)	$\mathcal{U}$ (J m^{-1})
K. animale	35 ± 8	41 ± 13	$5.2 \pm 1.2 \times 10^{-12}$
L. lagerheimii	90 ± 28	20 ± 9	$6.1 \pm 2.0 \times 10^{-12}$
O. lutea	34 ± 8	29 ± 10	$3.7 \pm 0.9 \times 10^{-12}$

[41, 42] suggested that the fibril layer, which consists of helical structures lying between the peptidoglycan layer and the outer membrane [44], contracts and in the process sends waves in the direction opposite to that of the filament's motion. In the framework of this model, the measurements presented here give the magnitude of the stresses and bending energies that would need to be generated by these contractile waves, allowing more quantitative predictions to be developed for the origins of the gliding motion.

Finally, an alternative characterisation of the shape of filaments is through their persistence length, P, which describes the distance over which correlations in the local filament orientation or direction are lost [149]. This metric has been used to demonstrate that modern cyanobacteria have a similar persistence length to fossil specimens from the Precambrian [87], for example, or to estimate the bending stiffness of microtubules [150]. Mathematically, P can be defined through the relation

$$\langle \cos(\phi) \rangle = e^{-\Delta s / 2P} \tag{3.16}$$

where $\phi = \theta(s + \Delta s) - \theta(s)$ is the change in filament orientation over a distance Δs along its contour length, the factor of 2 in the exponent is appropriate for filaments confined to a surface [150] and the angled brackets represent an average over the contour s and an ensemble of filaments.

Persistence lengths and angular correlations for all three cyanobacteria species studied here were extracted from the skeletonised filament images obtained in section 3.3.3. For the active case of gliding cyanobacteria, as already shown in Figure 3.19, the filaments adopt the shape of a circular arc, rather than a disordered shape. In this case, it is expected that $\phi(\Delta s) = \kappa \Delta s$, instead of following Equation 3.16. Therefore, a correlation analysis of this nature would not be appropriate. In inactive filaments, however, the persistence-length analysis is well-defined, as the filaments are more disordered in their shape. Figure 3.21 shows the persistence length measurements for inactive (non-motile, chilled) filaments, which are all in the range of 5–10 mm.

This is of a similar magnitude, although slightly larger than, the values of 1.3–3.9 mm previously measured for P in other species of *Oscillatoria* [87].

Interestingly, these shape fluctuations can also be linked to an energy density along the length of the filaments. For thermally driven systems of slender filaments, such as microtubules, $P = \beta/k_BT$, where k_B is Boltzmann's constant, and T the system temperature [87, 149, 150]. Cyanobacteria are too large to be in this limit–the persistence lengths based on the thermal energy k_BT and the measurements of β in this chapter would be several kilometres. However, an analogous relationship may still hold, if the shape is determined by some actively generated but incoherent distribution of forces. In this case, one would anticipate stored strain energy along a segment of length P to be of order β/P, or that the total strain energy density in the filament is $U \simeq \beta/P^2$. Given measurements of β and P presented here, this is about 1 pJ m^{-1} for all three species studied here, which is surprisingly similar to the bending energies of the gliding, uniformly curved specimens. Alternatively, this means that, on average, the magnitude of the locally-defined curvature $|d\theta/ds|$ is similar in both cases. A plausible interpretation of this is that, when the filaments are not moving, the cells maintain some degree of the internal stresses that would otherwise be coordinated into *e.g.* a contractile wave, but these forces are instead uncoordinated.

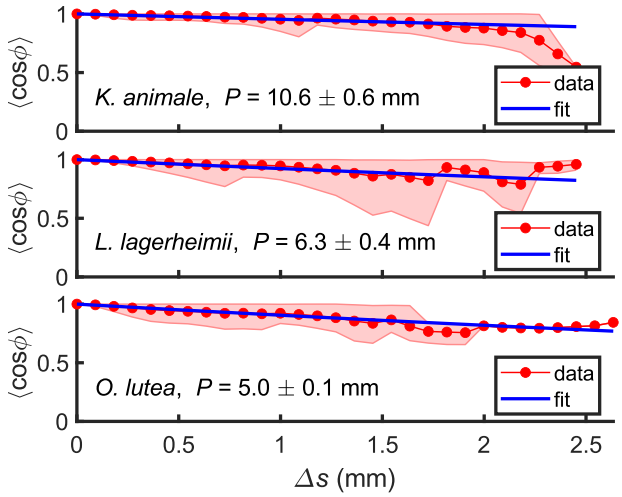

Figure 3.21: Measured persistence length in inactive filaments of *K. animale*, *L. lagerheimii* and *O. lutea*, evaluated by analysing 164, 162 and 79 filaments for each species, respectively. Fits for the persistence length use Equation 3.16. The shaded region represents extreme points of the distributions (using shadedErrorBar function [127]). Reproduced from [91]

3.5 Conclusions

In this chapter the mechanical properties of three related species of filamentous cyanobacteria, namely *K. animale*, *L. lagerheimii*, and *O. lutea* have been quantified. These species all belong to the order *Oscillatoriales* and are of similar size and motile behaviour. This allows for robust validation of the internal consistency of the methods employed in this chapter. In later chapters, the study will focus on single-species observations, but the results here suggest that the subsequent measurements will be similarly general in nature. As a further consistency check, the measurements presented in this chapter can be compared with contemporaneous observations using three-point bending tests from a collaborating lab [142] at the Max Planck Institute for Dynamics and Self-organisation (MIPDS) in Göttingen. The collaborating lab used a thin micropipette to bend a cyanobacteria filament against two pillars. With a calibrated force, and observing deflections of the filament, they were able to measure the bending stiffness of two out of the three species studied in this project. Both labs found consistent measurements, although the other lab's measurements were higher on average than mine. Taking into account the moving points of contact between the filament and pillars may partially explain the difference between the results reported there, and those in this work. Apart from measuring the bending stiffness, the collaborating lab also estimated the forces involved in the self-buckling of the filaments [142].

The observations in this chapter focused on quantifying and understanding the source of the bending stiffness or flexural rigidity in filamentous cyanobacteria, as well as looking at their implications on the shape and motion of these organisms. It was found that the mechanical responses of all three species were similar to each other. Indeed, for many measurements, there was just as much variation between filaments of the same species as there was between species. The average bending stiffness ranged between 2.6-6.0$\times 10^{-17}$ N m^2, as measured by monitoring the bending of filaments under flow in a custom-built microfluidic flow cell. These observations were complemented by measurements of the elastic modulus of the cell wall, through AFM techniques, and measurements of the thickness of the cell wall and its component layers, through TEM. By comparing the bending stiffness to that expected from a hollow rigid cylinder, it was shown that the resistance of filamentous cyanobacteria to bending is largely due to the mechanical stiffness of their characteristically thick cell walls.

To link the bending stiffness to the shape and motion of the cyanobacteria, I performed a characterisation of the shapes of filaments when they were actively gliding at room temperature, and when their motion was halted by reducing the temperature of their environment. While active, isolated filaments adopted a uniformly curved shape, like circular arcs. The curvature distributions were shifted noticeably away from zero, with mean curvatures of about 0.5 mm^{-1}

in all cases. This bias seems to be connected to their motion, which shows a strong preference for clockwise over counter-clockwise rotation, as the filaments glide. A more detailed study of the dynamics of filament motion will follow shortly in chapter 4.

Finally, exploring these results in line with one of the theories of gliding motion, which suggests that shape fluctuations or internally generated waves drive filaments in a gliding motion, the bending energy and maximum axial stress in the cell walls of the filaments were estimated. The results in this chapter show that activity in filamentous cyanobacteria can induce axial stresses of up to tens of kPa in the cell wall. These results are applicable to the wide range of areas where mechanical properties of filamentous cyanobacteria are needed, such as modelling biofilm self-organisation [47] and in the design of scaffolds for microbial fuel cells bio-reactors [96, 97].

Chapter 4

Dynamic properties of single cyanobacteria filaments

4.1 Introduction

Motility in filamentous cyanobacteria is still one of the unresolved mysteries of locomotion in microorganisms [39, 151]. Motile filamentous cyanobacteria are known to move by gliding [30], a type of locomotion whereby filaments move along surfaces without the aid of any physical appendages like cilia or flagella. This type of locomotion has been investigated for some time but the story is still incomplete, with different theories proposed to describe the mechanisms behind gliding motion in filamentous cyanobacteria, as described in section 1.1. For example, one theory suggests that gliding motion is mediated by the continuous secretion of polysaccharides through pores on individual cells [33–35], while another theory suggests that gliding motion involves the use of type IV pili [37–39] which are short, hair-like appendages found the surface of many bacteria and archaea [152–154]. There are five classes of pili, based on protein structure, [155] including chaperone–usher pili, type IV pili, type IV secretion pili, type V pili, and curli fibres. The type IV pili class is widely known for its role in bacteria motility, especially twitching behaviour in *E. coli* [156, 157]. Other scholars have suggested that surface waves generated by the contraction of a fibril layer in the cyanobacteria cell wall act as the mechanism behind the gliding motion in cyanobacteria [41, 42]. This fibril layer has been found to have helical structures and is thought to influence corkscrew-like motion, as these filaments are seen to rotate as they glide on substrates [44]. Figure 4.1 shows a helical fibril layer in *Oscillatoria sp.*

Cyanobacteria rely on light to power their bodies through photosynthesis. To optimally utilise light energy in their environment, cyanobacteria developed mechanisms to move towards or away from light sources, commonly referred to as phototaxis [158]. As will be demonstrated in this chapter, cyanobacteria locomotion, especially their tendency to reverse their motion, is affected by light gradients. In chapter 3, it was shown that single active isolated filaments take on the shapes of circular arcs. As shown later in this chapter, the curvature of single filaments varies

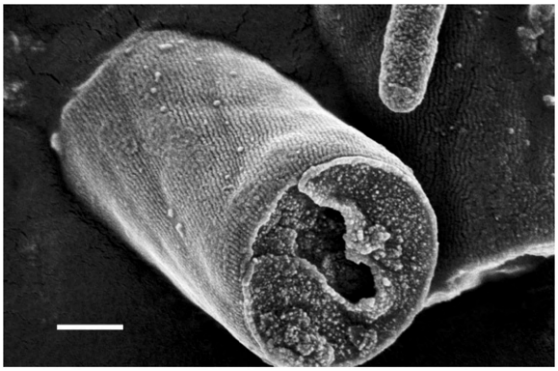

Figure 4.1: Electron micrograph of a fragmented single cell of *Oscillatoria sp.* filament showing the fibril layer as parallel corrugations on the cell surface, running at an angle to the long filament axis. The contraction of such grooves is thought to induce gliding motion and rotation of filaments along their main axis. Figure adapted from [44]. Scale bar: 500 nm.

around a non-zero mean value.

In this chapter, I will investigate the motion and shape dynamics of single cyanobacteria filaments. The presentation here is a continuation from chapter 3, but now with a focus on the dynamical properties of single filaments instead of the static ones. In line with the main goal of the thesis, this chapter identifies the key features of cyanobacteria filament motion, which are intended to guide the development of a numerical model for the self-organisation of filamentous cyanobacteria, a complementary work being carried out by collaborators (Dr. Marco G. Mazza and Jan Cammann) at the University of Loughborough, UK. The findings in this chapter will be applied in chapter 6, for example, where the key behavioural features of cyanobacteria filaments are used to describe collective self-organisation. While this chapter does not directly resolve the mysteries around locomotion in filamentous cyanobacteria, the details presented will support some of the existing theories of gliding motion, thereby opening doors for further studies.

Here, I also focus on one particular species, *Oscillatoria lutea*, allowing for a more detailed and rigorous study of its dynamics. Specific questions to be answered in this chapter are: How does an isolated filament of filamentous cyanobacteria move? How does the shape of the filaments vary with time and space? And, how often do filaments reverse their motion? These questions will be answered by monitoring the motion of single isolated filaments over a period of time, and the information sought will be found by analysing the behaviour of the filaments, as is described in the next section. Results from this chapter have been published [159].

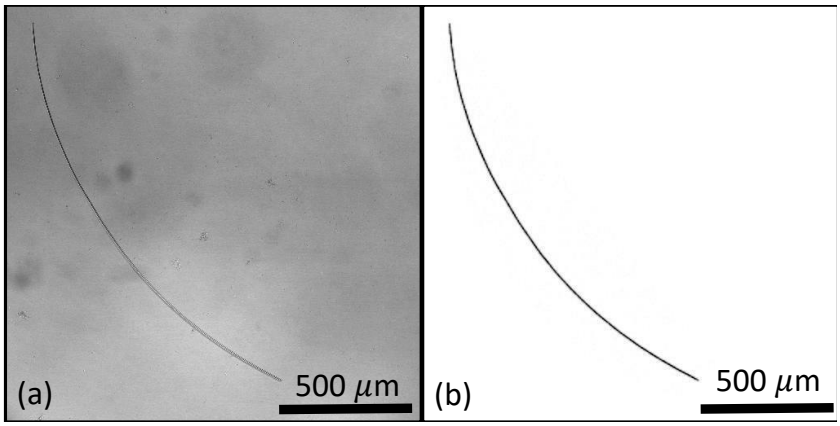

Figure 4.2: Example images of single filaments of cyanobacteria (*O. lutea*). (a) A bright field image, and (b) an inverted confocal image of the same filament.

4.2 Methodology

The behaviour of isolated filaments was studied by observing single filaments gliding on a flat substrate with no interactions with walls or other filaments. For this, a dilute suspension of filaments of *O. lutea* was first transferred into a six-well plate dish whose wells had a diameter of 3.4 cm, with a filament density of approximately 1 filament per mm^2 or less. Once transferred, filaments were allowed to stay for 24 hours in an incubator with controlled lighting and temperature, as described in section 2.3. After 24 hours, filaments were moved into an imaging suite and tracked by taking bright-field and fluorescence images of each filament using a confocal laser microscope, as described in section 2.2.1, for periods ranging between 20 minutes and 3 hours. Example images are shown in Figure 4.2.

The fluorescence images had a very high signal-to-noise ratio, which is a good condition for thresholding. On the other hand, the bright-field images were used to confirm that the filament was well away from non-fluorescent objects, such as walls. The aim was to study the filament while it was not being disturbed by external factors. As such, once the filament was in contact with any wall or other filament, tracking of the filament was aborted. Images were taken at temporal and spatial resolutions of 1.29 seconds and 3 μm, respectively. The maximum width for a single captured image was 1.55 mm, and only filaments with lengths less than the image width were tracked.

Tracking a filament was achieved by moving the X-Y stage of the confocal laser microscope to ensure that the whole filament was inside the field of view. The X-Y stage could only be moved while data capture was stopped. As such, data for each filament consisted of streams of images for each fixed X-Y position of the sample stage, separated by brief breaks in the data

as the microscope stage was moved. For each fixed position, the confocal microscope software (LAS AF) provided the X-Y coordinates of the microscope stage, as well the start and end times of capture of the stream of images. This information was used to stitch all the images taken at different X-Y positions into one series of images with consolidated X-Y positions and times as demonstrated in Figure 4.3. The stitching process started with finding the extreme values of the stage coordinates, [X_{min}, X_{max}] and [Y_{min}, Y_{max}], from the coordinates of all the imaging points. These extreme coordinates were used to construct a larger image (large red box in Figure 4.3) into which all the individual images were copied, according to their respective coordinates, as demonstrated in Figure 4.3. The result was a series of images, each showing the filament position in the consolidated image. The times for the images were also consolidated, such that the first image was assigned a time of zero seconds based on the timestamps provided by the confocal software.

The stitched series of images, therefore, had small gaps in time (15 to 30 seconds) accounting for the time required to move the stage and restart image acquisition. For quantities such as speed or angular drift, the gaps did not have any significant effect, since the changes in distance and angle were mostly linear with time. However, quantities that needed continuous data, such as the rotation frequency of the filament, were quantified using portions of the series of images that had no temporal gaps. Also, I noticed a negligible position hysteresis error of ~ 3 μm, which might have been caused by magnetic hysteresis and/or mechanical friction in the microscope stage stepper motor [160].

The consolidated series of images were processed in Matlab, where each image was converted to binary using the *imbinarize(I, T)* function, where I is the image and T is the threshold value, here 0.25. This leaves the bright cyanobacteria highlighted as white pixels on a black background on a black-and-white image,BW. Recall that images presented here are mostly inverted, for easier viewing. Any smaller bits of cyanobacteria or fluorescent material that were not part of the filament under study were removed from the image by applying the *bwareaopen(BW, P)* function, and setting the area of objects to be removed P to be less than the area covered by the filament of interest. The *bwareaopen* function calculates the area of groups of joined or connected white pixels. All groups, also known as objects, with pixel areas less than or equal to the area P size are removed from the image, by setting the pixel values to zero. Again, mostly the filament of interest was the only visible object in the image space, and this was achieved by using a very dilute suspension of filaments. The binary image was then skeletonised using the *bwmorph* function and the operation *skel*, applying it repeatedly until the filament was just a single pixel wide, producing a skeleton of the original shape.

The endpoints of the filament were identified using the same *bwmorph* function and the

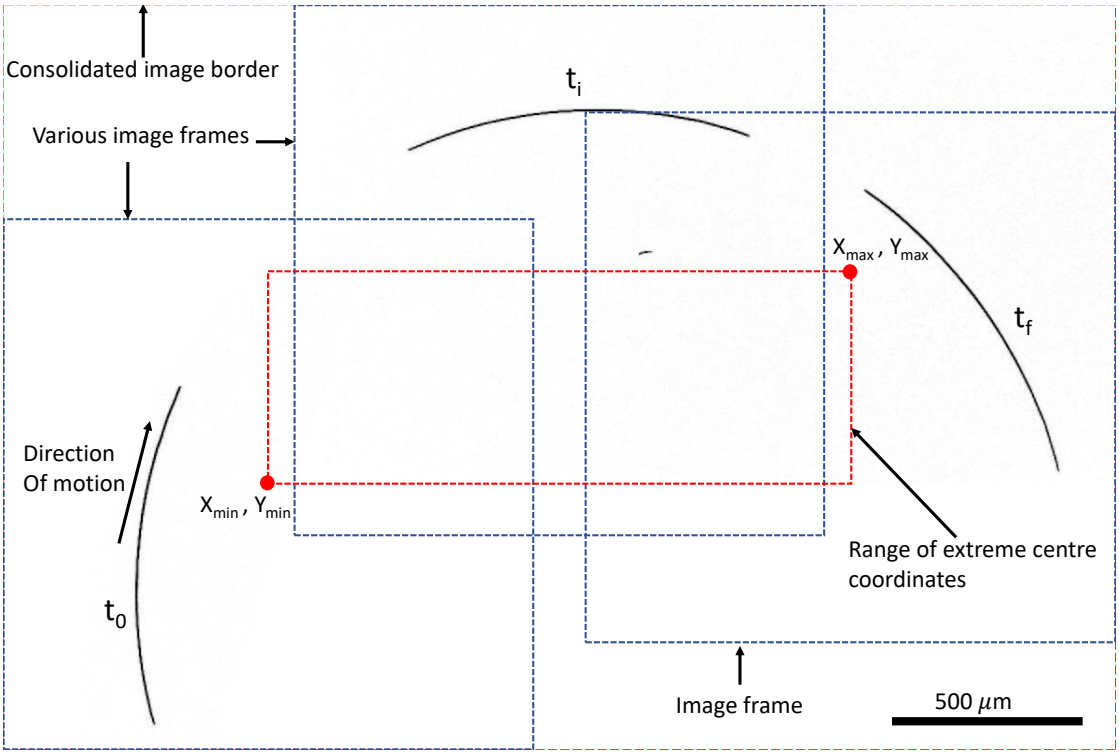

Figure 4.3: Example image stitching process. First, extreme coordinate values (from the image centres) were found from the coordinates of all the images and these were used to construct a consolidated frame of reference for the images (small red box). The size of the consolidated image (large red box) was found by extending the border of this box by half the captured image width. Later, each image was copied into this template according to its X-Y coordinates, to generate a consolidated time series of images. Here, I show a superposition of three images, showing the positions of the filament at the start of image acquisition t_0, an intermediate stage t_i and the final image t_f.

operation *endpoints*. The midpoint of the filament was identified as the point on the filament with an equal contour length to either endpoint along the filament skeleton. The coordinates of the two endpoints and the midpoint were all tracked for the entire series of images collected. The filament shape or the skeleton was also divided into three portions: the middle part and two tails, for further analysis, as demonstrated in Figure 4.4(b). The middle part of the filament was taken as half the length of the filament and was centred at the midpoint. The average orientation of the filament was based on the orientation of this middle part of the filament. The two tips were each defined as a quarter of the length of the filament, as measured from the endpoints. These tips were used to quantify the angular drift or the rotation behaviour of the cyanobacteria. The

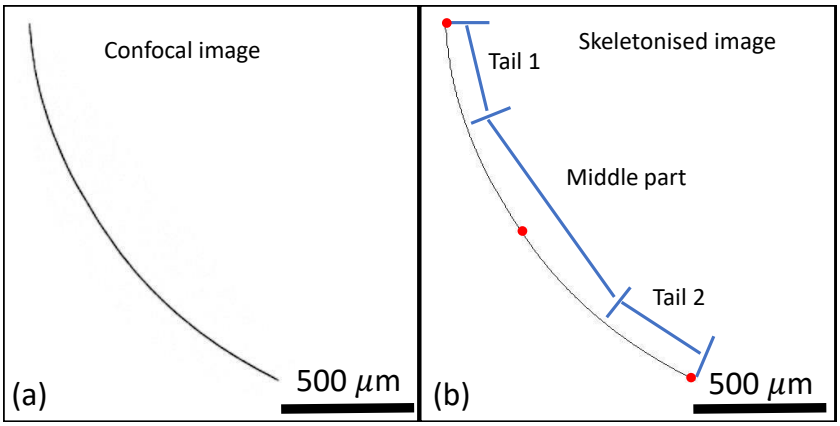

Figure 4.4: Image processing for single filaments. (a) Inverted confocal image of a filament, and (b) a binary skeleton of the confocal image showing the endpoints and the midpoint of the filament (red dots), and the segments used to quantify the tip and overall filament dynamics.

coordinates of the whole filament skeleton were also stored for each frame for further analysis, including measuring filament curvature, as described in the next section. Finally, for purposes of visualisation, images could be inverted to show black filaments on a white background, as shown in Figure 4.4.

4.3 Results

Having turned each series of images into skeletons where the endpoints and the midpoint are marked, I used the resulting images to quantify the behaviour of each filament by tracking the filament trajectories. In particular, I measured parameters such as speed, angular drift, and reversal rates of the filaments. In the next subsections, I will present these measured filament behaviours in detail.

4.3.1 Isolated filaments move in circular clockwise motion

It was observed that isolated cyanobacteria filaments moved consistently in a nearly circular motion, with a preference for clockwise over counter-clockwise motion. Similar motions have been observed previously in *Phormidium* species [30, 143], while the counter-clockwise motion was observed in *Oscillatoria princeps* and *Lyngbya aeruginosa* [30,143]. Indeed, this observation is thought to be influenced by the presence of helical structures on the fibril layer of *Oscillatoria*, as observed in Ref. [44, 161], which would the chiral break symmetry as the filament rotates in a corkscrew motion, as also observed in this project. Figure 4.5 shows an example of a track made

by one *O. lutea* filament. This type of behaviour was consistent across all observations made in this project, including all 23 tracked filaments. In the next sections, I will demonstrate the quantitative analysis of the behaviour of these filaments, using the track shown in Figure 4.5, and then give a summary of the results from all 23 filaments observed.

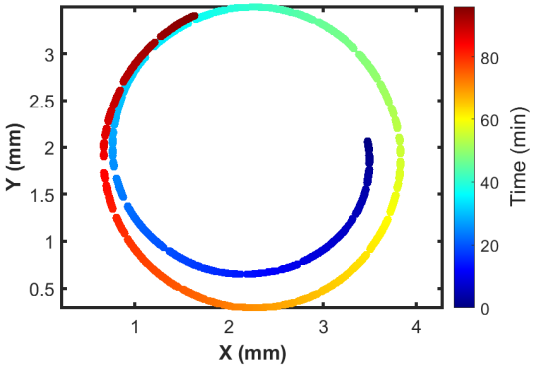

Figure 4.5: Cyanobacteria filament midpoint track, showing that the motion is clockwise and nearly circular. This behaviour was consistent in all the observed isolated filaments. Adapted from [159].

4.3.2 Gliding speed is roughly constant

The gliding speed of the filaments was quantified by tracking the midpoint of each filament, both in time and space. The midpoint of the filament was defined as a point that was equidistant from both ends of the filament along the filament contour. The total distance travelled was calculated cumulatively, as shown in Figure 4.6(a). The overall shape of the cumulative distance profile is roughly linear with time, as demonstrated by the linear fit in Figure 4.6(a). This suggests that the gliding speed in *O. lutea* is constant over long times. This outcome of a roughly constant gliding speed was consistent across all the observed filaments.

As an additional check, I looked at whether filament speed was dependent on filament length. The lengths of the filament studied varied between 0.5 and 1.5 mm. It was found that there was no significant correlation between speed and filament length in this range (Pearson correlation: $r(23) = 0.37, p = 0.08$). A plot of the measured speeds against filament lengths is shown in Figure 4.7.

However, a closer look at the cumulative distance profile shows that there are local periodic variations, demonstrated by the meandering shape of the plot in Figure 4.6(a). This suggests that filaments accelerate and decelerate periodically, around their average speed. To capture

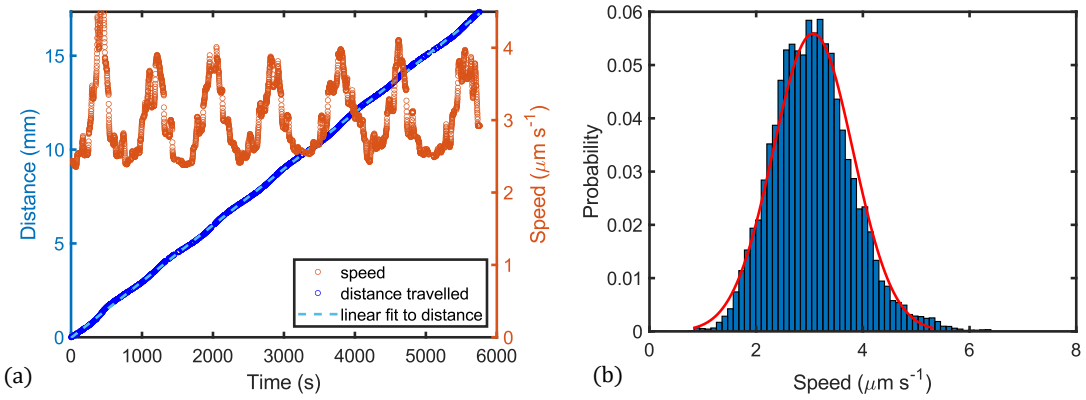

Figure 4.6: Cyanobacteria filament speed as measured by tracking the midpoint of a filament. (a) Cumulative distance is roughly linear and filament speed, calculated by finding the instantaneous slope of the cumulative distance profile, is roughly constant but shows periodic variations, as highlighted when the instantaneous speed is plotted (right axis). The cumulative distance was measured by tracking the midpoint of the filament. (b) A distribution of an ensemble of instantaneous speed measurements from 23 filaments of speed measurements is shown. The average speed from all the measurements was 3.01 $\pm$ 0.70 μm s^{-1} (mean $\pm$ standard deviation). Adapted from [159].

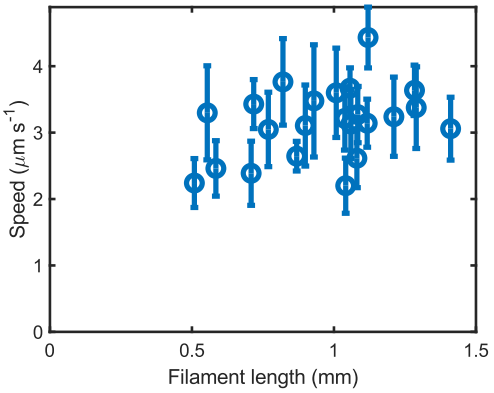

Figure 4.7: Filament speed vs filament length. The distribution of the data points shows a moderate positive correlation, but it is not significant (Pearson correlation: $r(23) = 0.37, p = 0.08$). The bars on the data points represent the standard deviation of each measurement.

these oscillations in speed, I computed the instantaneous slope of the cumulative distance profile shown in Figure 4.6(a), using a sliding window of 40 data points, which was equivalent to a period

of about 52 seconds. The computed speed profile is also shown in Figure 4.6(a), which clearly shows the periodic pattern of the gliding speed. The procedure was repeated in all 23 observed filaments and the distribution of the instantaneous speeds from all the filaments is shown in Figure 4.6(b). The average speed from this ensemble was found to be 3.01 ± 0.70 μm s^{-1} (mean ± SD). The measured speed is similar to that observed in *Oscillatoria sp.* (3-4 μm s^{-1}) [162] but higher than that observed in *Pseudanabaena* (1.3 μm s^{-1}) [45]. However, to my knowledge, there has never been a record of the periodic behaviour observed here in other observations of filamentous cyanobacteria.

Going back to the computation of the instantaneous speed, the choice of the sliding window size was based on testing different sizes and then choosing a window size with the smoothest profile while confirming that the results were robust and consistent for a range of window sizes. The tests were conducted by trying to increase window sizes of 6, 10, 20, 30 and 40 points. As can be seen from Figure 4.8, all the window sizes captured the periodic pattern of the gliding speed of the filament around the same average. As expected, the wider the window, the lower the noise in the computed profile, as shown in Figure 4.8, although the computed profile does not improve much between the window sizes of 20 and 40 points. I, therefore, chose a sliding window size of 40 points for computing instantaneous gliding speeds.

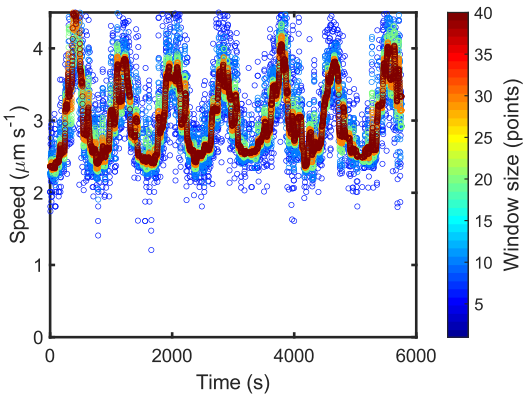

Figure 4.8: Effect of sliding window size on the computed speed. The computed profile becomes smoother with increasing window size. A window size of 40 points was used for the computations made in the rest of this chapter. Each point or step corresponded to a time of 1.2 seconds.

The gliding speed could also be calculated by tracking the translation of the endpoints of the filament. However, as shown in Figure 4.9, filaments wiggle their ends as they glide and rotate in a corkscrew fashion. The wiggling behaviour forces the cumulative distance moved by an endpoint to be greater than the actual translation of the filament. Consequently, if the

speed was to be quantified based on the translation of the endpoints, then the values would be higher on average, compared with the average speed of the midpoint of the filament. Figure 4.10 demonstrates this, where is shown that the profiles of speed based on the movement of either endpoint of the filament are higher than the speed profile measured by tracking the midpoint of the filament.

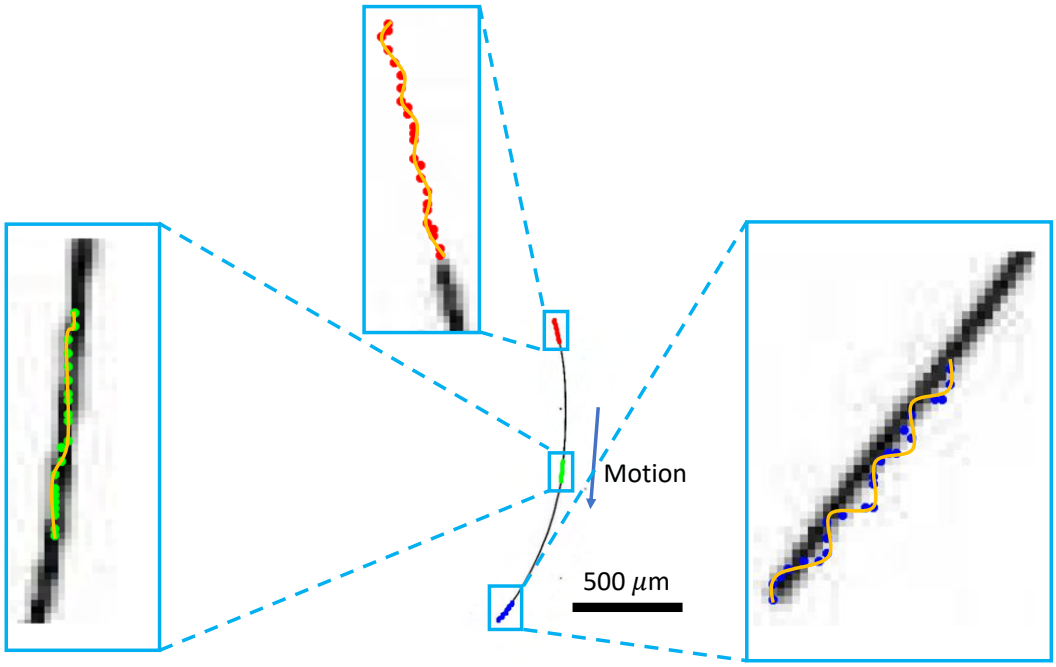

Figure 4.9: Filamentous cyanobacteria rotate as they glide in a corkscrew-like motion. Rotations are most visible at the endpoints, which are seen to oscillate as shown by the closeup views of the traces left by the filament endpoints. The trace by the midpoint of the filament is smoother and does not show oscillations. The yellow lines are drawn to highlight the path taken by the points traced. The leading end usually oscillates with larger amplitudes than the trailing end.

Another analysis made was to determine the frequency of the oscillations in speed. The oscillations in speed, as shown in Figure 4.11(a), have a period of about 900 seconds. To determine the dominant frequency of the oscillations I used Fourier analysis, specifically by computing the Fourier transform of the speed profile. Before computing the Fourier transform, the time series was flattened by detrending the data, subtracting a best-fit linear profile. The original and detrended data are shown in Figure 4.11(a). The Fourier transform of the flattened signal $F(\omega)$ was then computed in Matlab using the function *fft* and the power spectrum computed as $|F(\omega)|^2$. The dominant frequency for the example shown in Figure 4.11 was 0.0012 Hz (corresponding to a period of about 13.9 minutes) at a frequency resolution of 0.00017 Hz. In general, the period of

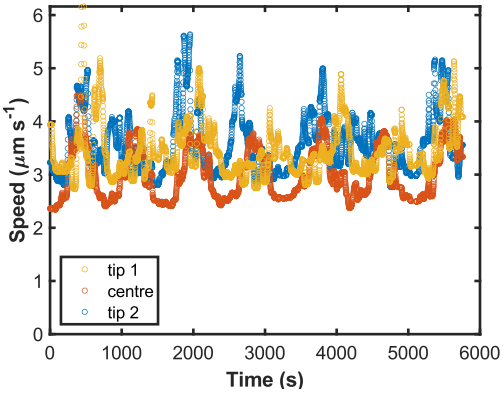

Figure 4.10: Comparing cyanobacteria filament speed measurement approaches. Speed measured by tracking the endpoint (tip) of the filament is higher than that measured by tracking the midpoint (centre) of the filament. This is due to the wiggling behaviour of the endpoints of the filament. Cyanobacteria speed was therefore measured by tracking the midpoint of the filament.

oscillation in speed ranged between 5 and 55 minutes, with the majority between 5 and 24 minutes (15 ± 11 minutes, mean $\pm$ SD), as shown by an insert in Figure 4.11(b). To my knowledge, there are no known processes in cyanobacteria that have similar time scales or that these variations can be attributed to. By comparing the observed periods of speed oscillation with other characteristic time scales of filament behaviour, I note that the time taken to complete an average filament length of 1.5 ± 1 mm is 8 ± 6 minutes, which overlaps with the observed periods of oscillation in speed (15 ± 11 minutes). However, the time a filament takes to complete a circle is longer than the observed periods of oscillation in speed. Based on the filament curvature of 537 ± 228 m^{-1} as reported in Table 3.1, active *O. lutea* filaments complete a circle in 65 ± 28 minutes, on average, longer than 15 ± 11 minutes of oscillation period in speed observed.

4.3.3 Angular drift is roughly constant

The behaviour of isolated filaments moving persistently in a clockwise motion means that any filament changes its orientation with time. The variation of the filament orientation with time or distance travelled is what I call angular drift. In this section, the angular drift was calculated in the same manner as the speed of the filament in section 4.3.2, *i.e.* by using a sliding window of 40 points. In section 4.2 it was stated that each filament was divided into three portions: two tails and the middle part, as illustrated in Figure 4.4. The orientation of each portion, the angle θ, was measured by fitting a straight line to the coordinates of each portion and then calculating the arctangent of the slope. The final list of angles was expressed with reference to

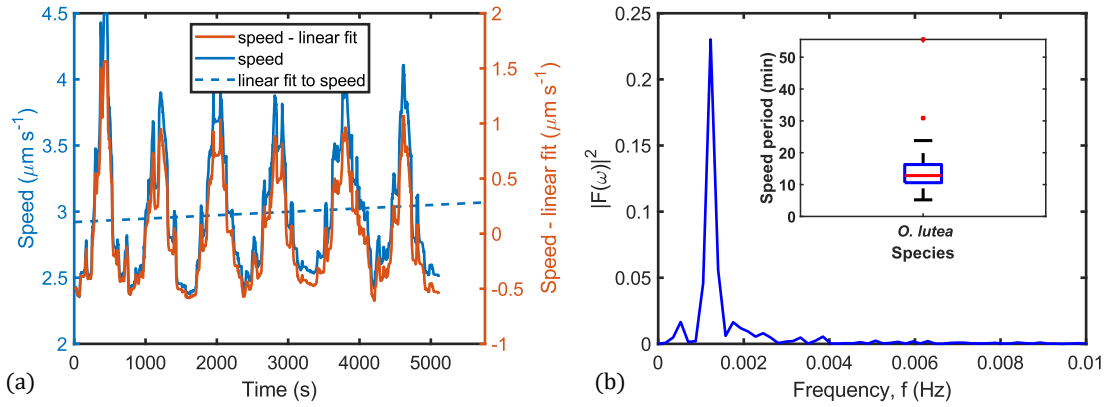

Figure 4.11: Analysis of filament speed periodic behaviour in *O. lutea*. (a) The filament speed profile was flattened before frequency analysis by subtracting its mean, which here was found by fitting a straight line. (b) The flattened profile was analysed by computing its Fourier transform using the *fft* function in Matlab. The dominant frequency for this signal, i.e. the peak, is 0.0012 Hz, corresponding to a period of about 13.9 minutes. The insert shows a summary of the measured periods of speed oscillation the majority of the measurements fell between 5 and 24 minutes. On the box, whiskers indicate extreme points, a line gives the median, and the bottom and top edges of the box indicate the 25$^{\text{th}}$ and 75$^{\text{th}}$ percentile, respectively.

the initial orientation, where a decreasing series meant that the filament was rotating clockwise while increasing angles represented a counter-clockwise rotation. Angles for the two tails and the middle part of the filament were all recorded. In this section, I only used the orientation of the middle part of the filament, which represented the average orientation of the filament at a particular time. The angular variation of the filament with respect to time, $\mathrm{d}\theta/\mathrm{d}t$, is periodic as shown Figure 4.12(a) and in agreement with the periodic behaviour of the speed, as seen in section 4.3.2.

One can reconcile these observations of periodic behaviour by instead considering the angular drift with respect to distance travelled, $\mathrm{d}\theta/\mathrm{d}s$. As shown in Figure 4.12(b), this metric does not show a periodic pattern, demonstrating that the periodic pattern observed in $\mathrm{d}\theta/\mathrm{d}t$ originates from the velocity variation since $\mathrm{d}\theta/\mathrm{d}t = \mathrm{d}\theta/\mathrm{d}s \cdot \mathrm{d}s/\mathrm{d}t = \kappa v$. Here, it can be further shown that angular drift with respect to time, $\mathrm{d}\theta/\mathrm{d}t$ is comparable to the product of the mean filament curvature measured in chapter 3 and the mean velocity measured in this chapter *i.e.* $\mathrm{d}\theta/\mathrm{d}s = (537\ \mathrm{m}^{-1} \times 3.01) \times 10^{-6}\ \mathrm{m\ s}^{-1} = 1.6 \times 10^{-3}\ \mathrm{rad\ s}^{-1}$, which matches with the mean of the angular drift profile shown in Figure 4.12(a). Similarly, I can also show that the angular drift with respect

to the path $\mathrm{d}\theta/\mathrm{d}s$ is similar to the curvature of the filament, as illustrated in Figure 4.12(b). In general, $\mathrm{d}\theta/\mathrm{d}s$ is the curvature of the path traced by the filament. The change in path curvature should help the filament to explore different areas of its environment.

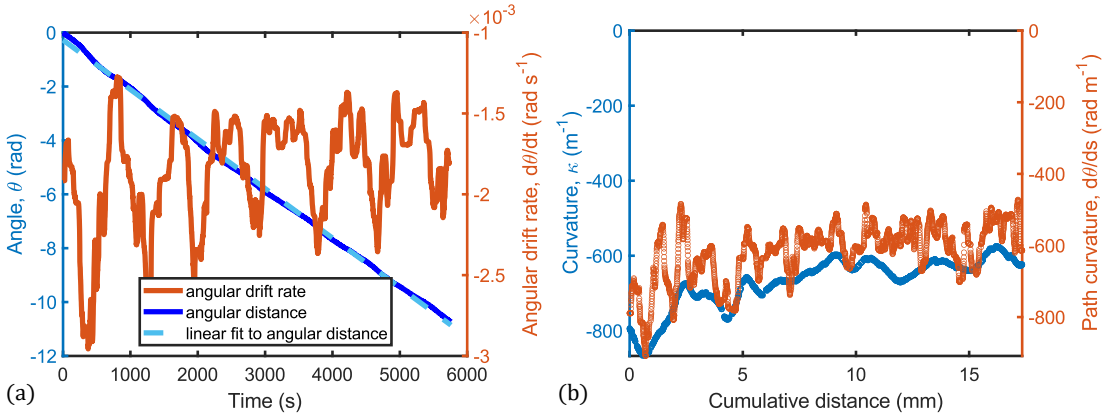

Figure 4.12: Angular drift in *O. lutea*. (a) Angle data for a filament moving in a clockwise motion (decreasing angle), based on data in Figure 4.5. The rate of change of angle $\mathrm{d}\theta/\mathrm{d}t$ is roughly constant, but has a periodic component, as expected from the periodic behaviour of filament speed seen in section 4.3.2. (b) The angular variation with distance travelled $\mathrm{d}\theta/\mathrm{d}s$, measured by tracking the midpoint, does not show this periodic term, demonstrating that it results from the velocity variations only. However, $\mathrm{d}\theta/\mathrm{d}s$ does closely match the curvature of the filament κ.

4.3.4 Filament rotation and tip motion

In section 4.3.2 I mentioned that the tails or the ends of a gliding filament of *O. lutea* were observed to wiggle periodically through the corkscrew rotational behaviour of the filaments. The frequency of this wiggling behaviour can be used to measure the frequency of rotation of the filaments. In this section, I will quantify the frequency of these rotations. To capture the rotation of the filament, I compared the orientation of the middle part of the filament with the leading end of the filament. The choice is based on an observation given earlier, which showed that the leading tip oscillates with a larger amplitude than the trailing end, thereby making its oscillations data easier to analyse.

Since the orientation of the middle part of the filament represented the average orientation of the filament, the fluctuations in the orientation of the leading end can be found by subtracting the orientation angle of the middle part of the filament from that of the leading end, *i.e.* $\theta_{leading\ end} - \theta_{middle}$. Usually, the data captured had gaps accounting for the time to move the microscope

stage. For high-frequency oscillations like the ones investigated here, such gaps in the data can affect the output of the computations. For this reason, I divided my data into pieces of continuous data sets and analysed each part separately. Figure 4.13 shows an example of a piece of data for $\theta_{leading\ end} - \theta_{middle}$.

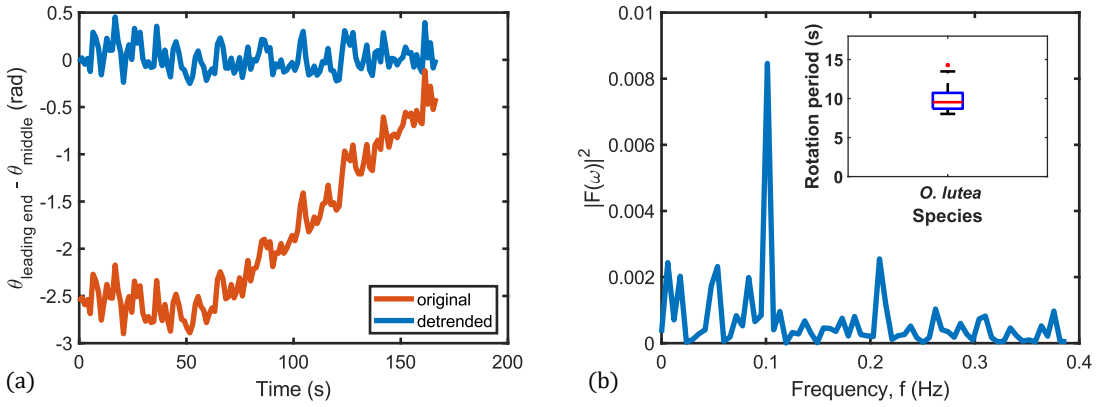

Figure 4.13: Cyanobacteria filament rotation analysis. (a) The wiggling behaviour of the filament is captured by comparing the orientations of the middle part of the filament and the leading end of the filament. Data is broken down into series of continuous data, one of which is shown here and detrended to flatten it as shown. (b) Fourier transform of the detrended signal was computed using the *fft* function in Matlab to produce the power spectrum shown. The frequency spectrum shows that the dominant frequency is 0.101 Hz, which corresponds to a period of about 9.9 seconds. Such periods were averaged for each filament and the insert shows a summary of the measured periods of filament rotation from 23 different filaments, which range between 8 and 14 seconds. On the box, whiskers indicate extreme points, a line gives the median, and the bottom and top edges of the box indicate the 25^{th} and 75^{th} percentile, respectively.

To determine the frequency of the rotation, I employed Fourier analysis. First, the signal was detrended as shown in Figure 4.13(a) and the result was then computed for the dominant frequencies using the Fourier transform function *fft* in Matlab, generating a frequency power spectrum as shown in Figure 4.13(b). The frequency spectrum in Figure 4.13(b) shows that the dominant frequency is 0.101 Hz, which corresponds to a period of about 9.9 seconds. Such dominant frequencies were computed for all other pieces of data for a given filament and then averaged. The insert in Figure 4.13(b) shows a summary of the measured average periods of filament rotation from 23 filaments, which range between 8 and 14 seconds (10 $\pm$ 2 seconds, mean $\pm$ SD), much lower than the period of oscillation in speed measured earlier.

4.3.5 Curvature fluctuations have a correlation time

In section 4.3.3 it was shown that the curvature of the path taken by single gliding filaments changes with time. It was further suggested that this mechanism can be biologically important for the filament to explore different areas of its environment, rather than moving in one circular loop. In chapter 3, I also showed that the isolated filaments attain a well-defined curved shape. There, the curvature of the isolated active filaments was quantified by fitting a circle to the filament skeleton and the results showed that the curvature distribution is centred away from zero. The measured curvature in chapter 3 was a static curvature because the observations were made without time variation. In this section, I analyse the dynamic curvature of single filaments, and the variation of the curvature of the path the filaments took, given by $\mathrm{d}\theta/\mathrm{d}s$. I analyse these by measuring their persistence time or their correlation time.

To begin with, Figure 4.14(a) shows two curvature signals: filament curvature κ_f and the curvature of the path $\mathrm{d}\theta/\mathrm{d}s$. Filament curvature was measured by fitting a circle to the shape of the filament, after converting it to a skeleton, as discussed in section 4.2, and tracking the variations of this through time. On the other hand, the curvature of the path taken by the filament was measured by looking at the change of the orientation of the filament (taken from the orientation of the middle part of the filament, as discussed in section 4.3.3) with the distance travelled. This is equivalent to analysing the variation of the tangent vectors along the path of the filament. Furthermore, filament curvature was assigned a negative sign when the filament was moving in a clockwise motion and a positive sign when moving counter-clockwise. This meant that both the values and the signs of the filament curvature and path curvature were comparable, as shown in Figure 4.14(a).

As can be seen from Figure 4.14(a), the two signals have some local variations which should be smoothed out to remain with only the long-term evolution of the curvatures. The local variations of the curvature signal were filtered out using the Savitzky-Golay [163, 164] filter as has been done for *e.g.* analysing similar behaviour in microtubules [165]. Savitzky-Golay data filtering is based on a local least-squares polynomial approximation. By fitting a polynomial to a set of input samples and evaluating the resulting polynomial at a single point within the interval, a Savitzky-Golay filter acts like a low-pass filter, depending on the choice of the order of the polynomial and the frame length or the sliding window size. The data shown in Figure 4.14(a) was smoothed in Matlab using *sgolayfilt* algorithm employing a third-order polynomial with a frame length of 1501 points. The choice of the order of the polynomial and frame length was based on finding a filtering algorithm that matched the path curvature profile with the filament curvature profile. Usually, the path curvature data was noisy due to the way it was computed

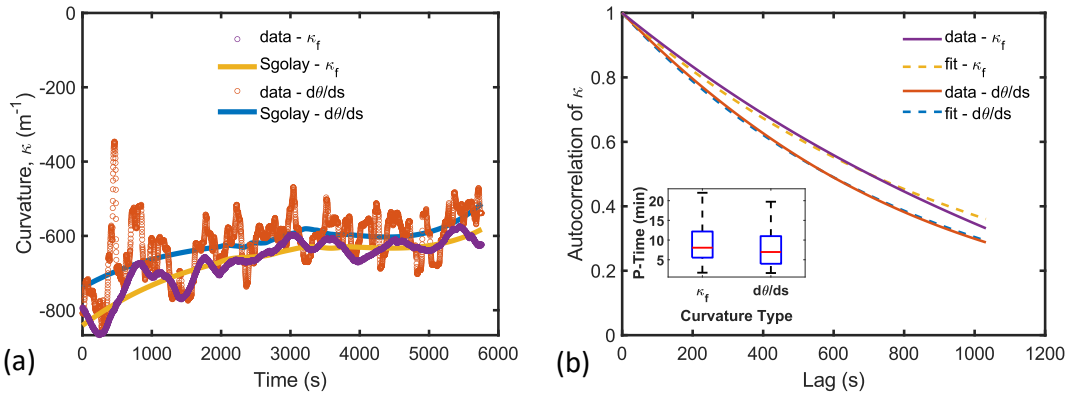

Figure 4.14: Filamentous cyanobacteria dynamic curvature. (a) Example filament curvature κ_f and path curvature $\mathrm{d}\theta/\mathrm{d}s$ data plotted alongside corresponding filtered signals, using the Savitzky-Golay filter. (b) Example autocorrelation analysis for path and filament curvatures shown in (a), with fitted exponential function $e^{-\tau/\tau_0}$. The distribution of curvature persistence time τ_0 for 23 different filaments is shown in the figure insert with mean values of 9 ± 5 minutes and 8 ± 5 minutes (mean ± SD) for filament curvature and path curvature, respectively. On the boxes, whiskers indicate extreme points, a line gives the median, and the bottom and top edges of the box indicate the 25^{th} and 75^{th} percentile, respectively. Part of the figure is adapted from [91].

via numerical derivatives. The filter removed these weak local fluctuations so that the analysis should focus on long-term variations.

The filtered signal for curvature data was used to quantify curvature correlation time by calculating the autocorrelation of the signal. Autocorrelation of a signal measures the degree of similarity between a given time series $y(\tau)$ and a lagged version of itself $y(\tau + L)$ where L is the lag [166]. The autocorrelation of the signal was computed in Matlab using the *autocorr* function. Fitting the result with an exponential function $e^{-\tau/\tau_0}$, I found the autocorrelation time of curvature, τ_0, to be in the range 1.7–22 minutes (9 ± 5 minutes, mean ± SD) and 1.6–19.7 minutes (8 ± 5 minutes, mean ± SD) for filament curvature and path curvature, respectively. Figure 4.14(b) shows an example of the computed autocorrelation profiles together with the exponential fit. An insert in Figure 4.14(b) shows the distribution of the measured curvature autocorrelation times in the form of a box plot. The autocorrelation time for curvature is one of the key parameters for describing the behaviour of active nematic filaments [165, 167] like filamentous cyanobacteria, as will be discussed in section 4.4.

4.3.6 Filaments reverse their motion randomly but maintain clockwise motion

Being autotrophs, cyanobacteria rely on light to photosynthesize. Therefore, cyanobacteria are known to have developed mechanisms of seeking or moving away from certain lighting conditions, a behaviour known as phototaxis [168–170]. Cyanobacteria are also able to respond to chemical gradients [171]. In all these responses, motile cyanobacteria tend to move towards favourable conditions in their environment. To easily explore different regions in their environment, some species of cyanobacteria, such as *O. lutea*, employ a reversal motion where the polarity of the head or tail changes. The frequency at which filamentous cyanobacteria reverse their motion is reported to be relatively random, and the average value in the literature range between minutes to hours [168, 172].

In this study, the goal was to quantify the reversal frequency of *O. lutea* in their normal setting. However, it is difficult to avoid the influence of light on the observed behaviour of light-dependent species like *O. lutea*, especially when observations are made under light microscopy. I investigated the reversal behaviour of filaments using fluorescence light microscopy (Leica TCS SP5) with excitation light at 543 nm. A total number of 23 filaments were investigated. Some filaments were seen to sense lighting gradients by reversing their motion at, or "bouncing off", the field of view boundary. Such observations were excluded from this analysis. Filaments were manually tracked for reversal, by playing a series of images in ImageJ software [85] while taking note of the times the filament reversed its motion. There were up to three records made per data set: the period of time from the start of observation to the first point of reversal t_1, the period of time between two reversal instances (observed reversal period) t_2, and the period of time between the last reversal instance and the end of the observation t_3. The distribution of the observed reversal period is shown in Figure 4.15(c).

The distribution presented in Figure 4.15(c) consists of all observed periods in all the 23 filaments studied. However, within a given filament the reversal periods were mainly random. For example, one filament had reversal periods of 9.4, 24, and 22 minutes, in that order. Also, as pointed out earlier, some filaments appeared to respond to the lighting gradient as they could be seen bouncing off at the boundary of the field of view. Such light-motivated reversals were excluded from the scatter plot shown in Figures 4.15(c) and (d) and often had very short reversal times. In general, the reversal periods ranged between minutes to a few hours, similar to what was observed in other cyanobacteria species [168, 172].

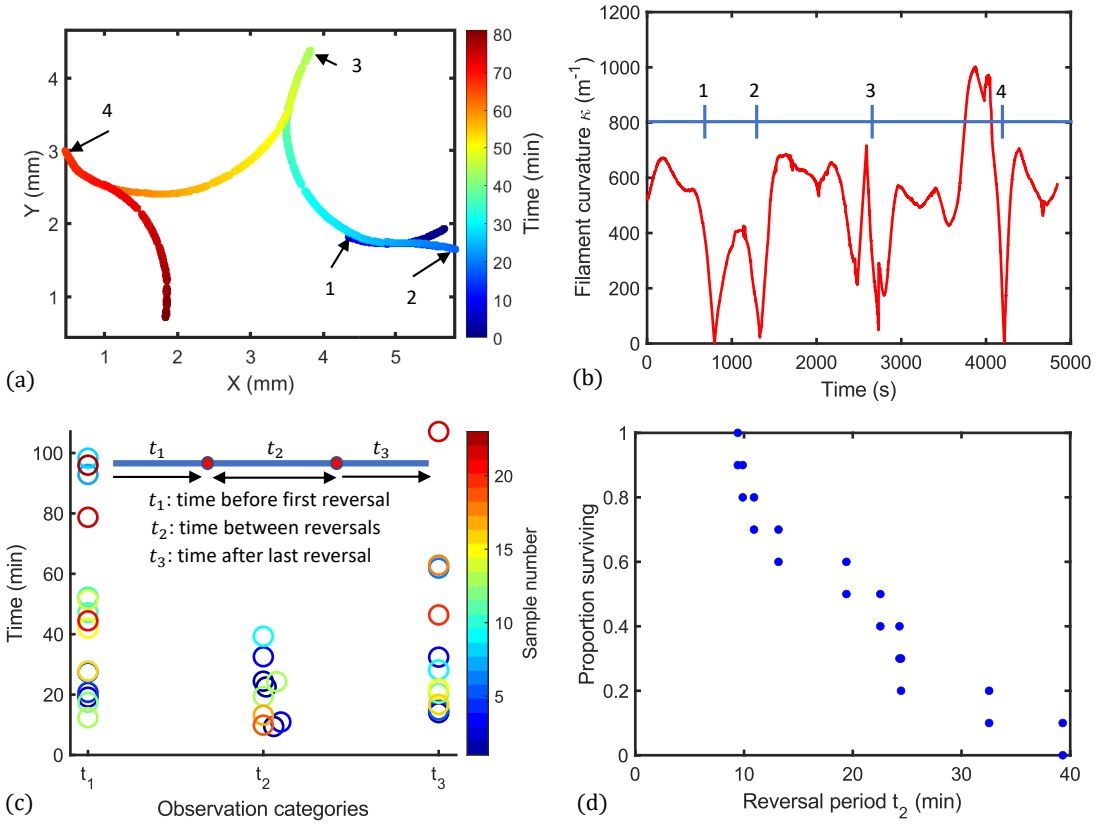

Figure 4.15: Filament motion reversal analysis in *O. lutea*. (a) An example motion track of the midpoint of an isolated filament of *O. lutea* showing 4 reversal events. The filament maintains a clockwise motion even after reversing its direction. The points of reversals are marked in their order. (b) During a reversal, the curvature is disrupted but returns to similar values after negotiating the reversal. Here the curvature of the filament for the track in (a) is shown alongside numbers marking the positions of reversal. (c) The distribution of reversal periods starting with the period of time from the start of observation to the first point of reversal t_1, the period of time between two reversal instances (observed reversal period) t_2 and the period of time between the last reversal instance and the end of the observation t_3. From the colour codes, which indicate sample numbers, it is noted that a single filament can have varied reversal periods. (d) Survival distribution of the period of time between two reversal instances (observed reversal period) t_2. The distribution shows that half of the observed reversal periods were 20 minutes and above.

4.4 Discussion

Quantification of the key behavioural features of active systems contributes in a fundamental way to understanding their collective behaviour. In modelling the collective behaviour of active nematic particles, a class of systems that filamentous cyanobacteria belong to, the dynamic properties of the particles such as speed and angular variation, and the interactions between the particles are considered the key features [165, 173]. For example, Sumino *et al.* [165] developed a model for the collective organisation of microtubules where the position X_i of a particle i changes with respect to a constant speed v_0 and orientation θ_i as

$$\frac{d\boldsymbol{X}_i}{dt} = v_0(\boldsymbol{e}_x \cos\theta_i + \boldsymbol{e}_y \sin\theta_i) \tag{4.1}$$

In the case of filamentous cyanobacteria, the speed of the filaments would be 3.01 ± 0.70 μm s^{-1}. In Sumino *et al.* [165], the orientation of the particle varies according to an Ornstein-Uhlenbeck process

$$\frac{d\theta_i}{dt} = \omega_i + \frac{\alpha}{n_i(t)} \sum_{j\sim i} \sin 2(\theta_j - \theta_i) \tag{4.2}$$

where the last term in Equation 4.2 is the change in the orientation due to the interaction between particle i and any nearby particles within a defined interaction range. The parameter α defines the strength of the interaction and can be varied. The strength of interactions or the probability of one cyanobacteria filament aligning with another after the collision will be investigated in chapter 5. Sumino *et al.* complete their model by arguing that the rate of change of the orientation of microtubules ω_i in Equation 4.2 evolves as

$$\frac{d\omega_i}{dt} = -\frac{1}{\tau_0}(\omega_i - \omega_0) + \xi(t) \tag{4.3}$$

where ω_i fluctuates around a preferred non-zero angular velocity $\omega_0 = v_0\kappa_0$ induced by the mean curvature of the filaments, κ_0. The correlation time for ω_i is given as τ_0, while $\xi(t)$ is a Gaussian white noise source with zero mean. In this chapter, I have found the correlation time for the path curvature as 8 ± 5 minutes. The preferred curvature of isolated cyanobacteria filaments was quantified in chapter 3 where it was found that active *O. lutea* filaments preferred a curvature of 537 ± 228 m^{-1}. However, as shall be seen in the next chapter, this preferred curvature is lost significantly when filaments interact, such that a mean curvature of zero, with some random variations, could well describe the shape of cyanobacteria filaments in a denser colony.

Similar models of active nematic particles [165, 173] have been applied to other studies such as *C. elegans* [167] and *Pseudanabaena* sp. [174]. My collaborators at the University of Loughborough, Dr. Marco G. Mazza and Jan Cammann have also developed a modified model suitable for the numerical study of collective behaviour in filamentous cyanobacteria based in good part on the observations in this chapter and chapter 5. Their model is described in chapter 6.

4.5 Conclusion

In this chapter, the dynamic properties of isolated gliding cyanobacteria filaments were quantified. Focusing on *O. lutea*, the chapter revealed that isolated filaments of glide with a speed of 3.0 ± 0.7 μm s^{-1}. It was further shown that the speed has weaker periodic fluctuations around this average value, with a period of 15 ± 11 minutes. Filaments were found to move in approximately circular paths, with a preference for a clockwise motion. The clockwise motion has been attributed to the presence of helical structures on the surface of these species by Read *et al.* [44]. The curvature of the paths taken by the filaments had an autocorrelation time of 8 ± 5 minutes. As cyanobacteria filaments glide on a substrate, they also change their shape with an autocorrelation time of 9 $\pm$ 5 minutes, similar to the change of the curvature of the paths they take. Such results can be used as inputs or constraints to model the collective behaviour of filamentous cyanobacteria by treating cyanobacteria filaments as active nematic particles [165, 173]. In chapter 6, a model developed by my collaborators at Loughborough University, following the parameters quantified in this chapter and chapter 5, will be presented and its results will be compared with experimental observations of collective behaviour.

Following earlier observations that filamentous cyanobacteria such as *O. lutea* rotate along their long axis as they glide [44], I measured the periods of filament rotation by tracking the wiggling pattern of the leading end of the filament. Results showed that *O. lutea* filaments rotate with a period of 10 ± 2 seconds (mean $\pm$ SD). This information, although not directly linked to the rest of the chapter, provides insights into the gliding behaviour of filamentous cyanobacteria, a means of locomotion that is not fully understood.

Furthermore, it was confirmed that the reversal rates in *O. lutea* were relatively random within a filament and ranged between a few minutes to hours. It was also noted that some filaments responded to the lighting in the imaging window, influencing their behaviour and causing them to reverse more frequently than they normally might. This was determined by the tendency of such filaments to bounce off the boundary of the imaging area. Knowledge of reversal frequency in active nematic systems is important, especially for cyanobacteria confined to a 2D space where they have difficulty in crossing each other [175]. The study of cyanobacteria in 2D confined spaces is beyond the scope of this thesis, but the measured reversal frequencies could be useful to future collaborators who would be interested in further studies on cyanobacteria filaments in 2D confined spaces.

Finally, models of active nematic particles suitable for describing the collective behaviour of the filaments build on the isolated behaviour reported here but also have an interaction term in them. In chapter 5, the behaviour of cyanobacteria filaments when they interact with each

other or with walls will be investigated. The results from this chapter and chapter 5 will form the basis for the model to be presented in chapter 6.

Chapter 5

Cyanobacteria filament interaction with walls and other filaments

5.1 Introduction

In chapter 4, I presented my findings on the behaviour of isolated filaments, which included speed, angular drift, and reversal frequency. However, cyanobacteria filaments do not live in isolation but rather in groups or colonies [45, 176, 177]. In these colonies, individual filaments are in constant motion and interact with other filaments and boundaries. Through filament-to-filament interactions, cyanobacteria colonies can exhibit self-organised patterns that are easily observable at scales larger than the size of individual filaments [45, 47]. An example of a self-organised pattern observed in *Oscillatoria lutea* is shown in Figure 5.1.

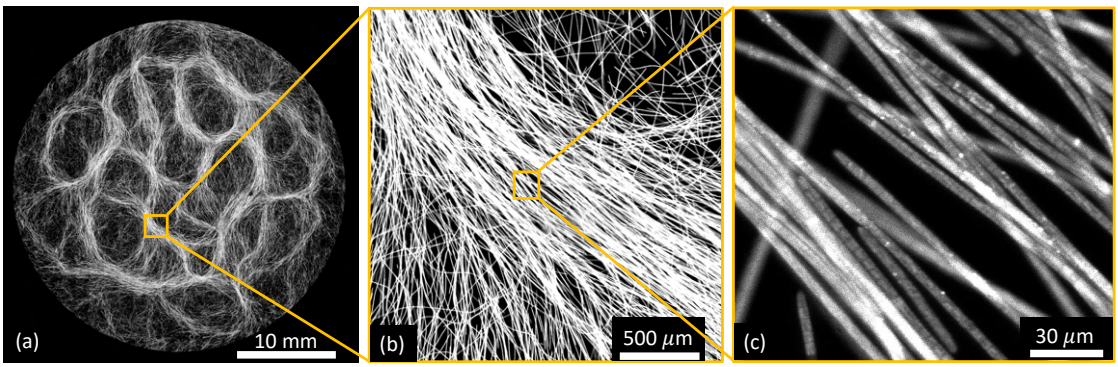

Figure 5.1: Example collective structure in *O. lutea*. (a) Through collective interaction, macroscopic structures like these are formed in filamentous cyanobacteria. (b) Close-up of a bundle of filaments showing the texture of the filaments. (c) High magnification view of the individual filaments forming part of the bundle. Adapted from [159].

Cyanobacteria are just one of the many living systems that exhibit self-organisation, an emergence of order based on local interactions of the members without any central authority.

Other systems that display self-organisation include flocks of birds [178,179], schools of fish [180], and herds of animals [181]. Numerical models of self-organised systems both in biology [182] and physics [183] have shown that simple rules of interaction between individuals are enough to reproduce collective behaviour seen in such self-organised systems. However, the rules of interaction may differ between different groups of living systems, depending on their nature and the environments they live in. In this chapter, the rules of interaction between pairs of cyanobacteria filaments will be studied.

Cyanobacteria colonies are also found in different geometries, for example where they interact with the environment such as at walls or barriers. The presence of boundaries may affect the behaviour of a microorganism. For example, studies of the interaction between the single-celled green alga *Chlamydomonas* and walls [184] found that there was a preferential angle of scattering independent of the angle of incidence of the green alga as it hits a barrier. *Chlamydomonas*, as single-celled organisms, are morphologically different from the filamentous cyanobacteria being studied here. Their means of locomotion are also different, where *Chlamydomonas* are swimmers and filamentous cyanobacteria glide on substrates. Here, I will first quantify the interactions between cyanobacteria filaments in space by looking at the probability of filament alignment after a collision to understand how filaments might behave when they interact in their colonies. I will then study the interactions between a cyanobacteria filament and a wall or boundary, to understand how filaments might behave when placed in confinements. Experimental studies on the results of these interactions and their implications on filamentous cyanobacteria collective structure formation in an open space and in confinements are presented in chapters 6 and 7, respectively.

The filamentous cyanobacteria species studied in this thesis are among those associated with mat-forming [45] and closely aligned with those in stromatolites [2]. They also have potential applications in bioreactors [58, 59], where knowledge of the interaction between filaments and boundaries might help in designing advanced biofuel cells. In general, the goal of this chapter is to get a set of rules of interaction among filaments and between filaments and their surroundings. These rules, together with the rules obtained in chapter 4, will form a complete set of observations that can be used to build a model of self-organisation of filamentous cyanobacteria, either in an open space or in confined geometries. Such model building is being done in collaboration with a theoretical group (Dr. Marco G. Mazza and Jan Cammann) at Loughborough University. So far, the group has developed a model for collective behaviour in filamentous cyanobacteria that will be described in 6. Just as in chapter 4, I will focus on a single species, *Oscillatoria lutea*, for an in-depth investigation. Results from this chapter have been published [159].

5.2 Methodology

5.2.1 Cyanobacteria filaments pair-wise interaction

To quantify pair-wise interactions, moderately dense suspensions of filaments (about 10 filaments per mm^2) were transferred into well plates of diameter 3.4 cm and were stored in an incubator with controlled light and temperature as described in section 2.3. This density was suitable for observing frequent filament interactions as well as for being able to physically track individual filaments. After 24 hours, the sample was imaged using a confocal microscope (Leica TCS SP5) with imaging conditions as described in section 2.2. A section at the centre of the well was used to take a time series of images as filaments moved around and interacted with one another. The centre of the well was chosen to ensure that the behaviour of the filaments under study was not influenced by boundaries, but only by the other filaments. Both bright-field and confocal images were captured, as in the previous chapter, but only bright-field images were used for analysis. An example frame of the images collected is shown in Figure 5.2(a).

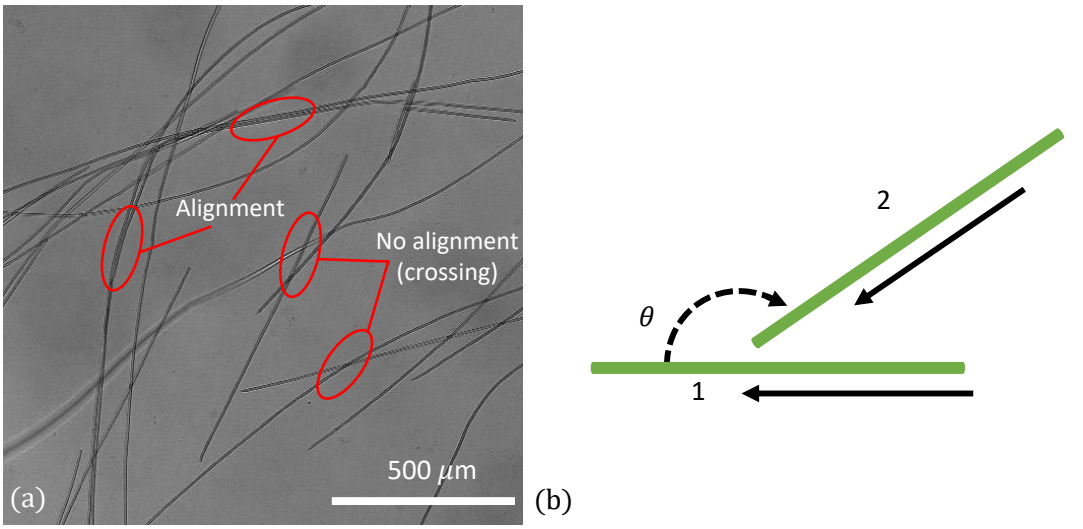

Figure 5.2: Quantification of filament interaction behaviour. (a) A snapshot of filaments moving in space, showing pairing or bundles (top). When they interact, two filaments can align, or cross, as shown. (b) An illustration of how the angle of interaction between filaments was measured. The angle was measured at the point of contact, tangent to the filament being crossed, in the direction of its motion, as demonstrated.

The series of images collected were analysed in ImageJ software [85] by manually counting the number of observed interaction events between filaments and recording the interaction outcomes.

For each interaction event, there were two possible outcomes: an alignment or no alignment (crossing). The angle of incidence was measured at the point of contact, tangent to the filament being crossed or aligned, in the direction of its motion, as demonstrated in Figure 5.2(b). Results are presented and discussed in section 5.3.1.

5.2.2 Cyanobacteria filament and wall interactions

The interaction between filaments and walls was quantified to understand how filaments would behave when in contact with boundaries *e.g.* when in confinement. Here, filaments were placed in a microfluidic channel (widths between 300 and 600 μm), as shown in Figure 5.3, and observed as they moved and collided with the walls. The widths of the channels were chosen to be less than the observed filament diameter of curvature $\sim$ 1 mm so that all filaments should bounce off the two side walls of the channel as they move in the channel. This increased the number of interactions observed. Observations were made under a confocal microscope (Leica TCS SP5) with settings as described in section 2.2. Both bright-field and confocal images were captured for analysis. Examples of images showing a cyanobacteria filament interacting with walls are shown in Figure 5.3. The angle of incidence was measured as the angle between the wall and the tangent to the convex side of the filament end that is colliding with the wall as illustrated in insert of Figure 5.3. The degree of alignment with the wall was quantified by measuring the distance that the filament travelled along the wall as shown on the right of Figure 5.3. Results are presented in section 5.3.2.

5.2.3 Variation of filament curvature with filament density

In section 3.3.3 it was observed that isolated free-gliding cyanobacteria filaments take a curved shape as they glide on surfaces. However, further observations in this project showed that filaments lose their well-defined curvature as filament density increases. In this chapter, the variation of curvature with density will be quantified. Since filaments in a given colony are in constant motion, the variation of filament curvature with density can also be thought of as the variation of curvature with filament interaction, where higher density means more filament interactions per unit time.

To quantify curvature variation with density, I measured the curvature of individual filaments in multiple cyanobacteria densities, some of which are shown in Figure 5.4(a-c). Filament curvature was measured as described in section 3.2.5, but here the procedure started with isolating each filament from the colony and then applying the method of measuring the curvature *i.e.* fitting a circle to the filament shape. To isolate a filament from a colony, I used Matlab's *polyline*

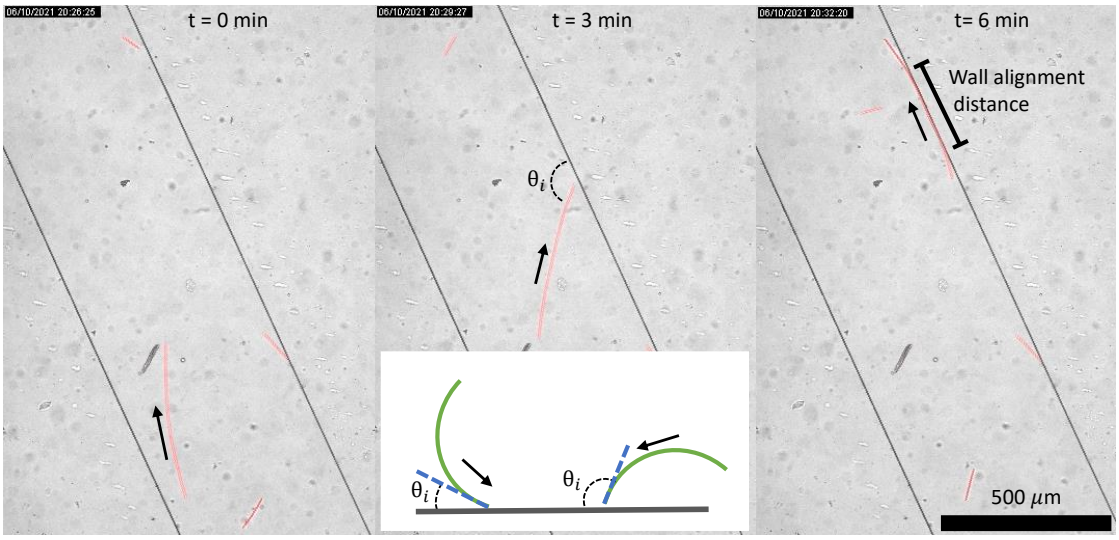

Figure 5.3: Quantification of filament-wall interactions. Left to right: Sequence of snapshots of a microfluidic channel (diagonal lines) showing the positions and the shape of a cyanobacteria filament (red) and tangents to the direction of travel (arrows). The middle panel shows how the angle of interaction was measured and that is highlighted by the insert figure at the bottom. The angle of interaction was measured as the angle between the wall and the tangent to the convex side of the filament end that is colliding with the wall. The right panel shows the distance that the filament travelled along the boundary as marked.

function to draw a segmented line 6 pixels wide (wider than the filament width of 2 pixels) along the contour of the filament of interest by hand. The area along the segmented line became a region of interest. I then converted the region of interest into a mask that was used to isolate the filament of interest from the rest. The resulting isolated filament was then converted to binary using a threshold of 0.4. The binary filament was then skeletonised to generate a filament backbone of one pixel wide to which a circle was fitted, as described in section 3.2.5. The procedure was repeated for all other filaments in the image and for images of different filament densities. The traces for each filament measured in a colony are plotted over the original filaments in green, in Figure 5.4(d-e).

5.2.4 Motion of filaments in bundles

When a dense colony of cyanobacteria filaments is left to stand for hours to days, polygon-like patterns like those shown in Figure 5.5, and also observed in Ref. [45], are formed. I wanted to understand how filaments move in these emergent bundles that are formed. Filaments in bundles

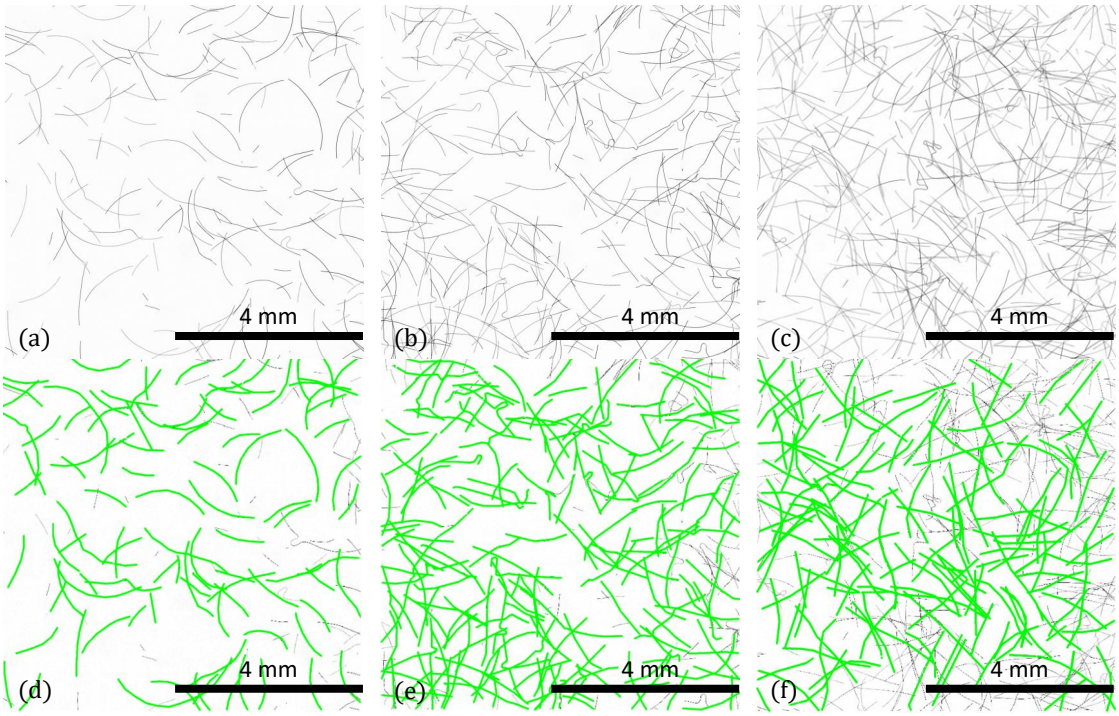

Figure 5.4: Quantification of filament curvature with filament density. (a)-(c) Raw images of some of the different filament density systems used to quantify curvature change with density. ((d)-(e) Raw images shown in (a)-(c) superimposed with traces of individual filaments that were used for curvature analysis.

are highly aligned, as shown in Figure 5.5. But the question is: how do filaments in bundles move? Do they all move in the same direction, or is the ordering into bundles independent of the direction of motion?

To answer the above questions, I studied the motion of filaments along the bundle shown in Figure 5.5(b-c). A series of images were collected at the points marked in Figure 5.5, along a bundle of filaments. Images for each point were saved as a video and played in ImageJ [85] software to measure the direction of the filaments captured moving inside the bundle. Since all the observations were made on the same bundle and the measured directions were correlated, the measurements from all the points marked in Figure 5.5 were combined, and statistical measures were made as discussed in section 5.3.4.

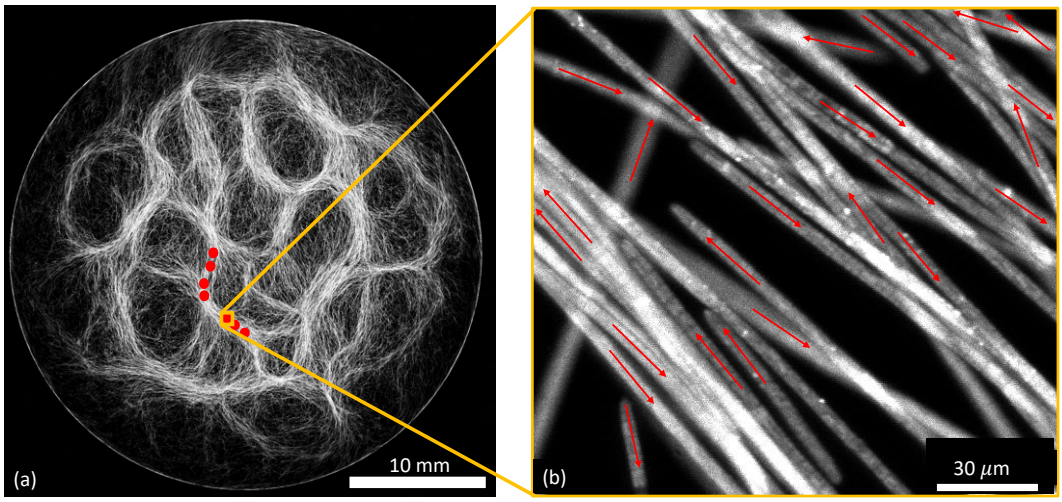

Figure 5.5: Measurement of the direction of motion of filaments in bundles. (a) A series of images was captured at the marked points in the figure and images were saved as videos. The saved videos were played in ImageJ [85] software for analysis of the direction of motion as discussed in section 5.3.4. (b) A closeup view of filaments at one spot in the bundle and their directions of motions marked. Adapted from [159].

5.3 Results

5.3.1 Cyanobacteria filaments pair-wise interaction

One behaviour that will contribute to the collective behaviour of filamentous cyanobacteria is the outcome after one filament collides with another as they glide on a substrate. When one filament collides with another filament, there were only two outcomes: crossing and continuing on with its initial direction of motion, or changing its direction and aligning with the filament it has collided into. By alignment here I mean moving either parallel or antiparallel to the direction of motion of the other filament.

As described in section 5.2.1, observations were made of filaments interacting in space, and the outcomes of their interactions were recorded as either 'alignment' or 'no alignment' for cases where the colliding filament aligns its direction with the impacted filament and when the colliding filament crosses the impacted filament, respectively. There were no cases of partial alignment, it was either a full alignment or crossing to continue with the initial direction of motion. The angle of interaction just before each collision occurred was also measured, as described in section 5.2.1. Here I present and discuss the results of such observations.

From a total number of 400 filament interactions that were observed, only 16 interactions resulted in filament alignment. This represents a probability of alignment of 0.04. This shows

that filaments mainly ignore each other when they meet in space, with a strong preference for continuing with their direction of motion rather than moving parallel to another filament. The interaction events that ended in alignment were further analysed in terms of the distribution of angles of incidence. This distribution is shown in Figure 5.6, where it is seen that filaments are more likely to align when they meet at angles closer to 0 or π radians. In other words, filaments aligned when they were already nearly aligned in their directions of motion. It can also be seen that filaments completely ignore each other when they meet at angles close to $\pi/2$ radians. Additionally, the alignment probability seems symmetric around alignment angle $\theta = \pi/2$ radians, evidence of nematic interactions between the filaments.

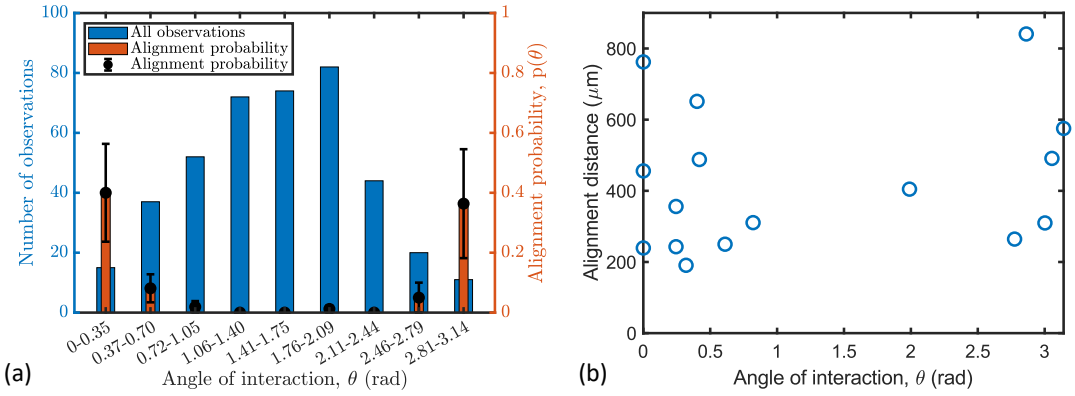

Figure 5.6: Cyanobacteria filament to filament alignment. (a) The probability of filament alignment is based on the angle of interaction between two filaments measured, where the error bars are standard errors. Also shown is a distribution of all the observed interactions. (b) Distribution of the distance or length of filament to filament alignment. The average alignment distance is 427 ± 197 μm (mean $\pm$ SD).

One other aspect of filament interactions is the breakup rate of pairs or bundles of filaments. To quantify the breakup rate of filaments from pairs or bundles, I measured the distance that a filament travelled along another filament after pairing. I call this the alignment distance. Alignment distances from the 16 alignment events observed in my data are shown in Figure 5.6(b). Based on the distribution of data in Figure 5.6(b), the breakup rate seems to be independent of the angle of interaction. To confirm this observation statistically, I performed a statistical test to check if the breakup rate was dependent on the angle of interaction and found that there was a weak positive correlation (Pearson correlation coefficient: $r(16) = 0.20, p < 0.45$), although the number of observations was limited. The mean value of the alignment distances is 427 ± 197

μm (mean $\pm$ SD). The breakup rate of filaments from pairs or bundles should be the inverse of the time a filament takes to cover the alignment distance i.e. $v_0/427$ μm or $\sim 0.007 \pm 0.004$ s^{-1} (mean $\pm$ SD). Here, $v_0 = 3.01 \pm 0.70$ μm s^{-1} (mean $\pm$ SD) is the average speed of the filament as measured in section 4.3.2. In the next section, I will show that the breakup rate of filament in pairs or bundles is similar to the dissociation rate of filaments from walls, supporting the idea that the interactions between the cyanobacteria filaments studied here are mainly influenced by physical factors. The calculated breakup rate of filaments in pairs or bundles will be useful in chapter 6, where I will use it to estimate the critical density for the collective organisation in colonies.

5.3.2 Cyanobacteria filament and wall interactions

Filamentous cyanobacteria are also found in environments where they continuously interact with boundaries, such as on rock surfaces [185], or rock pores where they can invade and cause damage [186]. In applications such as the production of algae-based biofuel [58,59], cyanobacteria are kept in fuel cells with walls or boundaries. It is therefore important to investigate how boundaries affect the behaviour of cyanobacteria filaments. Here the interactions between filamentous cyanobacteria and walls are quantified by specifically looking at how long filaments travel along the walls after colliding into them. Alternatively, the length over which a filament glides along the walls after a collision can also be taken as a measure of how much filaments like to stick to walls or boundaries.

As discussed in section 5.2.2, the interactions between filaments and walls were analysed by measuring the distance that each filament travelled along the wall after a collision, which I call here the wall-hugging distance. The angle of collision between the filament and the wall was also measured, as explained in section 5.2.2. The distribution of the wall-hugging distance with respect to the angle of collision is shown in Figure 5.7(a). Here, the distribution of the data points shows that there is no clear strong dependence of the wall-hugging distance on the angle of collision. To confirm this observation statistically, I performed a statistical test to check if the wall-hugging distance was dependent on the angle of collision and found that there was a weak positive correlation (Pearson correlation coefficient: $r(106) = 0.28, p < 0.01$). This weak positive correlation could be attributed to the need for filaments to change their curvature significantly when they collide with walls at angles greater than $\pi/2$ radians (see an illustration in Figure 5.3(b)).

The results found here could also be useful when answering the question: how frequently do filaments break away from walls? The wall-hugging distance data shown in Figure 5.7(a) has

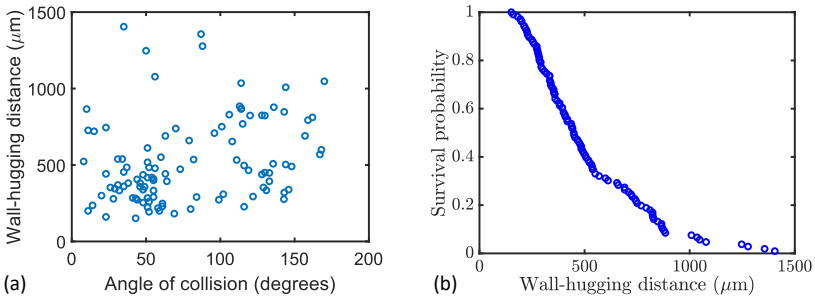

Figure 5.7: Filament-wall alignment results. The wall-hugging distance was the distance a filament travelled while in contact with the wall after a collision. An angle of the interaction of greater than $\pi/2$ means the filament was forced to flip its curvature (*e.g.* see Figure 5.3). (a) Shows a weak positive correlation between wall-hugging distance and the angle of the collision or the incidence angle (Pearson correlation coefficient: $r(106) = 0.28, p < 0.01$). (b) A survival plot showing the probability of observing a filament with a wall-hugging distance greater than the indicated wall-hugging times. Here, the observed wall-hugging times were between 150 and 1500 μm with a mean value of 520 $\pm$ 277 μm (mean $\pm$ SD).

a mean value of 520 $\pm$ 277 μm (mean $\pm$ SD). Similar to how I computed the breakup rate for filaments in pairs or bundles in the previous section, the dissociation rate of filaments from walls can be related to the inverse of the time a filament takes to travel through the wall-hugging distance i.e. $v_0/520$ μm or $\sim 0.006 \pm 0.003$ s^{-1} (mean $\pm$ SD). Again, for this conversion, $v_0 = 3.01 \pm 0.70$ μm s^{-1} (mean $\pm$ SD) is the average speed of the filament as measured in section 4.3.2. The computed filament dissociation rate from walls and the breakup rate of filaments from pairs or bundles are similar, which supports the experimental observations that the interactions between filaments in *O. lutea* are mainly influenced by physical factors.

I also analysed the distribution of data in Figure 5.7(a) in terms of survival analysis. Here I computed the probability of observing wall-hugging distances greater than any particular values. The computed probability profile is shown in Figure 5.7(b) and it is seen that less than half of the observations had wall-hugging distances ≥ 500 μm.

5.3.3 Effect of interactions on filament curvature

In section 3.3.3 it was shown that *O. lutea* filaments tend to acquire a smooth curved shape when they glide on surfaces. However, in my experimental observations, I noted that when multiple filaments are put together and interact, individual filaments tend to lose their curvature, especially as the density of the filaments increases. At higher densities, one could rarely see

perfectly curved filaments, like those seen in sparsely populated colonies. Filaments in high-density systems are instead seen with either lower curvatures or a more disordered shape. As described in section 5.2.3, curvatures of individual filaments were measured at multiple filament densities. The distribution of curvatures in these different densities is shown in Figure 5.8.

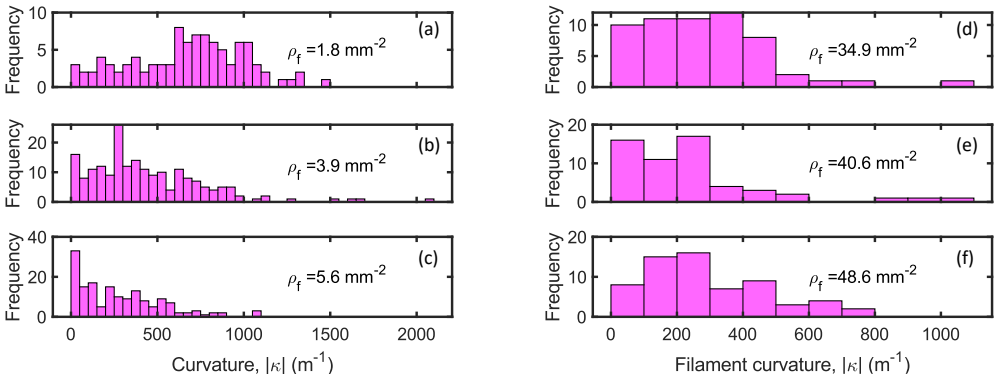

Figure 5.8: Curvature distribution in colonies of different densities. At a very low filament density in (a), the distribution of filament curvature appears to be centred away from zero. A slight increase in density in (b) and (c) forces the peak of the distribution to move to around zero. This is maintained in higher densities (d) to (f). The curvature was measured as an absolute value. Results published in [159].

From the curvature distributions shown in Figure 5.8, it is seen that in low-density colonies Figure 5.8(a), the peak of the distribution is away from zero, similar to the distribution of curvatures for isolated filaments shown in chapter 3. Above the density of 2 filaments per mm^2, the peak of the distribution of the filament curvatures shifts towards zero. The distributions still appear to have their peaks around zero in higher densities shown in Figure 5.8(d)-(f). As a summary for these distributions, a plot of the average filament curvature against density is shown in Figure 5.9.

The standard deviation of filament curvature δ_κ is one of the parameters for constraining a model for the behaviour of active nematics like filamentous cyanobacteria [165]. To quantify the standard deviation of filament curvatures in colonies, I used the measurements from the top three distributions shown in Figure 5.8. These densities were chosen because they represent the range of filament densities in both my experiments and the simulations. All curvature measurements shown in Figure 5.8 are absolute values. Therefore, having the peak of the distribution around zero as shown in Figure 5.8(c)-(f) means that the distribution of signed curvatures should be centred around zero. I, therefore, fitted a half-normal distribution function in Matlab using the function *fitdist(curvature, 'halfnormal')* to the ensemble of all filament curvatures from

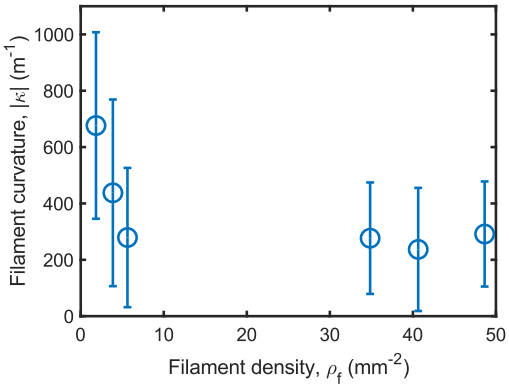

Figure 5.9: Effect of interactions on filament curvature. Filaments straighten as the interaction rate or density of filaments increases. Error bars are the standard deviations of the measurements. Adapted from [159].

Figure 5.8(d)-(f). The fitted half-normal function gave the standard deviation of the distribution as $\delta_\kappa = 340 \pm 40$ m^{-1}. This value of δ_κ estimated here was used by my collaborators in Loughborough to constrain their model as will be discussed in chapter 6.

5.3.4 Filaments in a bundle move equally in both directions

The directions of motion of filaments in a bundle were measured as described in section 5.2.4. A total of 417 filaments were observed and their directions of motion were measured. An example snapshot of filaments and their directions of motion is shown in Figure 5.10(a). Here, filaments are highly ordered and their directions of motion point almost equally in both directions of the local director *i.e.* the average orientation. This observation is supported by the ensemble of all orientations from multiple points along the bundle as shown in Figure 5.10(b). Here the polar histogram shows that filaments travel in either direction of the average orientation in approximately equal fractions (241 versus 176 filaments).

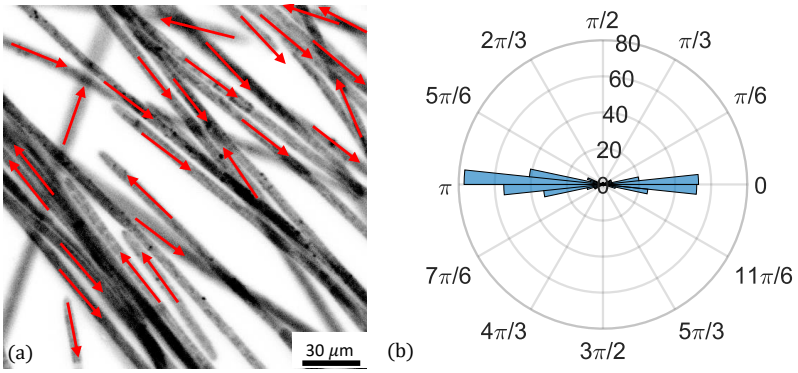

Figure 5.10: Direction of motion of filament in bundles. (a) An example snapshot of filaments in a bundle and their directions of motion (red arrows). Observations were made at multiple positions along a given bundle and videos of the images obtained were measured in ImageJ [85] to measure the directions of the filaments with respect to the local director. (b) A summary of the orientation angles of filaments in one bundle is shown as a polar histogram. The distribution shows that filaments move almost equally in both directions of the bundle and their directions are more aligned. Adapted from [159].

5.4 Conclusion

In conclusion, in this chapter, I have studied the basic interactions between filaments and walls or boundaries. First, found that individual filaments of *O. lutea* tend to ignore each other when they collide while gliding on a substrate. By studying 400 collisions between filaments gliding on a substrate, it was found that only 4 % of the collisions resulted in a filament aligning with another. By further studying the collisions that resulted in alignment, it was shown that filament alignment depended significantly on the angle of collision. Filaments completely ignored each other when they met at close to right angles and the probability of alignment increased with collision angles away from $\pi/2$ radians. This strongly favours alignment only for the case of collisions with angles of interactions near parallel or anti-parallel. It was also found that filaments travelled for a distance of 427 ± 197 μm (mean $\pm$ SD) while aligning with another filament. This observation was used to estimate the breakup rate of filaments at 0.007 ± 0.004 s^{-1} (mean $\pm$ SD), which is equivalent to a survival time of 142 ± 66 s (mean $\pm$ SD). This breakup rate is important for dynamics of clustering or pairing and will be used in chapter 6 to estimate the critical density for the transition between disorder and order in a cyanobacteria colony.

It was also shown that when filaments collided with walls, the wall-hugging distance at most weakly depends on the angle of collision. There was a slight increase in the wall-hugging distance when a collision forced a filament to change (flip) its curvature. Since the collision angles were

measured between the convex side of the filament and the wall, the collision angles were higher when the wall forced the filament to straighten its shape, thereby slightly increasing the time spent by the filament moving along the wall. The mean wall-hugging distance was found to be 520 ± 277 μm (mean $\pm$ SD). This result can be used to model the interaction between filaments and walls, especially for filaments in confined geometries, whose experimental observations are presented in chapter 7. Furthermore, I estimated the dissociation rate of filaments from the walls and found it to be $\sim 0.006 \pm 0.003$ s^{-1} (mean $\pm$ SD), equivalent to a survival time of 173 ± 92 s (mean $\pm$ SD). This result is similar to the breakup rate of filaments in bundles or pairs reported in the previous paragraph, which supports the experimental observations that the interactions between filaments in *O. lutea* are mainly influenced by physical factors.

Furthermore, it was shown that although isolated filaments take a curved shape when gliding on a substrate, the curvature significantly diminishes with increasing interactions or filament density. Curvatures of individual filaments in different densities were measured and the distribution of the measured curvatures with densities clearly showed a sharp decrease in the mean value between densities of 1 and 10 filaments per mm^2. Curvatures of filaments in higher densities remained low, with the peak of their distributions around zero. To quantify the distribution, I computed the standard deviation of the filament curvature distribution as $\delta_\kappa = 336$ m^{-1}. The standard deviation of filament curvature is one of the parameters for constraining a model of self-organisation in active nematics [165]. In the next chapter, I will describe a model that my collaborators in Loughborough developed, which used this parameter among many other parameters measured in this project.

Finally, in this chapter, I also investigated the motion of cyanobacteria filaments in bundles. By measuring the directions of motion of filaments in a bundle, it was found that filaments move equally in both directions of the bundle, with their directions more aligned. In general, these findings together with results of chapter 4 form a set of basic rules of filament behaviour that will be used to model self-organisation in filamentous cyanobacteria, as will be presented in the next chapter, along with my observations of the emergent structures seen in colonies of filamentous cyanobacteria.

Chapter 6

Cyanobacteria self-organisation in an open space

6.1 Introduction

Filamentous cyanobacteria are capable of self-organising into spatially differentiated structures when sufficiently dense filaments interact while gliding on a surface [45, 47]. The patterns that filamentous cyanobacteria form have been found to be similar to those found in fossilised stromatolites [45]. Indeed filamentous cyanobacteria, with their simple chains of connected cells, sit at the boundary between single-celled and multicellular organisms [187]. By understanding their behaviour, we could have insights into the evolution and complexity of life [188].

Previous experimental studies on self-organisation in filamentous cyanobacteria have been less quantitative [45], with models based on these studies [47] relying on rough estimates of some of the key parameters for their simulations. For example, the bending stiffness of filamentous cyanobacteria used in the model by Tamulonis et al [47] was based on estimated bending stiffness from Ref. [45], which in turn was based on persistence length measurements of their shape. Therefore a proper quantification of the bending stiffness of filamentous cyanobacteria is required, as done in chapter 3, for more accurate modelling.

Active nematic particles or filaments such as filamentous cyanobacteria could also be modeled by focusing on their nematic interactions, as demonstrated by the class of models of active nematic particles [165, 173], which have been applied to the models of *C. elegans* [167] and *Pseudanabaena* sp. [174]. Motivated by these models, my collaborators, Dr. Marco G. Mazza and Jan Cammann at the University of Loughborough, UK, have used my results from chapters 4 and 5 to develop a model of self-organisation of filamentous cyanobacteria which I will briefly present in the next section, before moving on to showing how it compares to my observations of pattern formation in dense cyanobacteria colonies. Results from this chapter have been published [159].

6.1.1 Model of self-organisation of filamentous cyanobacteria

Briefly, the model developed by Jan Cammann and Dr. Marco G. Mazza discretises a continuous filament into a series of connected beads or nodes. The head of the ith filament moves at constant speed $v_{0,i}$. Here $v_{0,i}$ is drawn from a normal distribution with $\langle v_0 \rangle = 3$ μm s^{-1} and standard deviation 0.7 μm s^{-1}, parameters that match my observations of isolated filaments of *O. lutea* in chapter 4. All filaments are set to a fixed length of $\ell = 1500\,\mu$m, which is the mean filament length of *O. lutea* measured here. The beads on each filament are separated by a distance $v_{0,i}\Delta t$, where Δt is the time step of the simulation. The rest of the filament glides along the path laid by the head, which advances at an orientation $\theta_i(t)$. Numerically, this is accomplished easily by removing at each time step the bead at its tail and attaching a new head bead.

Inspired by models of active nematic particles [165, 173] that have also been applied to the modelling of the behaviour of *C. elegans* [167] and *Pseudanabaena* sp. [174], the model includes a set of interactions appropriate to the observed behaviour of filamentous cyanobacteria from my thesis. The angle θ_i, governing the orientation of the filaments head, evolves according to an Ornstein–Uhlenbeck process

$$\frac{\mathrm{d}\omega_i}{\mathrm{d}t} = -\gamma \frac{\mathrm{d}\theta_i}{\mathrm{d}t} + \sqrt{2D_\omega}\xi_i(t) \tag{6.1}$$

$$\frac{\mathrm{d}\theta_i}{\mathrm{d}t} = \omega_i + \frac{\alpha}{N_i} \sum_{i\sim j} \frac{\partial}{\partial \theta_i} \cos\left[2(\theta_i - \theta_j)\right], \tag{6.2}$$

where $\gamma = 1/\tau$, with τ =480 s the curvature autocorrelation time, as measured in chapter 4; the orientational diffusion coefficient $D_\omega = \gamma \langle v_0 \rangle^2 \delta\kappa^2$ with curvature spread $\delta\kappa = 200\,\mathrm{m}^{-1}$, similar to the standard deviation of filament curvature in colonies as measured in chapter 5; $\xi_i(t)$ is a Gaussian white noise source with zero mean and unit variance. N_i denotes the number of filaments currently within the interaction range $d = 5\,\mu$m of the i-th filament's head, where d is based on the diameter of the filaments of 4.2 μm, as measured in chapter 3, accounting for the presence of a thin extracellular polymeric substances (EPS) sheath of < 1 μm. The sum $\sum_{i\sim j}$ in Equation 6.2 denotes a summation over all neighboring filaments of orientation θ_j following a nematic Lebwohl–Lasher potential with interaction strength $\alpha_s = 0.006\,\mathrm{s}^{-1}$. The choice of the value for α_s was based on the parameter value that produced results similar to the experimental observations as it is difficult to retrieve this value from experimental observations. The model factors are sketched in Figure 6.1.

6.1.2 Prediction of the phase transition point

It is evident from the studies in Refs [45,47] that the self-organisation of filaments of cyanobacteria is dependent on filament density. However, the density at which order emerges in a filamentous

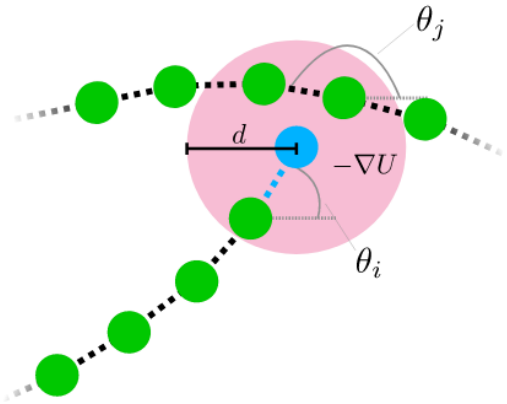

Figure 6.1: Schematic depiction of the filament-filament interaction in simulations. When the tip of a filament comes within a distance d of another filament, the angle of its advancing head will change according to the interaction potential $U = -\cos[2(\theta_i - \theta_j)]$, where θ_i is the angle of the incident filaments head and θ_j is the local angle of the other filament. Figure provided by Jan Cammann. Adapted from [159].

cyanobacteria colony has never been experimentally quantified. Here, based on the measured parameters of the behaviour of filaments from chapters 4 and 5, I will predict the point at which the interaction between filaments will become important and estimate when the transition between order and disorder should occur. For simplicity, I will consider a 'gas' of weakly interacting straight filaments of density ρ moving at constant speed v_0. If the filaments are oriented randomly as illustrated in Figure 6.2, on average they present to each other a cross-sectional length of

$$\bar{L} = \langle L \sin\theta \rangle = \frac{1}{\pi} \int_0^\pi L \sin\theta d\theta = \frac{2}{\pi} L \tag{6.3}$$

As one filament advances, it will therefore cross over other filaments at an average frequency $f = \bar{L}\rho v_0 = 2L\rho v_0/\pi$. Experimentally, most filament crossings have no effect, but a small fraction α results in the crossing filaments aligning nematically. The rate of filament ordering should therefore scale as αf. In contrast, I noted that aligned filaments would occasionally split up, a process that can be assumed as randomly occurring with the rate β. Under these simplistic but representative assumptions, the ordering interactions should become important when $\alpha f \simeq \beta$, and this cross-over can be used to define a characteristic density

$$\rho_c = \frac{\pi\beta}{2\alpha L v_0}, \tag{6.4}$$

with a value of $\rho_c \simeq 52 \pm 19$ filaments mm^{-2}, given the parameters in Table 6.1. A random

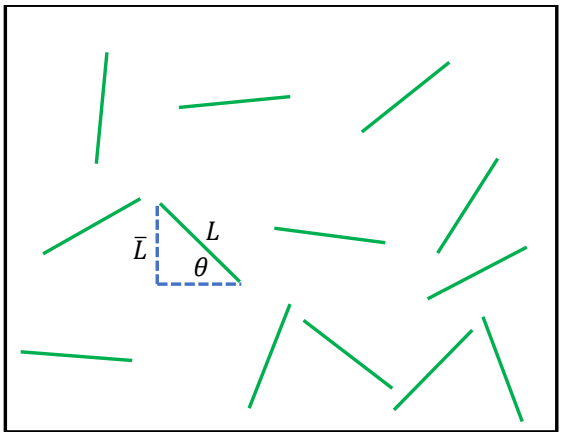

Figure 6.2: An illustration of a gas of filaments of cross-sectional length L, moving at speed v_0, and interacting with a probability α when they cross each other.

Table 6.1: A summary of the parameters used for the prediction of the phase transition point as quantified in Chapters 3 to 5.

Parameter	L (mm)	α	v_0 (μm s^{-1})	β (s^{-1})
Value	1.5±1	0.04 ± 0.01	3.0 ± 0.7	0.006 ± 0.003

disordered gas of filaments would be expected for densities $\rho \ll \rho_c$, with ordering behaviour expected at densities $\rho \approx \rho_c$ or above.

In general, this chapter presents the experimental study of self-organisation in filamentous cyanobacteria, focusing on one species, *Oscillatoria lutea*. Experimental results will be compared with the numerical results later in this chapter. In the following section, the methodology followed in conducting the experiments will be given.

6.2 Methodology

6.2.1 Sample preparation

Samples of *O. lutea* were cultured following the conditions given in section 2.3. A dense culture of the sample was transferred into a 50 ml glass tube and shaken to disentangle the filaments. Later, the shaken contents were transferred into a standard 3 x 2 well plate (each well with a diameter of 3.4 cm) filled with a BG 11 broth media diluted with deionised water to a ratio of 1:100. Different amounts of the sample were added to different wells, simply by varying the number of drops of the sample suspension. Up to 50 different setups (wells) were prepared and these were stored before

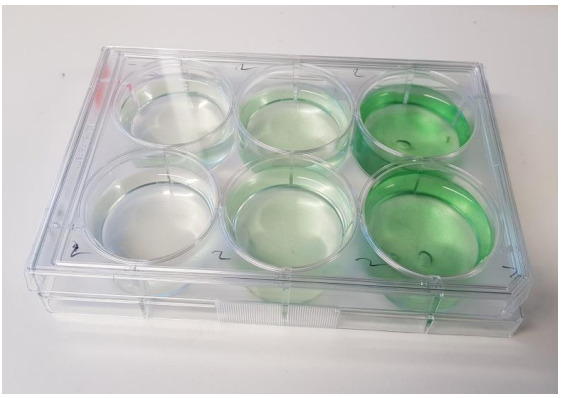

Figure 6.3: The experimental setup for structure formation in filamentous cyanobacteria growing in an open space showing a six-well plate dish with well diameter of 3.4 cm.

further use for 72 hours in the incubator used for storing the culture, as described in section 2.3. Usually, filamentous cyanobacteria are able to self-organise into their preferred patterns within 12 to 24 hours [45] after being disturbed or transferred into a new media. However, in this project, when a suspension of filaments was transferred into a well plate, the filaments initially clumped together as they settled on the base of the well plate. Individual filaments then spread throughout the chamber from these clumps to achieve a homogeneous distribution. The length of time to achieve a homogeneous distribution of filaments increased with the density of filaments in the chamber. Overall, it was observed that for all the filament densities studied in this project, a period of 48 hours was enough to achieve a uniform distribution. To this period, I added 24 hours to allow filaments to self-organise [45], taking the total period of time between sample transfer and observation to 72 hours. An example of a setup is shown in Figure 6.3.

6.2.2 Sample imaging

The samples described in section 6.2.1 were then imaged using confocal laser microscopy (Leica TCS SP5) with imaging settings as described in section 2.2.1. In brief, I took advantage of the presence of chlorophyll-a [83] in cyanobacteria to use 514 nm laser light for excitation and observed the resulting emission through a bandpass filter from 620 to 780 nm. The pinhole of the confocal microscope was set to the maximum width, thereby achieving a maximum depth of field of 81 μm. This ensured that filaments at different depths were captured in one focal plane. However, in certain cases, images were captured at different focal planes and later combined to form a single 2D image. This usually happened when the base of the well plate was not quite perpendicular to the objective lens, or when the layer of the filaments was thicker than the depth resolution.

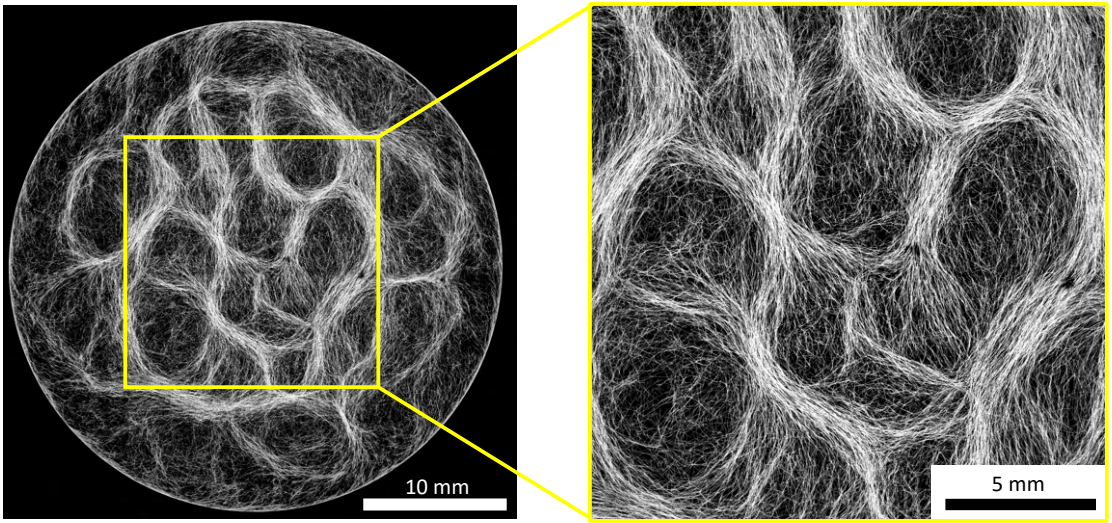

Figure 6.4: Example full well image of filamentous cyanobacteria collective structure. A region of 1.7 cm x 1.7 cm (right) was cropped at the centre of the image for analysis. Panel (a) adapted from [159].

A single confocal image covered a 1.55 mm x 1.55 mm area. Therefore, to capture the whole well of diameter 3.4 cm, the tile imaging feature of the confocal microscope was utilised, as described in section 2.2.1. An example of a full well capture is shown in Figure 6.4. To analyse the self-organisation of cyanobacteria filaments in an open space, I looked at the structure in the middle of the well, away from the effects of the boundary. For this reason, I cropped a 1.7 cm x 1.7 cm region at the centre of each well, as illustrated in Figure 6.4, and used the cropped image for further analysis.

6.2.3 Measuring filament density

Quantifying filament density started by getting a black-and-white image of the filament structure. To get such a binary image, I used Matlab function *imbinarize(Image, T)*, where T is the intensity threshold value that ranges between 0 and 1. The *imbinarize(Image, T)* function converts all pixels whose relative intensity is greater than or equal to the *threshold* to a pixel value of 1 and all other pixels to 0. For images with uniform brightness, a fixed threshold value also called the global threshold value, is often enough. However, for images with a more variable brightness or illumination, an adaptive threshold is required. An adaptive threshold applies different threshold values to different parts of the image ensuring that features in areas with low brightness are also captured, in a consistent way with features in brighter parts of the image.

In this project, I used the *adaptthresh(Image, sensitivity)* Matlab function to compute the appropriate threshold values for each region or pixel in an image. The function provides an option to choose the size of the neighbourhood to be used for computing the local statistics. I left this to the default value of $2 * floor(size(I)/16) + 1$, which sets the neighbourhood size to 1/8 of the image size. The sensitivity value in the *adaptthresh(Image, sensitivity)* function ranges between 0 and 1, similar to the threshold value in *imbinarize(Image, T)* function. However, unlike the parameter T, a high sensitivity value in *adaptthresh(Image, sensitivity)* gives more consideration to pixels with low-intensity values in a given region while a low sensitivity value gives less consideration. Low sensitivity values are good for images with low density of bright pixels *i.e.* with fewer features, as this helps the threshold algorithm to remove noise, which mostly happens to be pixels with low-intensity values. However, when the density of bright pixels is high, *i.e.* where there are more features or filaments, the low-intensity pixels in a given region might not be noise but filaments that are just not as bright as the majority of the bright pixels. Therefore, a more sensitive value for the threshold would be needed to include the low-intensity features as well.

For the reasons stated above, it is clear that if one is thresholding multiple images with different pixel densities or filament densities, as in my case, the sensitivity value of the adaptive threshold function should be variable. I have already indicated that high-density images will need a high sensitivity value for the *adaptthresh(Image, sensitivity)* function and that a low sensitivity value is appropriate for low-pixel-density images. Therefore, I decided that the best way to automate this process and to ensure uniformity in all the processes was to set the sensitivity value equal to a rough pixel density of each image. The rough pixel density of an image was computed by converting the image into binary using *imbinarize(Image, T)*, where T was set at 0.04. The choice of the threshold value here was based on the observation of the histograms for the images processed. The majority of intensities of pixels away from filaments had pixel intensities of less than 10. I, therefore, set the value of $T = 10/255 \approx 0.04$. From the resulting binary image, I computed the pixel density ρ_{pixel} by dividing the total number of white pixels by the total number of all pixels in the image. The inputs to the thresholding function, therefore, were *adaptthresh(Image,*ρ_{pixel}*)* and the output was passed on to the function *imbinarize(Image, T)* as the parameter T to generate a binary image. Figure 6.5 demonstrates the importance of varying the sensitivity value with the density using example low and high filament density images.

This approach of image thresholding allowed the sensitivity value to respond to different image densities and provided a robust way of converting various images to binary while minimising human bias. From the resulting binary image, I removed all particles or small bits of filaments

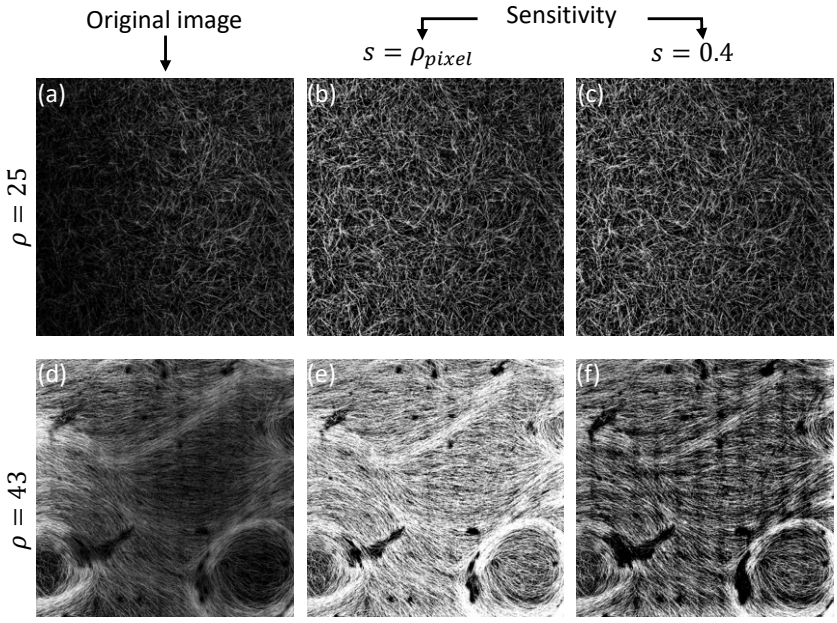

Figure 6.5: Demonstration of adaptive image threshold. Two images with different filament densities (a) and (d) are shown to illustrate the effect of fixed and variable sensitivity values in *adaptthresh(Image, sensitivity)* function on the resulting binary image. (a) is an original image and has a filament density of 25 filaments mm^{-2} with a shadowing effect on the left. Using a sensitivity value equal to its rough pixel density (≈ 0.4) in *adaptthresh(Image, sensitivity)* function, a binary image (b) is produced. (c) is the same as (b) with the sensitivity value fixed at 0.4 to act as a control for testing the effect of a fixed sensitivity value on other densities. (d) is an original image with a filament density of 43 filaments mm^{-2}. In (e), (d) is converted to binary using a sensitivity value based on its pixel density while in (f) a fixed sensitivity value similar to that used for a low-density image (c) was used to generate that binary image. It is clear that (f) looks less dense than the original image (d) while (e) closely matches its original image, showing that variable sensitivity based on rough pixel density used in the project provides reasonable outputs.

that occupied an area of fewer than 20 pixels using the function *bwareaopen*. From the resulting image, I computed the filament density ρ_f as

$$\rho_f = \frac{N}{N_0 A}$$

where N is the number of white pixels in an image, N_0 is the average number of pixels in one filament and A is the area of the image. On average, each filament was 2 pixels wide and the pixel size was 3 μm. The average filament length was taken to be 1.5 mm, making $N_0 = 990$ pixels. To check that the method was accurately quantifying filament density, I tested it on the

image shown in Figure 6.6(a) and picked 6 random 1 mm^2 regions across the image and counted the number of filaments in them. The average number of the filaments in a 1 mm^2 area was 12± 1 filaments, while the computed filament density was 13 filaments per mm^{-2}, showing that the method of measuring filament density was working properly.

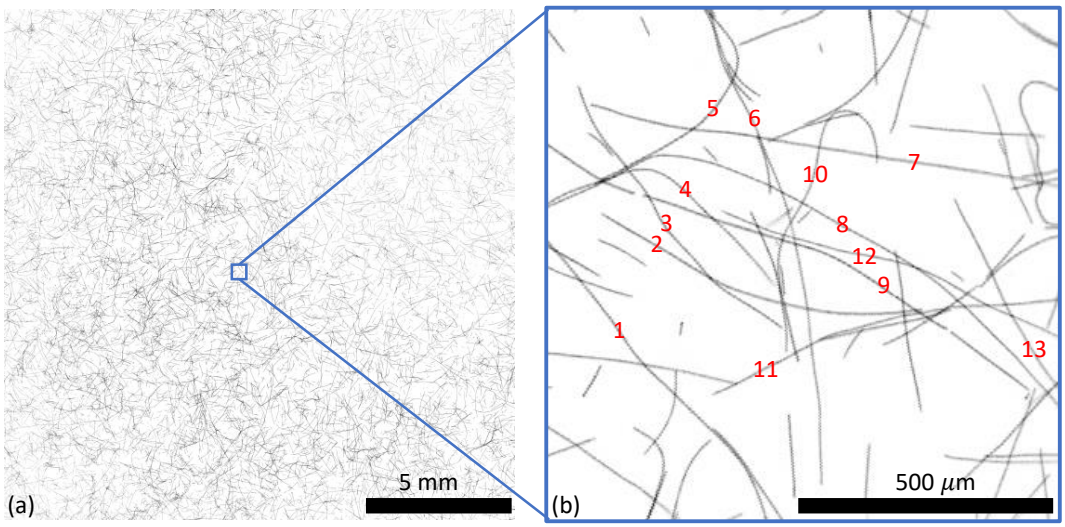

Figure 6.6: Verification of filament density measurement. The measured filament density using the process described in this section for the image in (a) is 13 filaments mm^{-2}. The average number of manually counted filaments from 6 random 1 mm^2 areas from the same image was 12 ± 1 filaments (mean ± SD). This showed that the method of filament density measurement was working as expected. An example of a 1 mm^2 region is shown in (b). Here there are about 13 filaments with lengths ≥ 500 μm (marked). All the smaller filaments contribute to the average length. The actual measurements were based on pixel counting rather than counting the exact number of filaments in an area.

6.3 Results

6.3.1 Emergence of nematic order

To investigate the emergence of order in a filamentous cyanobacteria colony, I analysed the orientation distribution of filaments using the GTfiber app [189], which is Matlab-based fibre analysis software. The app converts a given filament structure image into a skeleton network where each filament is represented by a series of pixels defining a single-pixel wide line through its centre. Later, the skeletonised image structure was used to calculate the orientation of each filament at each and every pixel, as described in [189]. The output of this computation was an

angle map of size equal to the skeletonised image, but with additional information associated with every pixel on the skeleton, giving its angle relative to the horizontal. All other pixels on the skeletonised image were replaced with NANs on the angle map, allowing angle information to be displayed virtually through colour, as shown in Figure 6.7.

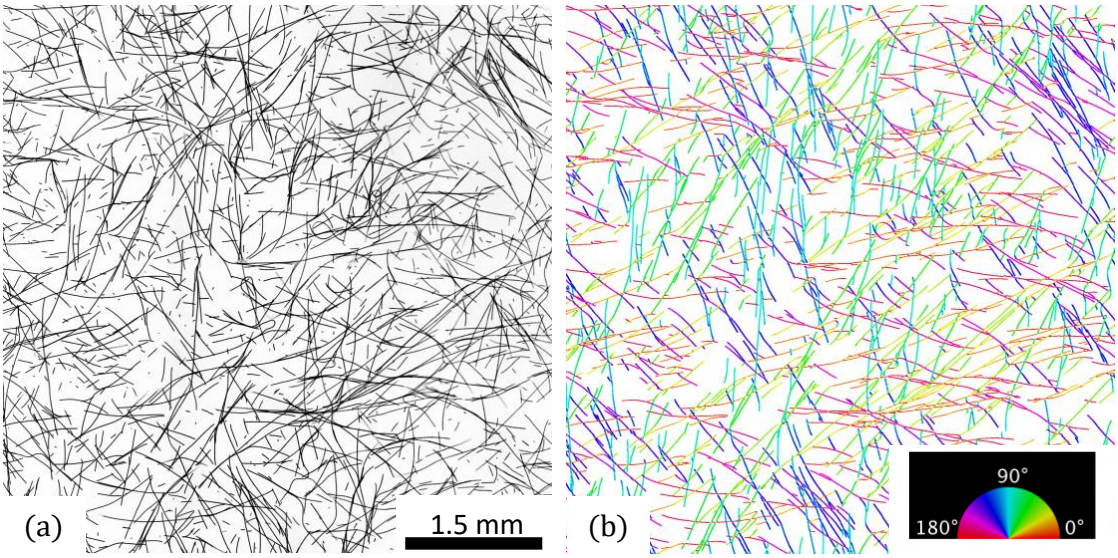

Figure 6.7: Generation of an angle map from a filament structure image. (a) An example of a raw image of a filamentous cyanobacteria structure is shown with an increased contrast for better visibility. (b) An angle map made from the image in (a), showing the orientation of each filament at the pixel level.

To quantify the nematic order of the filaments, the orientational order parameter, S_{2D}, sometimes referred to as the Hermans orientation factor [189–192], was employed. This parameter measures the degree of alignment of filaments and is mathematically defined as

$$S_{2D} = 2\langle \cos^2 \theta_n \rangle - 1 \equiv \langle \cos(2\theta_n) \rangle \tag{6.5}$$

where θ_n is the angle between a pixel on an individual fibre and the overall director $\vec{n}$ *i.e.* the average orientation, in an image or sub-image and the angled brackets represent an average over all relevant pixels on the skeleton. Here, S_{2D} varies between 0 and 1. In a scenario where the filaments are randomly oriented, $\langle \cos^2 \theta_n \rangle$ gives a value of 1/2, yielding an S_{2D} value of 0. When the filaments are perfectly aligned with each other, $\langle cos^2 \theta_n \rangle$ gives a value of 1, thereby yielding an S_{2D} value of 1. The overall director or the average direction of the filaments in a given image or sub-image was found by computing the structure tensor of the angles at each pixel and

averaging as

$$J_{average} = \frac{1}{N}\sum_{i=1}^{N}\begin{bmatrix} \cos^2\theta_i & \cos\theta_i \sin\theta_i \\ \cos\theta_i \sin\theta_i & \sin^2\theta_i \end{bmatrix} \tag{6.6}$$

for the N pixels in a given image or sub-image. The highest eigenvalue for $J_{average}$ corresponds to the order parameter, S_{2D}, and the corresponding eigenvector indicates the orientation of the average direction of the angles. However, there is a shortcut for computing the 2D order parameter S_{2D}, as given in Ref. [193]. Instead of first computing the average orientation of all angles in the image, the 2D order parameter can be computed directly from the angles using the formula

$$S_{2D} = \sqrt{(2A-1)^2 + 4B^2} \tag{6.7}$$

where

$$A = \frac{1}{N}\sum_{i=1}^{N}\cos^2\theta_i,$$

$$B = \frac{1}{N}\sum_{i=1}^{N}\cos\theta_i \sin\theta_i.$$

GTFiber app [189] uses this version for calculating the order parameter but it is mathematically equivalent to Equation 6.5.

In general, the 2D order parameter is calculated at different length scales of the image to generate a curve that shows how S_{2D} changes with the size of the domain used. To achieve this, each image is divided into boxes or tiles of a given size d and the order parameter is computed for each box. Later, an average value of the order parameter is calculated, for that specific box size. Sampled frames that do not have filaments in them are excluded from averaging, as the order parameter is not well-defined in that case. Figure 6.8 illustrates the process of computing the $S_{2D}(d)$ curve.

In order to compare the ordering of filaments from different images, I fixed the frame size d to 1 mm for computing S_{2D} in all the 50 images studied in this experiment. This length scale was chosen to the measure local order parameter so that I can characterise how the transition from disorder to order occurs with increasing density. By plotting the S_{2D} values of each image at the frame size of 1 mm against filament density, as shown in Figure 6.9, I observed a phase transition at filament densities between 40 and 50 filaments per mm^2 between a disordered "gas" of filaments and a well-ordered state. The phase transition occurs at densities close to those predicted in section 6.1.2. Results from the numerical model also show a striking resemblance both in the structure of the patterns and in the ordering transition, as shown in Figure 6.9. These results show that the self-organisation in filamentous cyanobacteria can be well-captured by a simple model, based on the collective nematic interactions of the filaments.

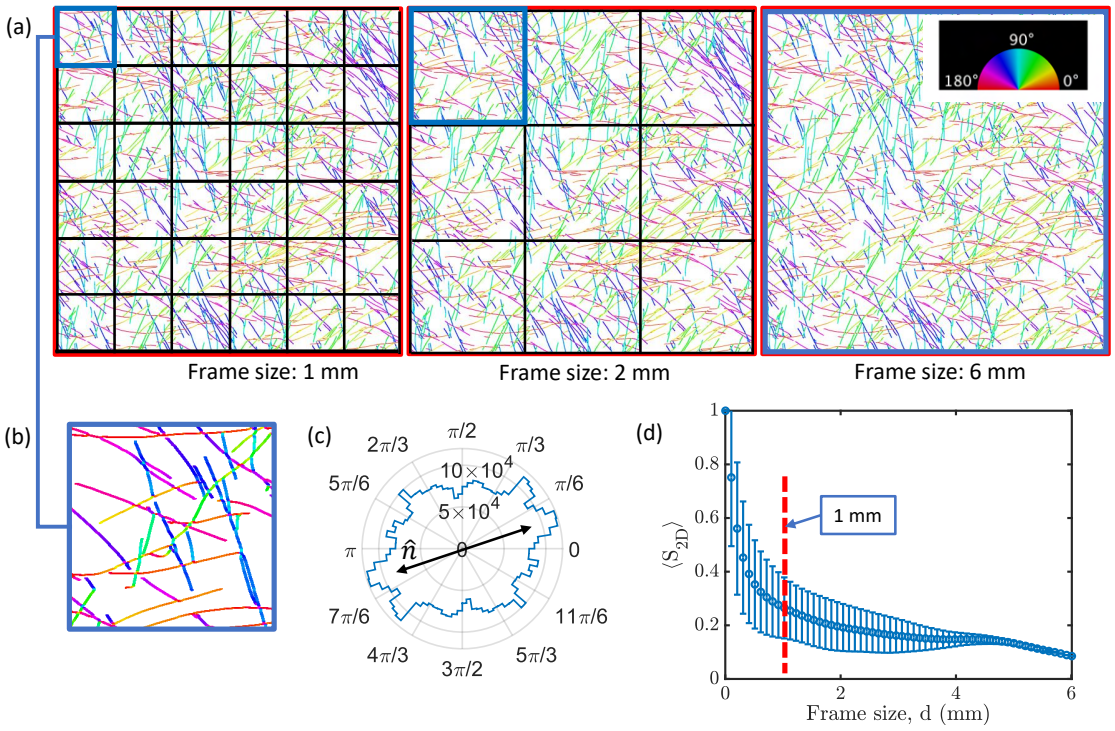

Figure 6.8: Calculation of S_{2D} from a skeletonised image. (a) Illustration showing how each skeletonised image was partitioned into boxes of different frame sizes. For each frame size, the S_{2D} was calculated in each box and the average and the standard deviation of the S_{2D} for all the boxes were calculated. (b) Closeup of a 1 mm x 1 mm frame showing the orientation of filaments in that frame. (c) The polar distribution of the directions of the filaments in panel (a) was measured at the pixel level. (d) S_{2D} plot with respect to frame size, for the image in (a). The error bars are the standard deviations of the S_{2D} for that particular frame size. The red line indicates the 1 mm length scale for sampling S_{2D} variation with filament density. Adapted from [159].

6.3.2 Structure size in filamentous cyanobacteria patterns

Beyond some critical density, filamentous cyanobacteria self-organise into patterns characterised by ridges that form reticulate patterns as seen in e.g. [45, 47] and Figure 6.4. I measured the size of these structures in two ways: first using the S_{2D} profiles as shown in Figure 6.8(d) and comparing the result with manual measurement of feature sizes. Using the S_{2D} profiles, I measured a characteristic size by making a log-log plot of the S_{2D} vs the region of interest (ROI) size or the area d^2 [194]. The plot shown in Figure 6.10(a) reveals the characteristic length (or area) at which correlation in structure ends. This appears at the higher filament density

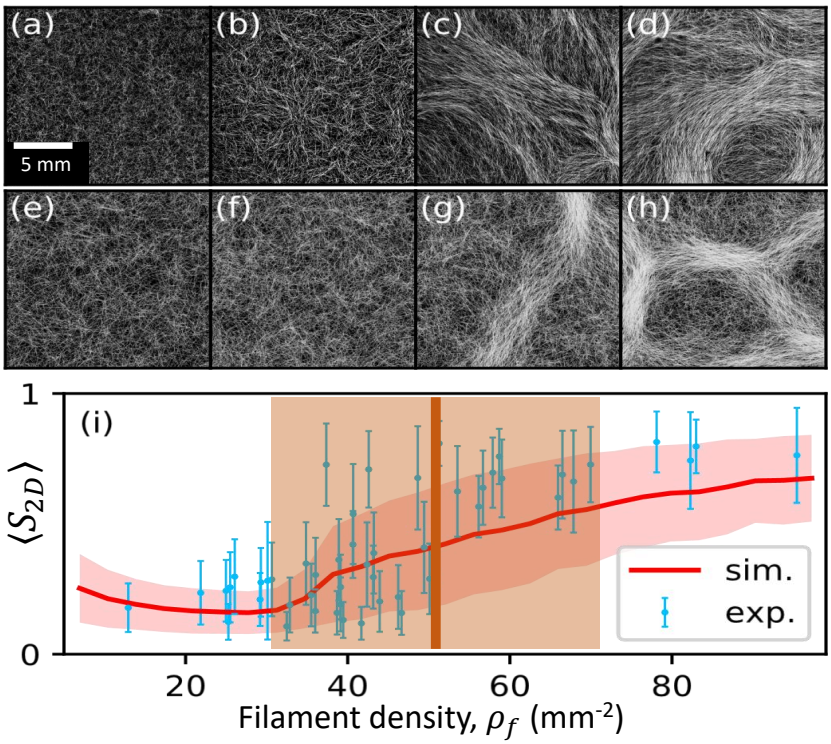

Figure 6.9: Phase transition in filamentous cyanobacteria. Experimental observations of the structure of filamentous cyanobacteria colonies at selected filament densities (a to d) compared with the structure of the filaments from simulations (e to h) at comparable densities. The nematic order of the filament structure at the frame size of 1 mm^2 is shown in panel (i). The dots and error bars for the experiments represent the average S_{2D} and the standard deviation respectively. Similarly, the solid line and the shaded region represent the average and the standard deviation for the simulations. The faint brown shaded area indicates the predicted region of phase transition from a disordered "gas" to an ordered state, based on a balance between the interaction and dissociation rates. Both experimental and simulation results show an ordering transition close to the expected value (vertical brown line). Adapted from [159].

profiles in Figure 6.10 as a shoulder at a length scale of about a centimetre. Above this scale, order drops, as the ROI averages over features with dissimilar orientation, whereas below this scale, the pattern order is relatively insensitive to d. Results from simulations, Figure 6.10(b), also show a similar characteristic length, further strengthening the predictions of the simple, yet powerful model.

Direct measurements of feature sizes were made by manually fitting a circle to the vortices or reticulate patterns shown in Figure 6.10(c)and (d) in ImageJ [85]. The average diameter of the features was found to be 8 ± 1 mm (mean ± SD), quite similar to results from both the

experiments and simulations in Figure 6.10(a-b). My collaborators have also shown how feature sizes vary with different parameters *e.g* the variation in filament curvature. Figure 6.10(e) shows that the size of the features l^* increases with the inverse of the standard deviation in filament curvature $1/\delta_\kappa \equiv v_0(D_\omega\tau)^{-1/2}$. From chapter 5, $1/\delta_\kappa \approx 3$ mm from the experiments, and the size of the features from experiments was found to be $\sim$4 mm (radius of vortices). This experimental result is also shown in Figure 6.10(e).

6.3.3 Ordering behaviour in naturally multiplying colonies

Up to this point, the experiments discussed have been those where the density was controlled manually, and the observation time was fixed to 72 hours after setting up a sample or colony. It has been observed that the critical density for self-organisation of *O. lutea* under these settings is about 50 filaments per mm^2. I wanted to understand if the ordering behaviour in a naturally multiplying colony is similar to the manually changed colony studied here. To do this, I prepared a very dilute suspension of filaments and poured it into a rectangular flask of base area $\approx$ 20 cm^2, with an initial filament density of about 5 filaments per mm^2. The flask was stored in the incubator described in section 2.3 and was taken out every 48 hours for imaging using a confocal laser microscope for a period of 40 days. Images were analysed for nematic order in the same way as the short-term experiments and the results in Figure 6.11 show that order emerges in a naturally growing cyanobacteria colony when the filament density is around 20 filaments per mm^2. It is interesting to note that the ordering in a naturally increasing *O. lutea* colony occurred in a similar way, but at a lower transition point, compared to the manually changed filament density, as shown in Figure 6.11.

Another difference between the two data sets is that in long-term experiments, the order of the filaments falls slightly at higher densities. There was no definitive explanation for the differences observed. However, I suspect the ageing of the colony and gradual buildup of *e.g.* extracellular polymeric substances (EPS) to be some of the factors since the main difference between the two experiments is the time of observation. Finally, the results from naturally growing colony were only possible in a single setting, owing to the continuous long-term observations

6.3.4 Topological defects in *O. lutea* colonies

In the self-organisation of elongated particles or filaments, such as liquid crystals, one of the key features is the formation of topological defects. These are effective singularities in the nematic director, where the order is undefined [195,196]. Topological defects are classified by the topological charge or the winding number which defines the number of rotations of the nematic

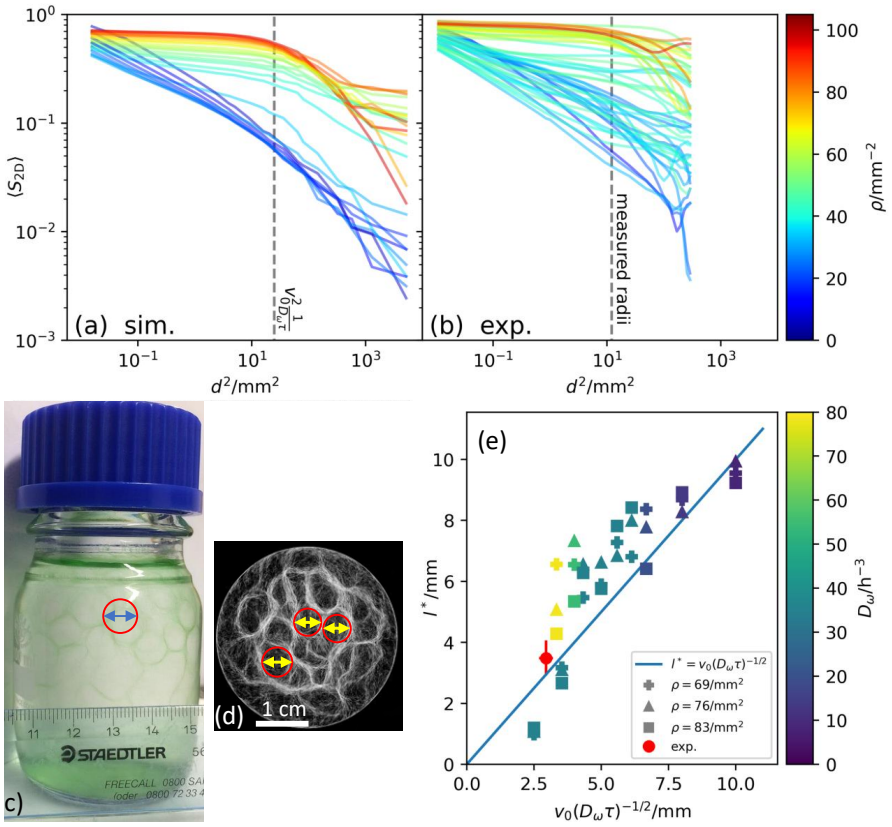

Figure 6.10: Size of structures in dense systems. (a) and (b) show log-log plots of the average nematic order parameter S_{2D} in experiments and simulations, respectively, calculated within regions of interest of size $d \times d$. At low density, the order parameter decays monotonically with d^2 indicating an isotropic state, whereas the emergence of structures at high density is marked by a plateau followed by a change in slope once d reaches the size of the emerging structures. The broken lines in (a) and (b) mark the radius of the structures in experiments and simulations, respectively. The size of the measured structures indeed coincides with the shoulder of the plateau. (c) and (d) show examples of reticulate patterns formed in a culture bottle and in a well plate, respectively, with sizes (some marked with red circles) similar to that captured by the plots in (a) and (b). (e) shows the size of the patterns l^* for different parameter values and the result from the experiments. All simulation results were provided by Jan Cammann. Adapted from [159].

director in any closed loop around the singular point [196]. Mathematically, the winding number is defined as

$$k = \frac{1}{2\pi} \oint (\theta - \theta_0) ds \tag{6.8}$$

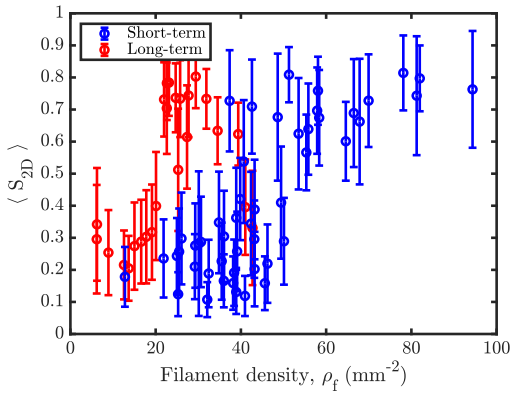

Figure 6.11: Comparing the ordering transition between long and short-term cyanobacteria colonies. The long-term colony was a self-replicating setup with observations made every two days on the same sample. The short-term setup consists of different samples and observations were made 72 hours after setup. The phase transition point for the long-term experiment is lower ($\sim$ 20 filaments per mm^{-2}) while that of short-term experiments is higher.

For example, moving along the red circle in an anticlockwise direction in Figure 6.12, the nematic director rotates through π radians, which gives a winding number or a defect charge of $+1/2$, according to Equation 6.8. Other examples of defects in liquid crystal are shown in Figure 6.13.

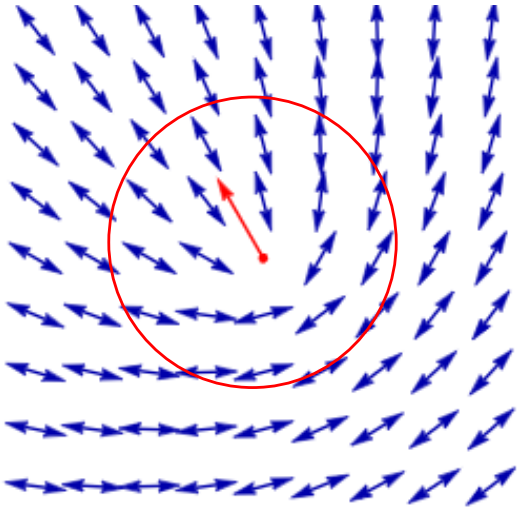

Figure 6.12: Classification of topological defect charge. The total rotation of the nematic director around any closed loop, like the red circle, is proportional to the charge, as in Equation 6.8. Here the angle of rotation is π giving $k = \pi/2\pi = +1/2$. Figure adapted from [196].

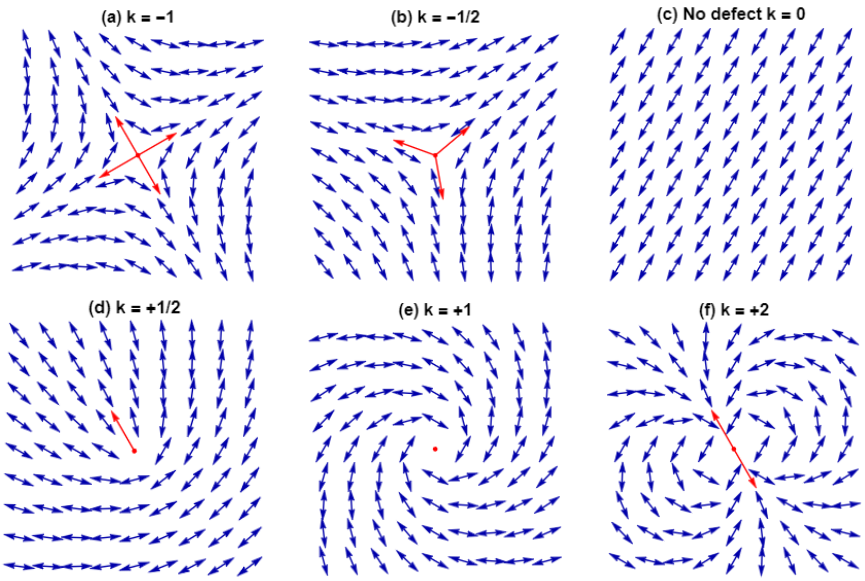

Figure 6.13: Examples of defects in a 2D nematic liquid crystal. Red arrows indicate the defect orientation. Figures adapted from [196].

Topological defects in active nematic systems are known to affect the dynamics of the system. For example, the emergence of $+1/2$ defects in a monolayer of epithelial cells was found to act as hotspots of compressive stress, leading to a higher probability of cell apoptosis (a normal and controlled cell death) and extrusion [197]. Furthermore, a study on the migration of a dense system of *Pseudomonas aeruginosa* on a surface found that the collision of comet-like defects slowed down fast-moving mutant cells as they rotated and got trapped [198]. On the other hand, wild-type cells avoided being trapped by moving slowly and migrating faster [198], suggesting that bacteria might have evolved mechanisms of moving in crowds while avoiding getting trapped.

In this work, I observed two kinds of topological defect charges, $+1/2$ and $-1/2$, from colonies of *O. lutea* in long-term experiments, as shown in Figure 6.14. Images of the filament structure taken days apart showed a slow movement of $+1/2$ defects, while $-1/2$ defects remained relatively stationary. An in-depth study of these defects is required for a better understanding of defect dynamics, for example, to investigate how the emergence of the topological defects affects the motion of filaments and if there is a correlation between their positions and the emergence of filament bundles.

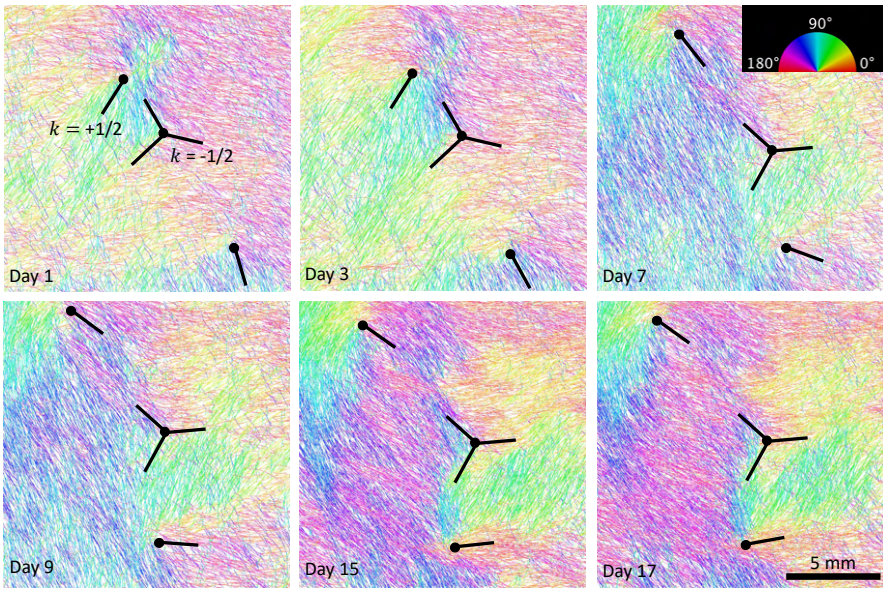

Figure 6.14: Defect formation in filamentous cyanobacteria structure. A series of images of a filamentous cyanobacteria (*O. lutea*) structure showing the evolution of defects. The orientations of filaments are marked by colour as indicated in the legend on the top right corner. $+1/2$ defects are shown by a line, and $-1/2$ defects as a threefold junction. Over several days the $+1/2$ defects move across the field of view, but the $-1/2$ defect remains relatively stationary.

6.4 Conclusion

In this chapter, the dynamics of self-organisation in filamentous cyanobacteria have been quantified. While focusing on one species of *O. lutea*, it was found that filaments self-organise into an ordered state when the density reaches some critical point around 40–50 filaments per mm^2, in colonies that were homogenised and stored for 72 hours. These results were also in agreement with a prediction of the ordering transition point based on the measured dynamical properties of individual filaments, which emphasized the balance between rates of interaction and rates of filament breakup.

However, it was also observed that when a single colony of filamentous cyanobacteria was grown from low to high density, which I called long-term experiments, the ordering transition point between the disordered "gas" phase and ordered state was around ≈ 20 filaments per mm^2, below that of short-term experiments. There was no definitive explanation for this difference but I suspect that the ageing of the colony could influence the interactions of the filaments, for example, due to the buildup of extracellular substances. More studies would be required for long-term experiments to find out exactly what encourages filaments to order so quickly.

Within the chapter, a simple numerical model of self-organisation of filamentous cyanobacteria, designed by my collaborators, was briefly introduced. By focusing on nematic interactions of the filaments as observed in my experiments, the model was able to capture strikingly resembling patterns in the structure of the cyanobacteria colonies. These results proved that although the dynamics of the filamentous cyanobacteria are complicated, the key collective behaviours can be described by a simple model, informed in all respects by experimentally motivated parameters.

Beyond the transition point from disorder to order, filamentous cyanobacteria form patterns characterised by polygon-like structures, also called reticulate patterns. The sizes of these structures were measured by looking at the correlation of filament order and by manual measurement of their diameters. The analysis of data from both the experiments and simulations showed that the size of these structures was about 1 cm which was supported by physical observations.

Finally, just as in liquid crystals, the nematic or polar interactions of filamentous cyanobacteria cultured for a long period of time gives rise to the emergence of nematic topological defects, mainly the $+1/2$ and $-1/2$ topological charges. The study of topological defects was not intensive, due to the limited data and time constraints to repeat the long-term experiments. Further studies would therefore be needed to understand the dynamics of topological defects in filamentous cyanobacteria colonies.

The study of self-organisation of filamentous cyanobacteria could have applications in the design of artificial active filaments and in other applications such as the design of biofuel cells [58, 59].

Chapter 7

Cyanobacteria self-organisation in confinement

7.1 Introduction

The ubiquity of cyanobacteria comes with the ability of these microorganisms to adapt to different environments [199]. For example, filamentous cyanobacteria have been found to thrive in confined spaces such as the pores of rocks [200–202]. The invasion of microorganisms in rock sculptures causes cosmetic, chemical as well as mechanical damage [53]. Understanding the formation of biofilms in confined spaces could help in the control of biofouling of porous structures.

One of the industrial applications of cyanobacteria is the production of biofuel, which involves the growth of cyanobacteria in specialised fuel cells that turn light energy into bioethanol [203]. To achieve maximum photosynthetic efficiency, cyanobacteria require enough exposure to light [204]. However, self-shading of filaments in dense biofilms limits light exposure to other filaments in the biofilm, thereby reducing the efficiency of bioreactors [205]. Therefore, one way of maximising the efficiency of these fuel cells is to increase light exposure by, for example, limiting the thickness of the biofilm layer. However, there is a need to understand how such confinement would affect the collective structure of cyanobacteria. This is what this chapter tries to explore. The study of cyanobacteria in confinement could therefore help in the design of more efficient biofuel cells of the future.

This chapter will highlight the experimental work I have carried out in order to understand the distribution and collective structure of filamentous cyanobacteria in confined spaces. The work presented here is intended to be matched by numerical analysis from my collaborators in Loughborough, which will follow after the submission of this thesis. The major question that I am trying to answer here is: how does the size or geometry of confinement affect the distribution and collective structure of filamentous cyanobacteria? To answer it I designed and fabricated microfluidic chambers of four different geometries, as described in the next section. This introduces a new length scale, and I explore examples of strong and weak confinement, where this

scale is smaller or larger than the average filament size, respectively. Each confinement geometry had chambers of varying sizes to explore the effect of the size of confinement on the filamentous cyanobacteria collective structure and distribution. Similarly, the four different geometries will help to explore how cyanobacteria filament structure and distribution can be affected by the shape of the confinement. As in the preceding chapters, the focus here will be on one species of filamentous cyanobacteria, *Oscillatoria lutea*, one of the more well-studied cyanobacteria species.

7.2 Methodology

In order to study the structure formation of filamentous cyanobacteria in confinement, I designed a microfluidic device around four different types of confining shapes, each with varying sizes, as shown in Figure 7.1. The dimensions of the chambers ranged between 3 mm and 15 mm in diameter for the circular chambers and all other shapes had similar dimensions (side lengths were matched with the diameter of a corresponding circular chamber). The choice of the minimum chamber size was influenced by the lengths of the filaments, which ranged between 1 mm and 3 mm, with a mean size of 1.5 mm as shown in chapter 6.

On the other hand, the choice of the maximum chamber size was motivated by the size of the vortices observed in the study of filamentous cyanobacteria self-organisation, in chapter 6. The diameters of the vortices were typically around 6 mm. Therefore, the idea was to have confinement chambers that could at least hold one or two vortices, if they can form in confinement. For this reason, the maximum size of the chamber size was set to 1.5 cm. On practical limitations, I wanted uniformity in height across all chambers. The easiest way to achieve this was to make all PDMS chips from the same master mould. Therefore, the choice of chamber sizes in my experiments allowed all the designs to be made from a single wafer 10 cm in diameter. Another potential limitation of the chamber sizes is the need to avoid the collapse of wider chambers due to self-loading. This was not a concern in my designs as the expected deflection of the largest chambers due to self-loading in the air [206] was found to be $\ll 1$ μm for a chamber width of 1.5 cm. The deflection should be much lower for a PDMS chip submerged in water, as was the case in these experiments.

As described in chapter 2, the designs were made in QCAD software [61] and were sent to JD Photodata which manufactured a photomask. The photomask was used to fabricate a master mould using photolithography, as described in section 2.1.1. The height of the raised surfaces on the wafer was 39.1 ± 0.6 μm, as measured by OCT (see section 2.1.3). The master mould was then used to make PDMS chips using the soft lithography method given in section 2.1.2.

To fabricate the complete microfluidic device, the PDMS chip was first perforated to allow for

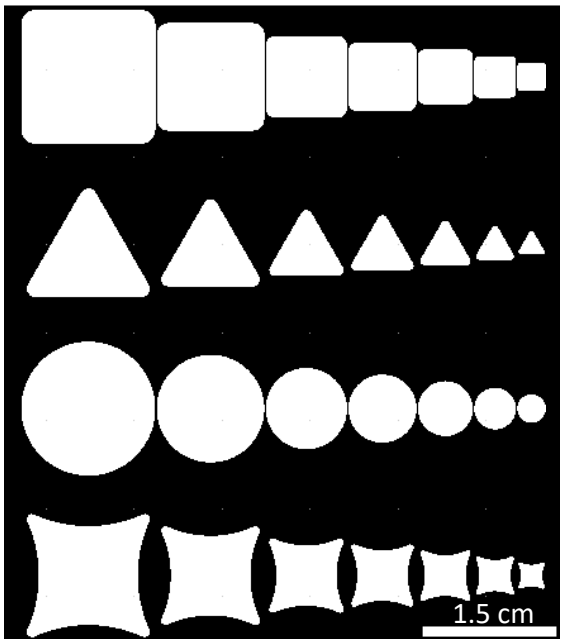

Figure 7.1: A snapshot of confinement design in QCAD software. The white areas were the regions that became transparent on the photomask. This allowed light to go through and cross-link the SU-8 to form raised surfaces on the master mould. PDMS chips made out of the master mould then had channels of the regions on the master mould with raised surfaces. See sections 2.1.1 and 2.1.2 for the photolithography techniques employed.

easy diffusion of nutrients and gases in and out of the chambers, while restricting the movement of filaments out of the confinement. The perforation was done using a 500 μm diameter puncher, often described as a "biopsy punch", as shown in Figure 7.2(b). This hand-operated device was used to punch 500 μm wide holes about 1 mm apart across the whole area of the chamber, as shown in Figure 7.2. The perforated PDMS chips were then primed in an oxygen plasma cleaner alongside the base (a PDMS-coated well plate prepared as the PDMS chip, see chapter 2 for details), to activate the surface for bonding. The primed PDMS chip and the base were then bonded together by applying light pressure while avoiding contact between the walls of the chambers and the substrate. This formed a complete microfluidic device, ready for experimental use.

A solution of the culture media was then added to the well plate containing the microfluidic device until the PDMS chip was completely submerged. The well plate was then placed in a vacuum chamber for about 10 minutes to displace air out of the chambers, leaving the chambers filled with culture media. The well plate was then taken out of the vacuum chamber and a shaken suspension of filamentous cyanobacteria was added to each confinement chamber using

a 0.5 ml syringe fitted with a needle with a diameter of 400 μm. The well plate containing the confinement chambers was covered and placed in an incubator before imaging. An example of a complete device with cyanobacteria inside is shown in Figure 7.2.

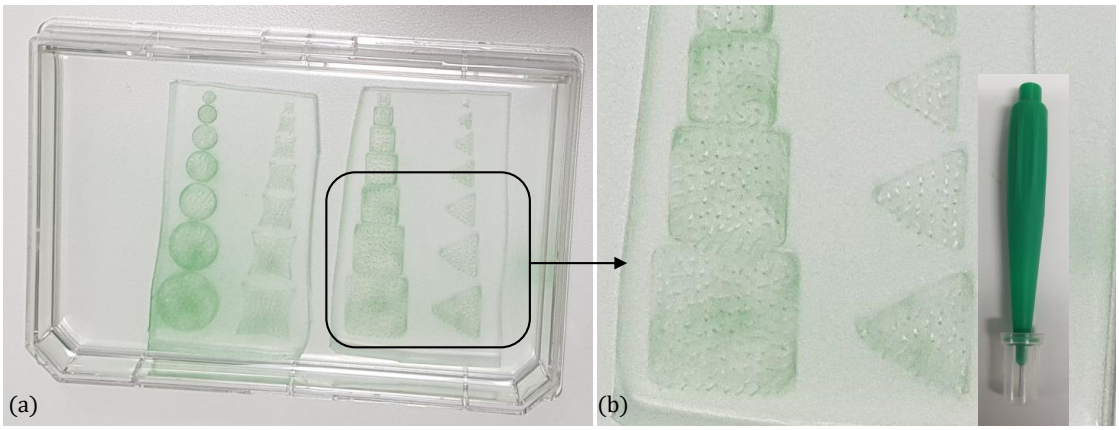

Figure 7.2: Filamentous cyanobacteria in confinement chambers. (a) Completed microfluidic device with confinement chambers loaded with filamentous cyanobacteria (*O. lutea*). The confinement chambers were all submerged in culture media throughout the experiments to avoid drying out of the samples. (b) The chambers were perforated by a PDMS puncher shown on the right for easy diffusion of nutrients and gases.

The experiment was carried out in two different ways, which depended on how the samples were stored. In the first experiment, a very dilute suspension of filaments was added to the chambers and the chips were stored for 25 days while imaging the samples every 48 hours using a confocal laser scanning microscope (Leica TCS SP5). This allowed the investigation of the structure formation of filamentous cyanobacteria in confinement, where the density changed through the natural growth of the biofilm. I called this a long-term experiment, consistent with the naming in the previous chapter. The second experiment involved changing the density of the filaments manually by sucking samples out of the chambers using a syringe before loading new samples. Every setup was imaged after 72 hours using a confocal laser scanning microscope (Leica TCS SP5), and then the chip was available to be emptied and reused. As in chapter 6, I called this experiment a short-term experiment.

The loading of fresh samples helped to avoid the possible effects of ageing on structure formation such as a gradual buildup of extracellular polymeric substances (EPS) and the creation of nutrient concentration gradients. For example, for long-term storage of cyanobacteria in chambers, the concentration of nutrients inside the chambers could go down with time, thereby

creating a chemical or nutrient gradient. Such gradients may influence the behaviour of the filaments in the chambers by, for example, causing them to accumulate around the perforations, as I observed in a preliminary version of this experimental setup. Before deciding to drill uniformly distributed and closely spaced holes, I had prepared confinement chambers with just four holes, but cyanobacteria filaments accumulated at the holes, which I believe was triggered by nutrient or oxygen gradients. To solve this problem, I drilled the holes as close as possible with a spacing of about 1 mm and saw that the filaments did not accumulate around the holes anymore, but rather spread out throughout the chamber.

7.3 Results

7.3.1 Filaments accumulate at the walls in circular confinement

In section 5.3.2 it was noted that isolated *O. lutea* filaments like to stick to straight boundaries, hugging the walls for an average distance of about 500 μm before separating again. Again, in section 3.3.3, it was found that these filaments have a preferred curvature of 0.5 mm^{-1} when they glide in isolation. If multiple filaments in confined chambers were to behave as they do in isolation, and when individually interacting with walls, then I would expect to see filaments confined to walls more when the radius of confinement for circular chambers is less than 2 mm, equivalent to the lower bound of the measured radius of filament curvature in chapter 3. The circular chambers in these experiments had radii of 1.5, 2.25, 3, 3.75, 4.5, 6, and 7.5 mm. I hypothesised that filaments in the first two chambers would find it difficult to escape the walls, thereby spending their time gliding along the walls. Filaments would then find it easy to escape the boundaries and move between the walls and the central part of the chambers with a larger radius than the observed radius of filament curvature.

Results from section 5.3.3 indicated that individual cyanobacteria filaments lose their preferred curvature when they interact with other filaments, thereby becoming more straight. This behaviour, therefore, suggests that filaments in dense colonies could still be trapped along the boundaries of the circular chambers even if the radius of the chamber was larger than the observed radius of filament curvature of the isolated filaments. Indeed, this is what was observed in my experiments, as shown in Figure 7.3. Here, the density of the filaments is higher along the boundaries than at any other point in the chamber, for all the chamber sizes. In other words, there is a significant wall-hugging effect seen in all cases.

To quantify the distribution of filaments inside the circular chambers, I calculated the density of filaments at the pixel level, by computing the ratio of white pixels to the total number of pixels

within a neighbourhood of 30 × 30 pixels. For filaments with a width of 2 pixels, a ratio of 1 corresponded to about 15 filaments per 8100 μm^2. The average filament density within the chamber was also computed by calculating the ratio of all the white pixels within the chamber to the total number of pixels in the chamber. The average density was presented in filaments per mm^2 as shown in Figure 7.3. It is noted that these density computations underestimate the density of filaments where there are crossings and overlay of filaments but represent a reasonable measure of the densities.

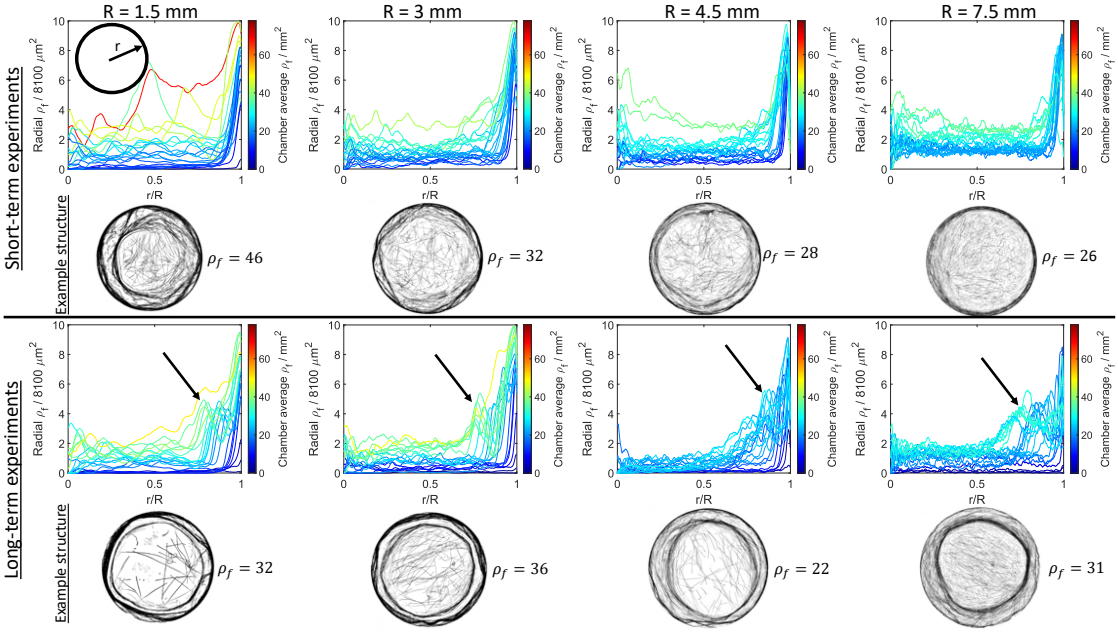

Figure 7.3: Wall hugging effect of *O. lutea* in confinement. The density of filaments near the boundaries is higher than in the interior of the chamber. Top rows: Graphs of radially averaged, filament density against position along the radius of the chamber in short-term experiments show that the density of the filaments is highest near the walls, even for larger confinement chambers. The selected graphs are for circular chamber radii of 1.5, 3, 4.5, and 7.5 mm, as indicated on top of the figure. Below the graphs are example images of the filament structure in respective confinement sizes. Bottom rows: similar analysis but for long-term experiments. Here, at higher chamber filament densities a ring forms as shown by insert images and as pointed by the arrow in the plots. Also, there is a clear phase separation between the centre of the chamber and the regions near the boundaries. Similar can be seen in the short-term experiments, but they were not as distinct.

One interesting observation from the results in Figure 7.3 is the phase separation generated

at higher filament densities. Here, especially in long-term experiments, I see the formation of a bundle of filaments near but noticeably away from the walls. I also observed a nematic ordering of filaments at the centre of the chamber, which later forced the filaments ringing the chamber into a deformed shape (see Figure 7.4), topology similar to that seen in confined microtubules [207]. It would be interesting to see if such results would be replicated by a simple numerical model, like what my collaborators have done with the open-space experiments in the previous chapter.

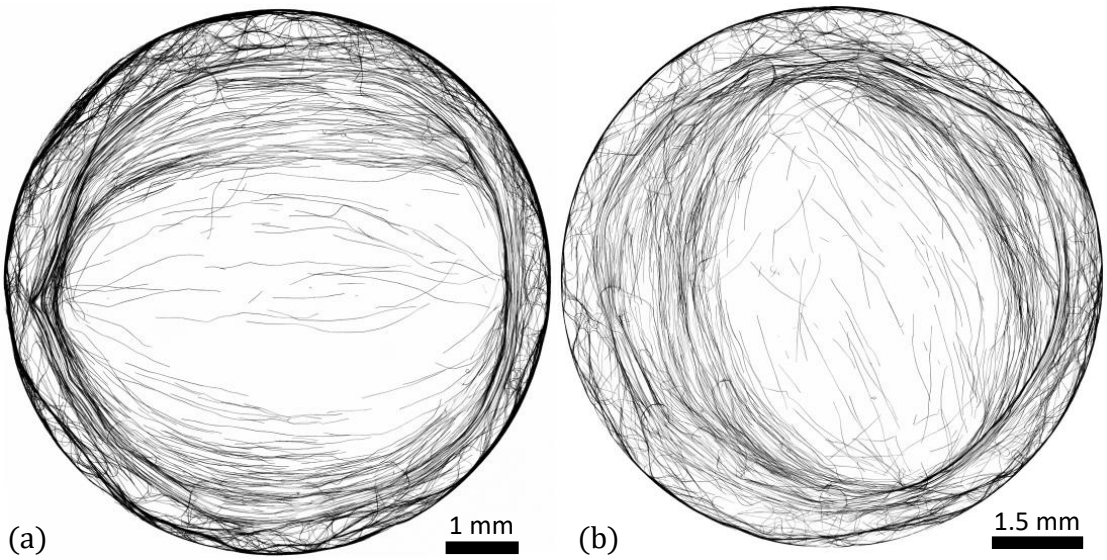

Figure 7.4: Depletion and ordering of filaments at the centre of a circular confinement. The ordering of the filaments around the centre of the chamber at high densities forces the ring into a deformed shape. Similar topology has been observed in confined microtubules [207].

7.3.2 Filament structure in other confinement geometries

As highlighted in section 7.2, the study of filamentous cyanobacteria structure formation in confinement was carried out in four different geometries, namely circular, square, triangular, and negative curvature chambers, as shown in Figure 7.5. The experiments in all the geometries were carried out in the same way i.e. long-term experiments where filaments were grown in chambers for 40 days while imaging the structure every 48 hours and short-term experiments where the filaments were stored for 72 hours before imaging the structure formed and then being emptied out for further experiments. There were 21 observations for each chamber size in the short-term experiments, with varying filament densities. Here, I will highlight key the qualitative differences observed in the structures formed in these four geometries. As shown in Figure 7.5, both the

circular and square confinements have a clear spatial variation of filament density, with more filaments seen closer to the walls than at the centre of the chamber. In both cases of confinement, the walls effectively capture the cyanobacteria filaments. The formation of the bundles near the walls could also be a result of the clogging of the filaments. However, in triangular and negative curvature confinements, the structure is different, as the distribution of filaments there is fairly uniform. More especially in the triangular confinement, filaments look almost evenly distributed. A more quantitative analysis of these structures could be developed alongside some numerical studies of the same phenomena together with my collaborators in Loughborough as future work.

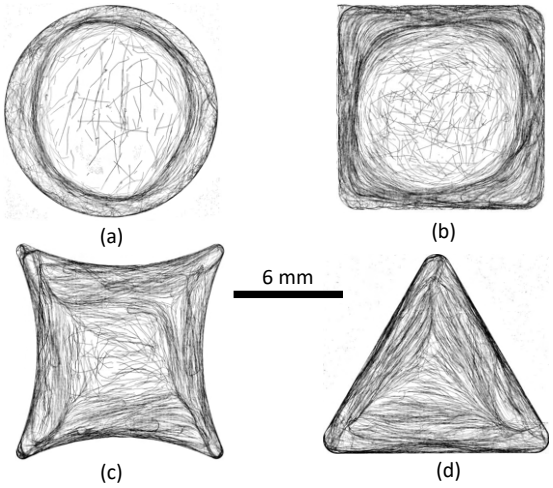

Figure 7.5: Comparing filament structure formation in four different confinement geometries. In (a) and (b), more filaments are seen close to the walls than at the centre of the chamber, suggesting that confinement walls of these shapes are good at capturing filaments or promoting clogging of the filaments. There is also clear phase separation between a sparse internal phase of filaments, and the dense wall-bound filaments in these two shapes. In (c) and (d), filamentous cyanobacteria filaments are fairly evenly distributed, which suggests that the walls of these shapes either repel the filament or do not influence clogging near the walls.

7.4 Conclusion

In conclusion, this chapter highlighted some of the observations of the structure formation of *O. lutea* in confinement. It was noted that some geometries force filaments to spend more time closer to the walls than others. For example, in circular confinement, there was a higher density of filaments near the walls than at the centre of the chamber. This generated a phase separation

between a sparse internal phase of filaments and a denser condensation of wall-bound filaments or the formation of a bundle of filaments near but slightly removed from the walls. The accumulation of the filaments near the walls and the formation of a bundle of filaments near the walls of the circular confinements could also be due to the clogging of the filaments that might be influenced by the nature of the walls. The distribution of filaments in square confinements was similar to that of circular confinements. However, in triangular and negative curvature confinements, filaments were distributed almost evenly inside the chambers.

Therefore, through this simple qualitative analysis, the results have indicated that the shape and shape of the confinement do affect the structure formed by filamentous cyanobacteria. Results from this study could be used in the design of micro-biofuel cells [58, 59, 208–210] especially those aimed at ensuring uniform distribution of filaments across the chamber. In this regard, one would design microchannels with either negative curvature or sharper internal boundaries.

The results presented in this chapter were limited as the analysis of the data is still underway and may continue beyond this thesis in the context of the studies of my collaborators at Loughborough. From the comprehensive data collected from this study, more questions could be answered later on. For example, one could want to understand how the size of the confinement affects structure formation and generation of phase separation. Also, at low densities, the distribution of filaments in the circular and square confinements was fairly uniform hence one could also want to understand the critical density at which the phase separation occurs and how that changes with confinement size. Such questions could be answered with further analysis of the data collected, or with more experiments conducted.

Chapter 8

Summary and Outlook

This thesis has revealed a number of fascinating behaviours of filamentous cyanobacteria from the single filament to collective interactions. In line with the goals of the project, these behaviours have been quantified in different ways, revealing information which lays the groundwork for further lines of investigation of filamentous cyanobacteria as active polymers. Here, I will present the main new results from this thesis and explain the relevance of these results, both scientifically and in practice. I will then conclude with some of the research questions that could be investigated in the future.

8.1 Summary

8.1.1 Structural and mechanical properties of filamentous cyanobacteria

In chapter 2 the mechanical properties of three related species of filamentous cyanobacteria, namely *K. animale*, *L. lagerheimii*, and *O. lutea* were quantified. These species all belong to the order *Oscillatoriales* and are of similar size and motile behaviour. This allowed for robust validation of the internal consistency of my methods. I found that the mechanical responses of all three species were similar to each other. The average bending stiffness ranged between 2.6–6.0$\times 10^{-17}$ N m^2, as measured by monitoring the bending of filaments under fluid flow in a custom-built microfluidic flow cell. These observations were complemented by measurements of the elastic modulus of the cell wall, through AFM techniques, and by measurements of the thickness of the cell wall and its component layers, through TEM. By comparing the bending stiffness to that expected from a hollow rigid cylinder, I showed that the resistance of filamentous cyanobacteria to bending is largely due to the mechanical stiffness of their characteristically thick cell walls.

These results were consistent with parallel measurements using a different method by my collaborators at the Max Planck Institute for Dynamics and Self-organisation (MPIDS) [142]. The bending stiffness of filamentous cyanobacteria can be used to predict the variation of its shape

under known forces and for modelling its behaviour and collective organisation, as demonstrated by Ref [47]. It can also be used for the design of porous biofuel cells similar to those described in [96, 97] that trap filaments while allowing the exchange of gases and nutrients between the system and its surrounding.

Also in this chapter, it was demonstrated that isolated gliding cyanobacteria filaments take on a well-defined circular shape. I measured the curvature of the gliding filaments by fitting a circle to their shapes and found that, on average, the curvature of the filaments is about 0.5 mm^{-1}. On the other hand, inactive cyanobacteria filaments, whose motion was halted by reducing the temperature of their environment, were found to have irregular shapes, suggesting that the smooth curvature of their natural state arises from the active forces within the filaments.

Finally, by considering one of the theories of the gliding motion of filamentous cyanobacteria, which suggests that compressional forces in the fibril layer generate travelling waves that propel the filament in the opposite direction [41, 42], I estimated the range of forces that could be generated, based on the local curvature of the filaments. I, therefore, computed the maximum axial stress in the cell wall of the filament and found values in the order of tens of kPa which appear to be actively maintained by an internal distribution of forces as the bacteria move. These results provide further insights into the understanding of the mechanical properties of filamentous behaviour which could help uncover the exact mechanisms behind their gliding motion. The majority of the work described in this chapter is published in Ref. [91].

8.1.2 Isolated cyanobacteria filaments motion

In chapter 4, I investigated the behaviour of isolated cyanobacteria filaments. The goal was to identify features that are critical for modelling the behaviour of cyanobacteria filaments. Here, I studied filaments gliding in isolation on the base of large well plates. Dynamic properties of the filaments, such as the speed, angular drift rate, filament curvature, the curvature of the path traced by the filament and the reversal frequency were quantified. I focused on one of the three species studied in chapter 3, to ensure the depth of analysis.

Key results from this chapter were that *O. lutea* filaments tend to move in a clockwise motion when they are in isolation and not disturbed by obstacles or boundaries. The speed of their gliding motion was found to be $3.0 \pm 0.7 \mu m\ s^{-1}$, while the curvature of the path varied with time. The curvature of the filaments was similar to the instantaneous curvature of the path they traced. Filamentous cyanobacteria are known for reversing their direction of motion [168, 172] and the reversal frequency was analysed here by measuring the time between reversals. I observed 140 reversals during the combined 29 h of observations, representing an average of one reversal every

12 minutes. Due to their preference for clockwise motion, *O. lutea* filaments maintained this type of motion even after reversing their motion, rapidly readjusting their configuration to match their curvature prior to reversing.

The results from this chapter can be used as building blocks for models of gliding motion or collective behaviour of filamentous cyanobacteria, although some of the observed behaviours, in particular the preferred filament curvature, were later found to change with filament density or collective interaction, as found in chapter 5.

8.1.3 Collective interaction between filaments.

In chapter 5, the collective behaviours of *O. lutea* filaments were quantified. First, I looked at how likely cyanobacteria filaments were to align with one another when they meet while gliding on a substrate. Here, I observed a total of 400 interactions between filaments, and only 16 of these resulted in alignment or anti-alignment of the filament motion. This represented a probability of pairing up of only 0.04. The rest of the interactions saw filaments ignoring one another. This behaviour is similar to other active polymers like microtubules [167] but shows a much weaker level of interaction.

Focusing on the filament interaction events that lead to alignment, I measured the distance through which the filaments travelled while aligned, which was found to be 427 ± 197 μm (mean $\pm$ SD). From the alignment distance, I was able to estimate the breakup rate of pairs or bundles which was found to be 0.007 ± 0.004 s^{-1} (mean $\pm$ SD), representing a survival time of ~ 142 seconds. The breakup rate of the filaments was later used to predict the critical point for the phase transition between a disordered "gas" colony of filamentous cyanobacteria and the well-ordered state, in chapter 6.

I also investigated how filaments behaved when they interact with walls or boundaries. Here, I measured the length over which cyanobacteria filaments glided along the walls after the collision. It was found that, on average, filaments glided along the walls for a length of ~ 500 μm after aligning. This distance was used to calculate the dissociation rate of filaments from the walls and I estimated that, on average, filaments detach from walls at the rate of 0.006 ± 0.003 s^{-1} (mean $\pm$ SD), representing a survival time of ~ 167 seconds. These results were similar to the breakup rate of filaments in pairs or bundles.

Also, in chapters 3 and 4 it was found that cyanobacteria filaments maintained a circular shape as they glided on a substrate. However, this behaviour diminished with an increase in filament density or rate of interactions, as observed in chapter 5. There, I measured the curvature of filaments in colonies of cyanobacteria with different filament densities and found that the

mean curvature decreased with an increase in filament density. Indeed, physical observations in higher-density structures showed that the filaments had generally lost their curvatures and their preference for clockwise over counter-clockwise motion above densities of only $\sim$ 10 filaments per mm^2. The distribution of the measured curvatures in dense systems showed a peak around zero and this led to the modification of the numerical model developed by my collaborators in Loughborough, where the preferred circular shape was dropped and a straight equilibrium filament configuration was used.

8.1.4 Collective organisation in filamentous cyanobacteria

Having identified and quantified the key behavioural aspects of cyanobacteria filaments both in isolation and collectively, the next step was to observe how collective interaction leads to structure formation. In chapter 6 I studied the structure formed by filamentous cyanobacteria (*O. lutea*) in an open space by choosing an area in the middle of a well plate whose filaments' behaviour was less likely affected by the far boundaries. I measured the orientational order of the filaments in the central region of the plates in colonies with densities between about 1 and 100 filaments per mm^2 and found that the colony structure changes from a disordered "gas" to an ordered nematic phase at densities between 40 and 55 filaments per mm^2.

The conditions of the observed phase transition were in agreement with the predicted value of a critical density of about 52 filaments per mm^2, which corresponds to a density when the rate of structure formation from interactions should exceed the rate at which order is lost by the breakup of bundles. Furthermore, results from a simple numerical model using the parameters measured in this thesis agreed with experimental observations. Various measurable parameters, such as the size of the vortices in the collective structure, matched well between the experiments and the simulations. For example, both the experiments and simulations showed that the sizes of the vortices formed by filamentous cyanobacteria were about 1 cm in diameter. These results were considerably advanced compared with previous studies [47]. The results from this chapter tell us that the collective behaviour of cyanobacteria filaments could be predicted accurately by a simple numerical model informed directly by the individual and pairwise interactions of the bacteria directly measured under the microscope.

8.1.5 Cyanobacteria in confinement.

In chapter 7, preliminary results on the study of filamentous cyanobacteria in confinement were presented. Unlike in chapter 6, where filaments were free to move in and out of the region of interest, here the filaments were restricted to confinement chambers of four different geometries;

circular, square, triangular and negative curvature.

The circular and square confinements forced more filaments to glide near the walls than the middle part of the chamber. This differential filament density created a phase separation where the region at the centre of these chamber shapes was sparsely populated but with filaments that tended to still be well-aligned with each other, locally. In contrast, the region near the walls was densely populated, forming a ring around the edge of the confinement chamber.

In triangular and negative curvature confinements, filaments were fairly evenly distributed inside the chamber, at densities comparable to those that resulted in phase separation in circular and square confinements. The conclusion here was that geometry affects cyanobacteria colony growth patterns, and different confinement chambers can be used to achieve certain preferred distributions of filaments in chambers. For example, when designing micro-biofuel cells [208–210] as in [211] but using filamentous cyanobacteria, with the goal of ensuring uniform distribution of the filaments, triangular or negative curvature confinement may be preferable. Uniform distributions of filaments in such chambers would reduce self-shading [205] thereby improving light exposure and photosynthetic efficiency of biofuel cells.

8.2 Future outlook

This thesis has presented some interesting results on the mechanics, behaviour, order and self-organisation of filamentous cyanobacteria. While the research has been extensive, there are still some research questions to be answered. For example, in chapter 3 the structural and mechanical properties of filamentous cyanobacteria were measured and these were connected with the forces that the filaments would generate leading to their gliding motion. However, gliding motion in filamentous cyanobacteria is still not fully understood. Further research is required to have a solid understanding of how filamentous cyanobacteria achieve gliding motion.

In chapter 4, I looked at the behaviour of isolated *O. lutea* filaments and found that their speed is oscillatory in nature on a timescale that is long compared to e.g. filament rotation. One biological question that could be asked is why they move in such a manner.

While investigating structure formation in chapter 6, I noted the formation of topological defects but I did not study them fully, due to limited data and time. It could be interesting to see if the topological defects formed by filamentous cyanobacteria have similar properties to those that are formed by liquid crystals [212, 213] or microtubules [214].

Finally, in confinement studies, the confinement chambers in this thesis only varied in width while the height remained constant. It would be interesting to see how varying chamber height would affect the distribution of filaments. The data gathered also has the potential for more

detailed analysis.

Bibliography

[1] J William Schopf and Bonnie M Packer. Early Archean (3.3-billion to 3.5-billion-year-old) microfossils from Warrawoona Group, Australia. *Science*, 237(4810):70–73, 1987.

[2] Abigail C Allwood, Malcolm R Walter, Balz S Kamber, Craig P Marshall, and Ian W Burch. Stromatolite reef from the Early Archaean era of Australia. *Nature*, 441:714–718, 2006.

[3] Birger Rasmussen, Ian R Fletcher, Jochen J Brocks, and Matt R Kilburn. Reassessing the first appearance of eukaryotes and cyanobacteria. *Nature*, 455(7216):1101–1104, 2008.

[4] Kaarina Sivonen. Cyanobacterial Toxins. In Moselio Schaechter, editor, *Encyclopedia of Microbiology (Third Edition)*, pages 290–307. Academic Press, Oxford, 2009.

[5] Timothy W Lyons, Christopher T Reinhard, and Noah J Planavsky. The rise of oxygen in Earth's early ocean and atmosphere. *Nature*, 506(7488):307–315, 2014.

[6] MR Walter, J Bauld, and TD Brock. Microbiology and morphogenesis of columnar stromatolites (*Conophyton, Vacerrilla*) from hot springs in Yellowstone National Park. In MR Walter, editor, *Stromatolites*, volume 20 of *Developments in Sedimentology*, pages 273–310. Elsevier, 1976.

[7] B Jones, RW Renaut, MR Rosen, and KM Ansdell. Coniform stromatolites from geothermal systems, North Island, New Zealand. *Palaios*, 17:84–103, 2002.

[8] Robert Wharton, Bruce Parker, and George Simmons. Distribution, species composition and morphology of algal mats in Antarctic Dry Valley lakes. *Phycologia*, 22:355–365, 12 1983.

[9] SM Awramik, L Margulis, and ES Barghoorn. Evolutionary processes in the formation of stromatolites. In *Developments in Sedimentology*, volume 20, pages 149–162. Elsevier, 1976.

[10] AM Mccgregor. A pre-Cambrian algal limestone in Southern Rhodesia. *South African Journal of Geology*, 43(01):9–15, 1940.

[11] Phillip Elliott Playford, Anthony Edward Cockbain, PF Berry, Anthony P Robderts, Peter W Haines, and Brendan Brooke. *The Geology of Shark Bay*, volume 281. Geological Survey of Western Australia Bulletin 146, 2013.

[12] EP Suosaari, RP Reid, PE Playford, JS Foster, JF Stolz, G Casaburi, PD Hagan, V Chirayath, IG Macintyre, NJ Planavsky, et al. New multi-scale perspectives on the stromatolites of Shark Bay, Western Australia. *Scientific reports*, 6(1):1–13, 2016.

[13] Stanley M Awramik. The history and significance of stromatolites. In *Early organic evolution*, pages 435–449. Springer, 1992.

[14] Marie Lochman. Close up of Stromatolites at Hamelin Pool. `https://www.bushheritage.org.au/species/stromatolites`. Accessed: 03-10-2022.

[15] Michelle L Liberton and Himadri B Pakrasi. Membrane systems in cyanobacteria. Technical report, Pacific Northwest National Lab.(PNNL), Richland, WA (United States), 2008.

[16] Yasukazu Nakamura, Takakazu Kaneko, Shusei Sato, Mamoru Mimuro, Hideaki Miyashita, Tohru Tsuchiya, Shigemi Sasamoto, Akiko Watanabe, Kumiko Kawashima, Yoshie Kishida, Chiaki Kiyokawa, Mitsuyo Kohara, Midori Matsumoto, Ai Matsuno, Naomi Nakazaki, Sayaka Shimpo, Chie Takeuchi, Manabu Yamada, and Satoshi Tabata. Complete Genome Structure of Gloeobacter violaceus PCC 7421, a Cyanobacterium that Lacks Thylakoids . *DNA Research*, 10(4):137–145, 08 2003.

[17] Jimmy HW Saw, Michael Schatz, Mark V Brown, Dennis D Kunkel, Jamie S Foster, Harry Shick, Stephanie Christensen, Shaobin Hou, Xuehua Wan, and Stuart P Donachie. Cultivation and complete genome sequencing of Gloeobacter kilaueensis sp. nov., from a lava cave in Kīlauea Caldera, Hawai'i. *PloS one*, 8(10):e76376, 2013.

[18] John Cumbers and Lynn J Rothschild. Salt tolerance and polyphyly in the cyanobacterium Chroococcidiopsis (Pleurocapsales). *Journal of Phycology*, 50(3):472–482, 2014.

[19] Claudia Mosca, Lynn J Rothschild, Alessandro Napoli, Fabrizio Ferré, Marco Pietrosanto, Claudia Fagliarone, Mickael Baqué, Elke Rabbow, Petra Rettberg, and Daniela Billi. Overexpression of UV-damage DNA repair genes and ribonucleic acid persistence contribute to the resilience of dried biofilms of the desert cyanobacetrium Chroococcidiopsis exposed to Mars-like UV flux and long-term desiccation. *Frontiers in Microbiology*, 10:2312, 2019.

[20] Pia Lindberg, Peter Lindblad, and Laurent Cournac. Gas Exchange in the Filamentous Cyanobacterium Nostoc punctiforme Strain ATCC 29133 and Its Hydrogenase-Deficient Mutant Strain NHM5. *Applied and environmental microbiology*, 70:2137–45, 05 2004.

[21] Maike Lorenz, Thomas Friedl, and T Darienko. SAG: Catalogue of Algal Strains. `https://creativecommons.org/licenses/by-sa/4.0/`. Accessed: 2022-07-08.

[22] C Sili, Giuseppe Torzillo, and Avigad Vonshak. Arthrospira (Spirulina). *Ecology of Cyanobacteria II: Their Diversity in Space and Time*, pages 677–705, 07 2013.

[23] MRJ Salton and KS Kim. Structure. In S Baron, editor, *Medical Microbiology*. University of Texas Medical Branch at Galveston, Texas, 2018.

[24] Katia Sciuto and Isabella Moro. Cyanobacteria: the bright and dark sides of a charming group. *Biodiversity and Conservation*, 24:711–738, 03 2015.

[25] Jiří Komárek, J Kaštovskỳ, J Mareš, and Jeffrey R Johansen. Taxonomic classification of cyanoprokaryotes (cyanobacterial genera) 2014, using a polyphasic approach. *Preslia*, 86(4):295–335, 2014.

[26] Tomáš Hauer and Jiří Komárek. CyanoDB.2.0- On-line database of cyanobacterial genera, 2022.

[27] Brian A Whitton and Malcolm Potts. Introduction to the Cyanobacteria. In Brian A Whitton, editor, *Ecology of Cyanobacteria II: Their Diversity in Space and Time*, pages 1–13. Springer Netherlands, Dordrecht, 2012.

[28] Lucas J Stal. Cyanobacterial mats and stromatolites. In Brian A Whitton, editor, *Ecology of Cyanobacteria II: Their Diversity in Space and Time*, pages 65–125. Springer Netherlands, Dordrecht, 2012.

[29] Rosmarie Rippka, Josette Deruelles, John B Waterbury, Michael Herdman, and Roger Y Stanier. Generic assignments, strain histories and properties of pure cultures of cyanobacteria. *Microbiology*, 111(1):1–61, 1979.

[30] E Hoiczyk. Gliding motility in cyanobacteria: Observations and possible explanations. *Arch. Microbiol.*, 174:11–17, 2000.

[31] Anton Hansgirg. Bemerkungen über die Bewegungen der Oscillarien. *Bot. Ztg*, 41:831, 1883.

[32] Gerhart Drews. Beiträge zur Kenntnis der phototaktischen Reaktionen der Cyanophyceen. *Arch. Protistenk.*, 104:389–430, 1959.

[33] A Hosoi. Secretion of the slime substance in *Oscillatoria* in relation to its movement. *Bot. Mag.(Tokyo)*, 64:14–17, 1951.

[34] AE Walsby. Mucilage secretion and the movements of blue-green algae. *Protoplasma*, 65(1-2):223–238, 1968.

[35] Egbert Hoiczyk and Wolfgang Baumeister. The junctional pore complex, a prokaryotic secretion organelle, is the molecular motor underlying gliding motility in cyanobacteria. *Curr. Biol.*, 8(21):1161–1168, 1998.

[36] Lisa Craig, Michael E Pique, and John A Tainer. Type IV pilus structure and bacterial pathogenicity. *Nat. Rev. Microbiol.*, 2(5):363–378, 2004.

[37] Paula S Duggan, Priscila Gottardello, and David G Adams. Molecular analysis of genes in *Nostoc punctiforme* involved in pilus biogenesis and plant infection. *J. Bacteriol.*, 189(12):4547–4551, 2007.

[38] Douglas D Risser, William G Chew, and John C Meeks. Genetic characterization of the hmp locus, a chemotaxis-like gene cluster that regulates hormogonium development and motility in *Nostoc punctiforme*. *Mol. Microbiol.*, 92(2):222–233, 2014.

[39] Behzad Khayatan, John C Meeks, and Douglas D Risser. Evidence that a modified type IV pilus-like system powers gliding motility and polysaccharide secretion in filamentous cyanobacteria. *Mol. Microbiol.*, 98(6):1021–1036, 2015.

[40] Nils Schuergers, Dennis J Nürnberg, Thomas Wallner, Conrad W Mullineaux, and Annegret Wilde. PilB localization correlates with the direction of twitching motility in the cyanobacterium *Synechocystis* sp. PCC 6803. *Microbiology*, 161(5):960–966, 2015.

[41] Lawrence N Halfen and Richard W Castenholz. Gliding in a blue–green alga: a possible mechanism. *Nature*, 225(5238):1163–1165, 1970.

[42] Lawrence N Halfen and Richard W Castenholz. Gliding motility in the blue-green alga *Oscillatoria princeps*. *J. Phycol.*, 7(2):133–145, 1971.

[43] Joël Tchoufag, Pushpita Ghosh, Connor B Pogue, Beiyan Nan, and Kranthi K Mandadapu. Mechanisms for bacterial gliding motility on soft substrates. *Proc. Natl. Acad. Sci. U.S.A.*, 116(50):25087–25096, 2019.

[44] Nicholas Read, Simon Connell, and David Adams. Nanoscale visualization of a fibrillar array in the cell wall of filamentous cyanobacteria and its implications for gliding motility. *J. Bacteriol.*, 189:7361–6, 11 2007.

[45] RN Shepard and DY Sumner. Undirected motility of filamentous cyanobacteria produces reticulate mats. *Geobiology*, 8(3):179–90, 2010.

[46] Dawn Y Sumner. Late Archean calcite-microbe interactions; two morphologically distinct microbial communities that affected calcite nucleation differently. *Palaios*, 12:302–318, 1997.

[47] Carlos Tamulonis and Jaap Kaandorp. A model of filamentous cyanobacteria leading to reticulate pattern formation. *Life*, 4:433–456, 2014.

[48] John C Meeks. Symbiosis between Nitrogen-Fixing Cyanobacteria and Plants: The establishment of symbiosis causes dramatic morphological and physiological changes in the cyanobacterium. *BioScience*, 48(4):266–276, 04 1998.

[49] Lucas J Stal. *Nitrogen Fixation in Cyanobacteria*, pages 1–9. John Wiley & Sons, Ltd, 2015.

[50] Jonas Kollmen and Dorina Strieth. The Beneficial Effects of Cyanobacterial Co-Culture on Plant Growth. *Life*, 12(2), 2022.

[51] Karl E Havens. Cyanobacteria blooms: effects on aquatic ecosystems. In H. Kenneth Hudnell, editor, *Cyanobacterial Harmful Algal Blooms: State of the Science and Research Needs*, pages 733–747. Springer New York, New York, NY, 2008.

[52] Hélène Barberousse, Ruben J Lombardo, Guillermo Tell, and Alain Couté. Factors involved in the colonisation of building facades by algae and cyanobacteria in France. *Biofouling*, 22(02):69–77, 2006.

[53] Tikam Dakal and Swaranjit Cameotra. Microbially induced deterioration of architectural heritages: Routes and mechanisms involved. *Environmental Sciences Europe*, 24, 12 2012.

[54] Christine C Gaylarde, Peter M Gaylarde, Janine Copp, and Brett Neilan. Polyphasic Detection of Cyanobacteria in Terrestrial Biofilms. *Biofouling*, 20(2):71–79, 2004. PMID: 15203960.

[55] Maria Filomena Macedo, Ana Zélia Miller, Amélia Dionísio, and Cesareo Saiz-Jimenez. Biodiversity of cyanobacteria and green algae on monuments in the Mediterranean Basin: an overview. *Microbiology*, 155(11):3476–3490, 2009.

[56] Dan Wan, Qinghua Wu, and Kamil Kuča. Chapter 42 - Spirulina. In Ramesh C Gupta, editor, *Nutraceuticals*, pages 569–583. Academic Press, Boston, 2016.

[57] Rachana Singh, Parul Parihar, Madhulika Singh, Andrzej Bajguz, Jitendra Kumar, Samiksha Singh, Vijay P Singh, and Sheo M Prasad. Uncovering Potential Applications of

Cyanobacteria and Algal Metabolites in Biology, Agriculture and Medicine: Current Status and Future Prospects. *Frontiers in Microbiology*, 8, 2017.

[58] Nicole Nozzi, John Oliver, and Shota Atsumi. Cyanobacteria as a Platform for Biofuel Production. *Frontiers in Bioengineering and Biotechnology*, 1, 2013.

[59] Parisa Farrokh, Mojgan Sheikhpour, Alibakhsh Kasaeian, Hassan Asadi, and Roya Bavandi. Cyanobacteria as an eco-friendly resource for biofuel production: A critical review. *Biotechnol. Prog.*, 35:e2835, 2019.

[60] Marc J Madou. *Fundamentals of microfabrication: the science of miniaturization*. CRC press, 2018.

[61] QCAD: Open source 2D CAD. `https://www.qcad.org/en/`. Accessed: 24-06-2022).

[62] SU8-3000 Data Sheet. Technical report, Kayaku Advanced Materials.

[63] Oshri Borgman, Thomas Darwent, Enrico Segre, Lucas Goehring, and Ran Holtzman. Immiscible fluid displacement in porous media with spatially correlated particle sizes. *Advances in Water Resources*, 128:158–167, 2019.

[64] Arnaud Hemmerle, Matthias Schröter, and Lucas Goehring. A cohesive granular material with tunable elasticity. *Scientific Reports*, 6(1):35650, 2016.

[65] J Cooper McDonald, David C Duffy, Janelle R Anderson, Daniel T Chiu, Hongkai Wu, Olivier JA Schueller, and George M Whitesides. Fabrication of microfluidic systems in poly(dimethylsiloxane). *ELECTROPHORESIS*, 21(1):27–40, 2000.

[66] H Hillborg, JF Ankner, Ulf W Gedde, GD Smith, HK Yasuda, and K Wikström. Crosslinked polydimethylsiloxane exposed to oxygen plasma studied by neutron reflectometry and other surface specific techniques. *Polymer*, 41(18):6851–6863, 2000.

[67] A Piegari and E Masetti. Thin film thickness measurement: A comparison of various techniques. *Thin Solid Films*, 124(3):249–257, 1985.

[68] Mark E Brezinski. *Optical coherence tomography: principles and applications*. Elsevier,Burlington, 2006.

[69] James G Fujimoto, Costas Pitris, Stephen A Boppart, and Mark E Brezinski. Optical Coherence Tomography: An Emerging Technology for Biomedical Imaging and Optical Biopsy. *Neoplasia*, 2(1):9–25, 2000.

[70] AA Michelson and EW Morley. On the relative motion of the Earth and the luminiferous ether. *American Journal of Science*, s3-34(203):333–345, 1887.

[71] James G Fujimoto, Wolfgang Drexler, Joel S Schuman, and Christoph K Hitzenberger. Optical Coherence Tomography (OCT) in ophthalmology: introduction. *Optics express*, 17(5):3978–3979, 2009.

[72] Wolfgang Drexler, James G Fujimoto, et al. *Optical coherence tomography: technology and applications*, volume 2. Springer, 2015.

[73] Ik-Kyung Jang. *Cardiovascular OCT Imaging*. Springer, 2014.

[74] Haida Liang, Marta Gomez Cid, Radu G Cucu, GM Dobre, A Gh Podoleanu, Justin Pedro, and David Saunders. En-face optical coherence tomography-a novel application of non-invasive imaging to art conservation. *Optics Express*, 13(16):6133–6144, 2005.

[75] Haida Liang, Rada Cucu, George M Dobre, David A Jackson, Justin Pedro, Christopher Pannell, David Saunders, and Adrian GH Podoleanu. Application of OCT to examination of easel paintings. In *Second European Workshop on Optical Fibre Sensors*, volume 5502, pages 378–381. SPIE, 2004.

[76] Haida Liang, Borislava Peric, Michael Hughes, Adrian Podoleanu, Marika Spring, and David Saunders. Optical coherence tomography for art conservation and archaeology. In *O3A: Optics for Arts, Architecture, and Archaeology*, volume 6618, pages 32–43. SPIE, 2007.

[77] Chi Cheung and Haida Liang. Ultra-high resolution Fourier domain optical coherence tomography for resolving thin layers in painted works of art. *Proc SPIE*, 8790, 05 2013.

[78] HA.Haus and EP Ippen. Group velocity of solitons. *Opt. Lett.*, 26(21):1654–1656, Nov 2001.

[79] Mikhail N Polyanskiy. Refractive index database.

[80] Benedikt W Graf, Steven G Adie, and Stephen A Boppart. Correction of coherence gate curvature in high numerical aperture optical coherence imaging. *Opt. Lett.*, 35(18):3120–3122, Sep 2010.

[81] James Pawley. *Handbook of biological confocal microscopy*, volume 236. Springer Science & Business Media, 2006.

[82] Monica Monici. Cell and tissue autofluorescence research and diagnostic applications. volume 11 of *Biotechnology Annual Review*, pages 227–256. Elsevier, 2005.

[83] David Millie, Oscar Schofield, Gary Kirkpatrick, Geir Johnsen, and Terence Evens. Using absorbance and fluorescence spectra to discriminate microalgae. *Eur. J. Phycol.*, 37(3):313–322, 2002.

[84] Ellen C Jensen. Use of fluorescent probes: their effect on cell biology and limitations. *The Anatomical Record: Advances in Integrative Anatomy and Evolutionary Biology*, 295(12):2031–2036, 2012.

[85] J Schindelin, I Arganda-Carreras, E Frise, V Kaynig, M Longair, T Pietzsch, and A Cardona. Fiji: an open-source platform for biological-image analysis. *Nat. Methods*, 9(7):676–682, 2012.

[86] Thomas Friedl and Maike Lorenz. The Culture Collection of Algae at Göttingen University (SAG): A Biological Resource for Biotechnological and Biodiversity Research. *Procedia Environmental Sciences*, 15:110–117, 2012. Innovative Researches on Algal Biomass.

[87] David Boal and Ray Ng. Shape analysis of filamentous Precambrian microfossils and modern cyanobacteria. *Paleobiology*, 36(4):555–572, 2010.

[88] Otakar Strunecky, Jiri Komárek, and Jan Šmarda. Kamptonema (Microcoleaceae, Cyanobacteria), a new genus derived from the polyphyletic Phormidium on the basis of combined molecular and cytomorphological markers. *Preslia*, 86:193–207, 05 2014.

[89] Maike Lorenz, Thomas Friedl, and John Day. Perpetual Maintenance of Actively Metabolizing Microalgal Cultures. In Robert A. Andersen, editor, *Algal Culturing Techniques*, pages 145–156. Elsevier Academic Press, New York., 01 2005.

[90] Ian Stewart, Wayne W Carmichael, Ross Sadler, Glenn B McGregor, Karen Reardon, Geoffrey K Eaglesham, Wasantha A Wickramasinghe, Alan A Seawright, and Glen R Shaw. Occupational and environmental hazard assessments for the isolation, purification and toxicity testing of cyanobacterial toxins. *Environmental Health*, 8(1):1–12, 2009.

[91] Mixon K Faluweki and Lucas Goehring. Structural mechanics of filamentous cyanobacteria. *Journal of The Royal Society Interface*, 19(192):20220268, 2022.

[92] MC Marchetti, JF Joanny, S Ramaswamy, TB Liverpool, J Prost, Madan Rao, and R Aditi Simha. Hydrodynamics of soft active matter. *Rev. Mod. Phys.*, 85:1143, 2013.

[93] Amin Doostmohammadi, Jordi Ignés-Mullol, Julia M Yeomans, and Francesc Sagués. Active nematics. *Nat. Commun.*, 9(1):1–13, 2018.

[94] Roland G Winkler and Gerhard Gompper. The physics of active polymers and filaments. *J. Chem. Phys.*, 153:040901, 2020.

[95] Zahra Mokhtari and Annette Zippelius. Dynamics of active filaments in porous media. *Phy. Rev. Lett.*, 123:028001, 2019.

[96] Thi Hiep Han, Sandesh Y Sawant, Sun-Jin Hwang, and Moo Hwan Cho. Three-dimensional, highly porous N-doped carbon foam as microorganism propitious, efficient anode for high performance microbial fuel cell. *RSC Adv.*, 6(31):25799–25807, 2016.

[97] Ya-Qiong Wang, Han-Xiong Huang, Bin Li, and Wei-Shan Li. Novelly developed three-dimensional carbon scaffold anodes from polyacrylonitrile for microbial fuel cells. *J. Mater. Chem. A*, 3(9):5110–5118, 2015.

[98] T Shaw, M Winston, CJ Rupp, I Klapper, and P. Stoodley. Commonality of elastic relaxation times in biofilms. *Phys. Rev. Lett.*, 93:098102, 2004.

[99] LD Landau and EM Lifshitz. *Theory of Elasticity: Vol. 7 of Course of Theoretical Physics.* Elsevier, Oxford, UK, 1986.

[100] I Eames and Christian Klettner. Stokes' and Lamb's viscous drag laws. *Eur. J. Phys.*, 38:025003, 03 2017.

[101] Horace Lamb. XV. On the uniform motion of a sphere through a viscous fluid . *Lond. Edinb. Dublin philos. mag. j. sci.*, 21(121):112–121, 1 1911.

[102] GK Batchelor. *An Introduction to Fluid Dynamics.* Cambridge University Press, 1967.

[103] GK Batchelor. Slender-body theory for particles of arbitrary cross-section in Stokes flow. *J. Fluid Mech.*, 44:419–440, 1970.

[104] Eric Lauga and Thomas R Powers. The hydrodynamics of swimming microorganisms. *Rep. Prog. Phys.*, 72:096601, 2009.

[105] Ariel Amir, Farinaz Babaeipour, Dustin B. McIntosh, David R. Nelson, and Suckjoon Jun. Bending forces plastically deform growing bacterial cell walls. *Proc. Natl. Acad. Sci. U.S.A.*, 111(16):5778–5783, 2014.

[106] David Boal. *Mechanics of the Cell.* Cambridge University Press, 2nd edition, 2012.

[107] G Binnig, CF Quate, and Ch Gerber. Atomic Force Microscope. *Phys. Rev. Lett.*, 56:930–933, Mar 1986.

[108] G Binnig, Ch Gerber, E Stoll, TR Albrecht, and CF Quate. Atomic Resolution with Atomic Force Microscope. *Europhysics Letters (EPL)*, 3(12):1281–1286, jun 1987.

[109] Yves F Dufrêne, Toshio Ando, Ricardo Garcia, David Alsteens, David Martinez-Martin, Andreas Engel, Christoph Gerber, and Daniel J Müller. Imaging modes of atomic force microscopy for application in molecular and cell biology. *Nature nanotechnology*, 12(4):295–307, 2017.

[110] Alvaro San Paulo and Ricardo Garcia. Unifying theory of tapping-mode atomic-force microscopy. *Physical Review B*, 66(4):041406, 2002.

[111] Brunero Cappella and Giovanni Dietler. Force-distance curves by atomic force microscopy. *Surface science reports*, 34(1-3):1–104, 1999.

[112] Shaoyang Liu and Yifen Wang. Application of AFM in microbiology: a review. *Scanning*, 32(2):61–73, 2010.

[113] Bede Pittenger, Natalia Erina, and Chanmin su. Quantitative mechanical mapping at nanoscale with peak force QNM. *Bruker Application Note #128.*, 2009.

[114] Bede Pittenger, Natalia Erina, and Chanmin Su. *Mechanical Property Mapping at the Nanoscale Using PeakForce QNM Scanning Probe Technique*, pages 31–51. Springer Netherlands, Dordrecht, 2014.

[115] Heinrich Hertz. Ueber die Berührung fester elastischer Körper. *J. reine u. Angew. Math*, 92:156–171, 1881.

[116] Kenneth Langstreth Johnson, Kevin Kendall, and AD Roberts. Surface energy and the contact of elastic solids. *Proc. Roy. Soc. London A*, 324(1558):301–313, 1971.

[117] BV Derjaguin, VM Muller, and YP Toporov. Effect of contact deformations on the adhesion of particles. *J. Colloid Interface Sci.*, 53(2):314–326, 1975.

[118] Marco P E Wenger, Laurent Bozec, Michael A Horton, and Patrick Mesquidaz. Mechanical Properties of Collagen Fibrils. *Biophys. J.*, 93:1255–1263, 2007.

[119] J Hrouz, V Vojta, and M Ilavský. Penetration behavior of the system sphere-cylinder. *Polym. Eng. Sci.*, 20(6):402–405, 2010.

[120] Stylianos-Vasileios Kontomaris, Andreas Stylianou, Anna Malamou, and Triantafyllos Stylianopoulos. A discussion regarding the approximation of cylindrical and spherical shaped samples as half spaces in AFM nanoindentation experiments. *Mater. Res. Express*, 5(8):085402, 2018.

[121] Amir Sanati Nezhad, Mahsa Naghavi, Muthukumaran Packirisamy, Rama Bhat, and Anja Geitmann. Quantification of the Young's modulus of the primary plant cell wall using Bending-Lab-On-Chip (BLOC). *Lab Chip*, 13:2599–2608, 2013.

[122] Yaron Caspi. Deformation of filamentous *Escherichia coli* cells in a microfluidic device: A new technique to study cell mechanics. *PLoS One*, 9(1):1–10, 01 2014.

[123] Carl D Meinhart, Steve T Wereley, and Juan G Santiago. PIV measurements of a microchannel flow. *Experiments in fluids*, 27(5):414–419, 1999.

[124] Joseph Boussinesq. Mémoire sur l'influence des frottements dans les mouvements réguliers des fluids. *J. Math. Pures Appl.*, 13(2):377–424, 1868.

[125] Frank White. *Viscous Fluid Flow 3rd Edition*. McGraw-Hill, Boston, 3rd edition, 2006.

[126] William Thielicke and René Sonntag. Particle Image Velocimetry for MATLAB: Accuracy and enhanced algorithms in PIVlab. *Journal of Open Research Software*, 9, 2021.

[127] Rob Campbell (2022). raacampbell/shadedErrorBar, MATLAB Central File Exchange. Retrieved January 31, 2022.

[128] Eric Lauga, Michael Brenner, and Howard Stone. Microfluidics: The No-Slip Boundary Condition. In Cameron Tropea, Alexander L Yarin, and John F Foss, editors, *Springer Handbook of Experimental Fluid Mechanics*, pages 1219–1240. Springer, Berlin, Heidelberg, 2007.

[129] Horace Lamb. *Hydrodynamics*. Dover, New York, 2014.

[130] Derek C Tretheway and Carl D Meinhart. Apparent fluid slip at hydrophobic microchannel walls. *Physics of Fluids*, 14(3):L9–L12, 2002.

[131] TJ Young, MA Monclus, TL Burnett, WR Broughton, SL Ogin, and PA Smith. The use of the PeakForce^{TM} quantitative nanomechanical mapping AFM-based method for high-resolution Young's modulus measurement of polymers. *Meas. Sci. Technol.*, 22(12):125703, 10 2011.

[132] Chris J Wright and Ian Armstrong. The application of atomic force microscopy force measurements to the characterisation of microbial surfaces. *Surf. Interface Anal.*, 38:1419–1428, 2006.

[133] X Yao, Manfred Jericho, Deann Pink, and T Beveridge. Thickness and elasticity of Gram-negative murein sacculi measured by atomic force microscopy. *J. Bacteriol.*, 181:6865–75, 12 1999.

[134] Giovanni Longo, Laura Rio, Roduit Charles, Andrej Trampuz, Alain Bizzini, Giovanni Dietler, and Sandor Kasas. Force volume and stiffness tomography investigation on the dynamics of stiff material under bacterial membranes. *J. Mol. Recognit.*, 25:278–84, 05 2012.

[135] Yi Deng, Mingzhai Sun, and Joshua Shaevitz. Direct measurement of cell wall stress stiffening and turgor pressure in live bacterial cells. *Phys. Rev. Lett.*, 107:158101, 10 2011.

[136] JJ Thwaites and NH Mendelson. Mechanical properties of peptidoglycan as determined from bacterial thread. *Int. J. Biol. Macromol.*, 11(4):201—206, 1989.

[137] NH Mendelson and JJ Thwaites. Cell wall mechanical properties as measured with bacterial thread made from *Bacillus subtilis. J. Bacteriol.*, 171(2):1055–1062, 1989.

[138] George K Auer and Douglas B Weibel. Bacterial cell mechanics. *Biochemistry*, 56:3710–3724, 2017.

[139] Nikolai Chernov (2021). Circle Fit (Pratt method), MATLAB Central File Exchange. Retrieved August 12, 2021.

[140] Vaughan Pratt. Direct least-squares fitting of algebraic surfaces. *SIGGRAPH Comput. Graph.*, 21(4):145–152, 08 1987.

[141] Cornelis Storm, Jennifer J Pastore, FC MacKintosh, TC Lubensky, and Paul A Janmey. Nonlinear elasticity in biological gels. *Nature*, 435:191–194, 2005.

[142] Maximilian Kurjahn, Antaran Deka, Antoine Girot, Leila Abbaspour, Stefan Klumpp, Maike Lorenz, Oliver Bäumchen, and Stefan Karpitschka. Self-buckling of filamentous cyanobacteria reveals gliding forces. *arXiv:2202.13658 [physics.bio-ph]*, 2022.

[143] Egbert Hoiczyk and Wolfgang Baumeister. Envelope structure of four gliding filamentous cyanobacteria. *J. Bacteriol.*, 177(9):2387–2395, 1995.

[144] Egbert Hoiczyk and Alfred Hansel. Cyanobacterial cell walls: news from an unusual prokaryotic envelope. *J. Bacteriol.*, 182(5):1191–1199, 2000.

[145] Ahmed Touhami, Bernard Nysten, and Yves F Dufrêne. Nanoscale mapping of the elasticity of microbial cells by atomic force microscopy. *Langmuir*, 19:4539–4543, 2003.

[146] JJ Thwaites and UC Surana. Mechanical properties of *Bacillus subtilis* cell walls: Effects of removing residual culture medium. *J. Bacteriol.*, 173:197–203, 1991.

[147] Robert P Burchard. Gliding motility of prokaryotes: ultrastructure, physiology, and genetics. *Ann. Rev. Microbiol.*, 35:497–529, 1981.

[148] Richard P Feynman, Robert B Leighton, and Matthew Sands. *The Feynman Lectures on Physics (Vol. 2)*. Pearson, 2009.

[149] M Doi and SF Edwards. *Theory of Polymer Dynamics*. Oxford University Press, USA, 1986.

[150] Frederick Gittes, Brian Mickey, Jilda Nettleton, and Jonathon Howard. Flexural rigidity of microtubules and actin filaments measured from thermal fluctuations in shape. *J. Cell Biol.*, 120:923–934, 1993.

[151] Annegret Wilde and Conrad W Mullineaux. Motility in cyanobacteria: polysaccharide tracks and Type IV pilus motors. *Molecular Microbiology*, 98(6):998–1001, 2015.

[152] Jamie-Lee Berry and Vladimir Pelicic. Exceptionally widespread nanomachines composed of type IV pilins: the prokaryotic Swiss Army knives. *FEMS microbiology reviews*, 39(1):134–154, 2015.

[153] Mecky Pohlschroder, Abhrajyoti Ghosh, Manuela Tripepi, and Sonja-Verena Albers. Archaeal type IV pilus-like structures—evolutionarily conserved prokaryotic surface organelles. *Current opinion in microbiology*, 14(3):357–363, 2011.

[154] Stephen Melville and Lisa Craig. Type IV pili in Gram-positive bacteria. *Microbiology and molecular biology reviews*, 77(3):323–341, 2013.

[155] Manuela Hospenthal, Tiago Costa, and Gabriel Waksman. A comprehensive guide to pilus biogenesis in Gram-negative bacteria. *Nat Rev Micro*, 15:365–379, 06 2017.

[156] Juan Xicohtencatl-Cortes, Valério Monteiro-Neto, Zeus Saldana, Maria A Ledesma, Jose Luís Puente, and Jorge A Girón. The type 4 pili of enterohemorrhagic Escherichia coli O157: H7 are multipurpose structures with pathogenic attributes. *Journal of bacteriology*, 191(1):411–421, 2009.

[157] David Bieber, Sandra W Ramer, Cheng-Yen Wu, William J Murray, Toru Tobe, Rosemary Fernandez, and Gary K Schoolnik. Type IV pili, transient bacterial aggregates, and virulence of enteropathogenic Escherichia coli. *Science*, 280(5372):2114–2118, 1998.

[158] Beronda L Montgomery. Sensing the light: photoreceptive systems and signal transduction in cyanobacteria. *Molecular microbiology*, 64(1):16–27, 2007.

[159] Mixon K. Faluweki, Jan Cammann, Marco G. Mazza, and Lucas Goehring. Active spaghetti: Collective organization in cyanobacteria, 2023.

[160] Charles I Hubert. *Electric machines*. Prentice Hall, 1990.

[161] David G Adams, Denise Ashworth, and Brenda Nelmes. Fibrillar array in the cell wall of a gliding filamentous cyanobacterium. *Journal of bacteriology*, 181(3):884–892, 1999.

[162] TN Glagoleva, AN Glagolev, MV Gusev, and KA Nikitina. Protonmotive force supports gliding in cyanobacteria. *FEBS Lett.*, 117(1-2):49–53, 1980.

[163] Abraham Savitzky and MJE Golay. Smoothing and Differentiation of Data by Simplified Least Squares Procedures. *Anal. Chem.*, 36(8):1627–1639, 1964.

[164] Ronald W Schafer. What Is a Savitzky-Golay Filter? [Lecture Notes]. *IEEE Signal Process Mag*, 28(4):111–117, 2011.

[165] Yutaka Sumino, Ken H Nagai, Yuji Shitaka, Dan Tanaka, Kenichi Yoshikawa, Hugues Chaté, and Kazuhiro Oiwa. Large-scale vortex lattice emerging from collectively moving microtubules. *Nature*, 483(7390):448–452, 2012.

[166] George EP Box, Gwilym M Jenkins, Gregory C Reinsel, and Greta M Ljung. *Time series analysis: forecasting and control*. John Wiley & Sons, 2015.

[167] Takuma Sugi, Hiroshi Ito, Masaki Nishimura1, and Ken H Nagai. C. elegans collectively forms dynamical networks. *Nat. Commun.*, 10:683, 2019.

[168] Richard W Castenholz. Cyanobacteria. *Bergey's Manual of Systematics of Archaea and Bacteria*, pages 1–2, 2015.

[169] Wilhelm Nultsch and Donat-P Häder. Photomovement in motile microorganisms—II. *Photochemistry and Photobiology*, 47(6):837–869, 1988.

[170] Francesco Lenci. *CRC Handbook of Organic Photochemistry and Photobiology*. CRC Press, 2004.

[171] Malin Nilsson, Ulla Rasmussen, and Birgitta Bergman. Cyanobacterial chemotaxis to extracts of host and nonhost plants. *FEMS Microbiology Ecology*, 55(3):382–390, 03 2006.

[172] VL Gabai. A one-instant mechanism of phototaxis in the cyanobacterium Phormidium uncinatum. *FEMS microbiology letters*, 30(1-2):125–129, 1985.

[173] Ken H Nagai, Yutaka Sumino, Raul Montagne, Igor S Aranson, and Hugues Chaté. Collective motion of self-propelled particles with memory. *Physical review letters*, 114(16):168001, 2015.

[174] Hiroki Yamamoto, Yuki Fukasawa, Yu Shoji, Shumpei Hisamoto, Tomohiro Kikuchi, Atsuko Takamatsu, and Hideo Iwasaki. Scattered migrating colony formation in the filamentous cyanobacterium, *Pseudanabaena* sp. NIES-4403. *BMC Microbiol.*, 21:227, 2021.

[175] Leila Abbaspour, Ali Malek, Stefan Karpitschka, and Stefan Klumpp. Effects of direction reversals on patterns of active filaments. *arXiv:2112.09188 [cond-mat.soft]*, 2021.

[176] MJ Romeu, D Domínguez-Pérez, D Almeida, J Morais, MJ Araújo, H Osório, A Campos, V Vasconcelos, and FJ Mergulhão. Quantitative proteomic analysis of marine biofilms formed by filamentous cyanobacterium. *Environmental Research*, 201:111566, 2021.

[177] Maria J Romeu, Patrícia Alves, João Morais, João M Miranda, Ed D de Jong, Jelmer Sjollema, Vítor Ramos, Vitor Vasconcelos, and Filipe JM Mergulhão. Biofilm formation behaviour of marine filamentous cyanobacterial strains in controlled hydrodynamic conditions. *Environmental microbiology*, 21(11):4411–4424, 2019.

[178] John T Emlen. Flocking behavior in birds. *The Auk*, 69(2):160–170, 1952.

[179] Michele Ballerini, Nicola Cabibbo, Raphael Candelier, Andrea Cavagna, Evaristo Cisbani, Irene Giardina, Vivien Lecomte, Alberto Orlandi, Giorgio Parisi, Andrea Procaccini, et al. Interaction ruling animal collective behavior depends on topological rather than metric distance: Evidence from a field study. *Proceedings of the national academy of sciences*, 105(4):1232–1237, 2008.

[180] Tony J Pitcher. *The behaviour of teleost fishes*. Springer Science & Business Media, 2012.

[181] Shay Gueron, Simon A Levin, and Daniel I Rubenstein. The dynamics of herds: from individuals to aggregations. *Journal of Theoretical Biology*, 182(1):85–98, 1996.

[182] Hanspeter Kunz and Charlotte K Hemelrijk. Artificial fish schools: collective effects of school size, body size, and body form. *Artificial life*, 9(3):237–253, 2003.

[183] Guillaume Grégoire, Hugues Chaté, and Yuhai Tu. Moving and staying together without a leader. *Physica D: Nonlinear Phenomena*, 181(3-4):157–170, 2003.

[184] Vasily Kantsler, Jörn Dunkel, Marco Polin, and Raymond E Goldstein. Ciliary contact interactions dominate surface scattering of swimming eukaryotes. *Proceedings of the National Academy of Sciences*, 110(4):1187–1192, 2013.

[185] Tomáš Hauer, Radka Mühlsteinová, Markéta Bohunická, Jan Kaštovskỳ, and Jan Mareš. Diversity of cyanobacteria on rock surfaces. *Biodiversity and conservation*, 24(4):759–779, 2015.

[186] P Albertano, D Moscone, G Palleschi, B Hermosin, C Saiz-Jimenez, S Sanchez-Moral, M Hernández-Mariné, C Urzì, I Groth, V Schroeckh, et al. Cyanobacteria attack rocks (CATS): control and preventive strategies to avoid damage caused by cyanobacteria and associated microorganisms in Roman hypogean monuments. *Molecular biology and cultural heritage*, pages 151–162, 2003.

[187] Bettina E Schirrmeister, Jurriaan M de Vos, Alexandre Antonelli, and Homayoun C Bagheri. Evolution of multicellularity coincided with increased diversification of cyanobacteria and the Great Oxidation Event. *Proceedings of the National Academy of Sciences*, 110(5):1791–1796, 2013.

[188] Andrew H Knoll. Cyanobacteria and earth history. *The cyanobacteria: molecular biology, genomics, and evolution*, 484, 2008.

[189] Nils E Persson, Michael A McBride, Martha A Grover, and Elsa Reichmanis. Automated Analysis of Orientational Order in Images of Fibrillar Materials. *Chemistry of Materials*, 29(1):3–14, 2017.

[190] Zhe Qiang, Longhe Zhang, Gila E Stein, Kevin A Cavicchi, and Bryan D Vogt. Unidirectional Alignment of Block Copolymer Films Induced by Expansion of a Permeable Elastomer during Solvent Vapor Annealing. *Macromolecules*, 47(3):1109–1116, 2014.

[191] Jeffrey N Murphy, Kenneth D Harris, and Jillian M Buriak. Automated Defect and Correlation Length Analysis of Block Copolymer Thin Film Nanopatterns. *PLOS ONE*, 10(7):1–32, 07 2015.

[192] Sophia Jordens, Lucio Isa, Ivan Usov, and Raffaele Mezzenga. Non-equilibrium nature of two-dimensional isotropic and nematic coexistence in amyloid fibrils at liquid interfaces. *Nature communications*, 4:1917, 05 2013.

[193] Ivan Usov and Raffaele Mezzenga. FiberApp: An Open-Source Software for Tracking and Analyzing Polymers, Filaments, Biomacromolecules, and Fibrous Objects. *Macromolecules*, 48:150210103859007, 02 2015.

[194] Daiki Nishiguchi, Ken H Nagai, Hugues Chaté, and Masaki Sano. Long-range nematic order and anomalous fluctuations in suspensions of swimming filamentous bacteria. *Physical Review E*, 95(2):020601, 2017.

[195] Gareth P Alexander, Bryan Gin-ge Chen, Elisabetta A Matsumoto, and Randall D Kamien. Colloquium: Disclination loops, point defects, and all that in nematic liquid crystals. *Reviews of Modern Physics*, 84(2):497, 2012.

[196] Xingzhou Tang and Jonathan V. Selinger. Orientation of topological defects in 2D nematic liquid crystals. *Soft Matter*, 13:5481–5490, 2017.

[197] Thuan Beng Saw, Amin Doostmohammadi, Vincent Nier, Leyla Kocgozlu, Sumesh Thampi, Yusuke Toyama, Philippe Marcq, Chwee Teck Lim, Julia M Yeomans, and Benoit Ladoux. Topological defects in epithelia govern cell death and extrusion. *Nature*, 544(7649):212–216, 2017.

[198] Oliver J Meacock, Amin Doostmohammadi, Kevin R Foster, Julia M Yeomans, and William M Durham. Bacteria solve the problem of crowding by moving slowly. *Nature Physics*, 17(2):205–210, 2021.

[199] Nicole Tandeau de Marsac and Jean Houmard. Adaptation of cyanobacteria to environmental stimuli: new steps towards molecular mechanisms. *FEMS Microbiology Letters*, 104(1):119–189, 1993.

[200] Victoria Meslier and Jocelyne DiRuggiero. Endolithic microbial communities as model systems for ecology and astrobiology. *Model Ecosystems in Extreme Environments*, 2019.

[201] Emine Ertekin, Victoria Meslier, Alyssa Browning, John Treadgold, and Jocelyne DiRuggiero. Rock structure drives the taxonomic and functional diversity of endolithic microbial communities in extreme environments. *Environmental Microbiology*, 23(7):3937–3956, 2021.

[202] Stephen Archer, Asunción De los Ríos, Kevin Lee, Thomas Niederberger, Stephen Cary, Kathryn Coyne, Susanne Douglas, Donnabella Lacap-Bugler, and Stephen Pointing. Endolithic microbial diversity in sandstone and granite from the McMurdo Dry Valleys, Antarctica. *Polar Biology*, 40:1–10, 05 2017.

[203] Nicole Nozzi, John Oliver, and Shota Atsumi. Cyanobacteria as a Platform for Biofuel Production. *Frontiers in Bioengineering and Biotechnology*, 1, 2013.

[204] T Iwaki, K Haranoh, N Inoue, K Kojima, R Satoh, T Nishino, S Wada, Hideshi Ihara, S Tsuyama, H Kobayashi, and A Wadano. Expression of foreign type I ribulose-1,5-bisphosphate carboxylase/ oxygenase (EC 4.1.1.39) stimulates photosynthesis in cyanobacterium Synechococcus PCC7942 cells. *Photosynthesis research*, 88:287–97, 07 2006.

[205] Hu Qiang, Yair Zarmi, and Amos Richmond. Combined effects of light intensity, light-path and culture density on output rate of Spirulina platensis (Cyanobacteria). *European Journal of Phycology*, 33(2):165–171, 1998.

[206] Warren C Young, Richard G Budynas, and Ali M Sadegh. *Roark's formulas for stress and strain*. McGraw-Hill Education, 2012.

[207] Guillaume Duclos, Christoph Erlenkämper, Jean-François Joanny, and Pascal Silberzan. Topological defects in confined populations of spindle-shaped cells. *Nature Physics*, 13(1):58–62, 2017.

[208] Miriam Rosenbaum, Zhen He, and Largus T Angenent. Light energy to bioelectricity: photosynthetic microbial fuel cells. *Current opinion in biotechnology*, 21(3):259–264, 2010.

[209] Hanyu Wang, Fang Qian, and Yat Li. Solar-assisted microbial fuel cells for bioelectricity and chemical fuel generation. *Nano Energy*, 8:264–273, 2014.

[210] Alistair J McCormick, Paolo Bombelli, Robert W Bradley, Rebecca Thorne, Tobias Wenzel, and Christopher J Howe. Biophotovoltaics: oxygenic photosynthetic organisms in the world of bioelectrochemical systems. *Energy & Environmental Science*, 8(4):1092–1109, 2015.

[211] Marin Sawa, Andrea Fantuzzi, Paolo Bombelli, Christopher J Howe, Klaus Hellgardt, and Peter J Nixon. Electricity generation from digitally printed cyanobacteria. *Nature communications*, 8(1):1–10, 2017.

[212] Luca Giomi, Mark J Bowick, Prashant Mishra, Rastko Sknepnek, and M Cristina Marchetti. Defect dynamics in active nematics. *Philosophical Transactions of the Royal Society A: Mathematical, Physical and Engineering Sciences*, 372(2029):20130365, 2014.

[213] Kirsten Harth and Ralf Stannarius. Topological point defects of liquid crystals in quasi-two-dimensional geometries. *Frontiers in Physics*, 8:112, 2020.

[214] Tim Sanchez, Daniel TN Chen, Stephen J DeCamp, Michael Heymann, and Zvonimir Dogic. Spontaneous motion in hierarchically assembled active matter. *Nature*, 491(7424):431–434, 2012.